UNIVERSITAT DE BARCELONA

Numerical Relativity studies in Anti-de Sitter spacetimes: Gravitational Collapse and the AdS/CFT correspondence

Daniel Santos-Oliván

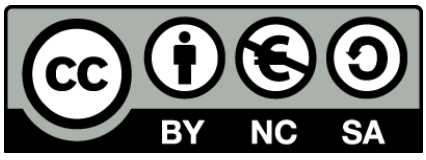

INSTITUT DE CIÈNCIES DE L'ESPAI
(CSIC-IEEC)

UNIVERSITAT DE BARCELONA

Numerical Relativity studies in Anti-de Sitter spacetimes: Gravitational Collapse and the AdS/CFT correspondence

DOCTORAL THESIS

Author:
Daniel SANTOS-OLIVÁN

Supervisor:
Dr. Carlos F. SOPUERTA

Numerical Relativity studies in Anti-de Sitter spacetimes: Gravitational Collapse and the AdS/CFT correspondence

A dissertation by:

Daniel Santos-Oliván

for the degree of Doctor of Philosophy in Physics

INSTITUT DE CIÈNCIES DE L'ESPAI (CSIC-IEEC)

Gravitational Wave Astronomy - LISA Group

Supervisor: Carlos F. Sopuerta

UNIVERSITAT DE BARCELONA

Facultat de Física

Departament de Física Quàntica i Astrofísica

Tutor: Dr. Domènec Espriu

"Unthinking respect for authority is the greatest enemy of truth.."

Albert Einstein

Abstract

In this thesis we study three different problems using Numerical Relativity on asymptotically Anti-de Sitter (AdS) spacetimes. The first is our research on the gravitational collapse of massless scalar fields on asymptotically AdS spacetimes. We have developed a new method that combines two different formulations of the Einstein Field Equations to get closer and with more accuracy to the collapse. We have numerical evidence that in the separation of the branches there is a universal power law in the mass of the formed apparent horizons for subcritical configurations in addition to the one for supercritical ones. This new power law confirms that there is a gap in the mass of the apparent horizon. In the second part, we introduce a shock waves model in AdS to study the far-from-equilibrium regime in the heavy ion collisions through the holographic correspondence in a non-conformal theory. In the models used until now, the shock waves correspond to conformal gauge theories while QCD is not conformal. In order to get closer to a description of the actual physical collisions we present the first shock waves collision in a non-conformal theory. With this, we show how the non-conformality increases the hydrodynamisation time and also that this can happen before the equation of state is fulfilled. In the last part, we propose the use of spectral methods for high precision computations. The exponential convergence of spectral methods can approximate functions with very high accuracy with few hundred terms in our spectral expansion while in other numerical methods it would be a few orders of magnitude larger. This makes spectral methods very attractive because they facilitate the accessibility to very small error simulations, removes the bottleneck of the memory demand and also help in the computational speed because fewer points are needed for the computation. We have tested this idea with the **ANETO** library for simulations in AdS spacetimes and the gravitational collapse in an asymptotically flat spacetime with very promising results. This library has been developed as a direct result of this thesis and that can be downloaded as Free Software.

Agradecimientos

En primer lugar quiero agradecer a mi director, Carlos, la oportunidad de venir a Barcelona y de introducirme en el campo de la Relatividad Numérica. También agradecer su apoyo y guía durante los últimos cinco años en la realización del máster y de esta tesis doctoral. Ha sido un viaje apasionante y provechoso que difícilmente hubiera iniciado de no haber venido aquí.

También quiero agradecer al Institut de Ciències de l'Espai y al Insitut d'Estudis Espacials de Catalunya por su apoyo en los últimos años. En especial al grupo de Ondas Gravitacionales que me ha permitido conocer de primera mano el desarrollo de una misión espacial tan compleja como LISA Pathfinder. A Carlos, Miquel, Ivan, Nacho, Ferran, Nikos, Francisco, Juan Pedro, Marius, Lluís y Víctor. En especial a estos dos últimos que siempre han tenido la paciencia necesaria para ayudarme y enseñarme tantas cosas sobre programación. Molta sort amb LISA els propers anys! No puedo olvidarme del resto de compañeros del ICE como el resto de doctorandos y en especial de mis compañeros de despacho en estos últimos dos años Ferran, Ramon, Fran y Juan Pedro; muchas gracias por tantas jornadas *productivas*.

Agradecer también a mis colaboradores de la Universitat de Barcelona, David, Jorge, Miguel, Miquel y Max, por haberme introducido en el campo de la holografía y del quark-gluon plasma. También al resto de personas que he conocido en dicha universidad a lo largo de los años. Al profesor Ulrich Sperhake quiero agradecerle la oportunidad de poder disfrutar de una estancia en el Departamento de Matemática Aplicada y Física Teórica de la Universidad de Cambridge.

No quiero olvidar a mis antiguos compañeros de la Universidad de Zaragoza con los que comencé mi sinuoso camino por el mundo de la física y que después de tantos años hemos acabado esparcidos no sólo en el mapa sino en los campos de la ciencia. Fue una gran experiencia que me aportó mucho.

No puedo dejarme a mi familia. En especial a mis padres, que con su apoyo incondicional y su ejemplo me han ayudado a estar aquí. También a Antonio y Sara, que han estado ahí siempre que los he necesitado.

Y, por supuesto, a Alba, que me ha acompañado todos estos años y ha sufrido y disfrutado todo lo que ellos han traído. Muchísimas gracias por tu paciencia y por tu amor.

Esta tesis doctoral ha sido finanziada por el Ministerio de Economía y Competitivdad con la ayuda para la Formación de Personal Investigador (BES-2012-057909) del proyecto AYA2010-15709.

x

Contents

List of Figures

List of Tables

List of Abbreviations

AAdS	**A**symptotically **A**nti-**d**e **S**itter
AdS	**A**nti-**d**e **S**itter
AMR	**A**daptive **M**esh **R**efinement
AH	**A**pparent **H**orizon
BH	**B**lack **H**ole
BBH	**B**inary **B**lack **H**ole
CFL	**C**ourant-**F**riedrichs **L**ewy (condition)
CFT	**C**onformal **F**ield **T**heory
DCT	**D**iscrete **C**osine **T**ransform
DSS	**D**iscrete **S**elf **S**imilar
EF	**E**ddington **F**inkelstein
EFEs	**E**instein's **F**ield **E**quation**s**
EH	**E**vent **H**orizon
GR	**G**eneral **R**elativity
FFT	**F**ast **F**ourier **T**ransform
FG	**F**efferman **G**raham
MPFR	(GNU) **M**ultiple **P**recision **F**loating-point **R**eliably
ODE	**O**rdinary **D**ifferential **E**quation
PDE	**P**artial **D**ifferential **E**quation
PSC	**P**seudo-**S**pectral **C**ollocation (methods)
QCD	**Q**uantum-**C**hromo **D**ynamics
QGP	**Q**uark-**G**luon **P**lasma
RK	**R**unge-**K**utta (methods)

List of Symbols

c	the speed of light, unless otherwise specified equal to one
d	number of dimensions of the space.
$d+1$	number of dimensions of the spacetime.
$g_{\mu\nu}$	metric of the spacetime
$i, j, ...$	latin letters: space indices
ℓ	AdS lenght scale
G	Newton's constant, unless otherwise specified equal to one
R	Scalar of curvature
$R_{\mu\nu}$	Ricci curvature tensor
$T_{\mu\nu}$	Stress-energy tensor
γ	Choptuik's critical exponent
Δ	Choptuik's echoing period
Λ	Cosmological constant
$\mu, \nu, ...$	greek letters: spacetime indices
ξ	mass gap exponent in AdS
ϕ	Scalar field
∂_μ	partial derivative respect to coordinate μ.
∇_μ	Covariant derivative

Introduction

The widespread use of numerical methods in scientific applications during the last few decades has amplified a great deal the number and the complexity of the problems that science and technology are able to address. Although this fact can lead to think that numerical analysis is a new branch of mathematics, this idea can not be more wrong. We have evidence that a numerical approximation of the square root of two was known in Mesopotamia more than three and a half thousand years ago. During this time, this discipline has been used in problems like the estimation of irrational numbers and to solve algebraic equations, just to mention two examples. And from the nineteenth century, numerical methods have also been adapted to another problem that is very relevant for this thesis, the solution of ordinary and partial differential equations.

Since their introduction in the modelling of natural phenomena more than three hundred years ago, differential equations have been a key mathematical tool in physics and in other fields of science. There has been a lot of developments to solve them analytically, specially for linear cases with the Sturm–Liouville methods. However, in the case of non-linear PDEs, in general we can only solve them by imposing certain additional assumptions like symmetries or particular boundary conditions. For this reason, the introduction of numerical methods is an approach to obtain results that, although not exact, are very close to the phenomena we want to describe with the differential equations. In addition, the increase in the resolution that we use, leads us asymptotically to the correct solution. But, as a drawback, we now have to deal with myriads of fundamental arithmetical computations. Specially for solving complex problems with a proper resolution where the necessity of computational resources can exceed the current available technologies. Therefore, although this problem could be approached before; is now, with the progress and development of computers and the current technology going in its way towards the exoscale computing[1], when the possibilities of this branch of mathematics has increased exponentially. And this is essential because the power of this technology improves not only the computational speed and accuracy but also impels us to

[1]Exascale computing refers to computing systems capable of at least one exaFLOPS, 10^{18} floating point operations per second. This goal is not expected to be reached before 2020.

consider more complex models and theories.

In the field of gravitation the great revolution arrived with the work of Albert Einstein that was culminated in 1915 with his General theory of Relativity. Since then, we understand gravity as the manifestation of the curvature of the spacetime. In spite of the vast mathematical complexity that this theory presents, during the following decades several exact solutions of the field equations were found although most of them, and certainly the most physically relevant ones, are spacetimes with a high degree of symmetry. In this scenario, the use of numerical methods arise as a very powerful tool to address, at least in principle, general problems like the binary black hole problem. In this sense, the discovery of the critical behaviour in gravitational collapse by Matthew Choptuik in 1992 is a milestone on the development of the field of *Numerical Relativity*. Even now, critical collapse remains as one of the best examples of a completely new phenomenon that was first obtained numerically and only later it could be studied from an analytical point of view. Another very important breakthrough came in 2005 when Frans Pretorius presented the first dynamical evolution of a spacetime with the collision of two orbiting black holes and with the extraction of the gravitational-wave signal emitted. Since then, different problems in relativistic gravitation have been addressed using Numerical Relativity and nowadays the development of theses techniques, which also involves the analytical mathematical studies, is one of the essential branches in the study of gravitation.

In this thesis, we take advantage of numerical methods to study different phenomena on asymptotically Anti-de Sitter (AdS) spacetimes. Few years after Einstein's equations were presented, a term with a cosmological constant Λ was added. Nowadays, the vacuum solution with positive Λ is considered to represent an accelerated expanding universe similar to our own. On the other hand, AdS is the maximally symmetric solution with negative cosmological constant. From the knowledge we have from our own local universe, AdS may seem like a very exotic spacetime, sometimes called "the infinite box". Any point in the interior of AdS is at infinite distance from the AdS boundary but this boundary can be reached by light rays coming from the bulk. In the interior, the cosmological constant acts like a spring, a particle thrown away from the centre always falls back in a fixed period of time. Ignored for years, in the last few decades this spacetime has obtained more and more attention. For example, the Randall–Sundrum models present a 3+1 dimensional brane embedded in a five dimensional AdS spacetime. Gravity lives in the whole five dimensional spacetime although it is localised near the brane, which makes these models compatible with the observations with a maximum limit for the AdS radious of $\ell = 0.01$ mm. Instead, matter fields are confined to live on the brane. This is a proposal to deal with the hierarchy problem of why gravity is several orders of magnitude weaker than the rest of interactions. This is an example of how even the, a priori, most unrealistic results of physics can surprisingly show up in our reality. In any case, this is not the only reason why AdS has become

important in the last years. In the context of string theory and the thermodynamics of black holes, Juan Maldacena introduced in 1995 the gauge/gravity duality. This establishes a holographic correspondence between a gauge theory without gravity and a pure gravitational theory in higher dimensions. In the most studied examples of this duality the gravitational theory is required to be an asymptotically AdS spacetime. Examples of the application of this duality can be found in different fields of physics like particle collisions in accelerators, superconductors, condensed matter and quantum information. From this point of view, Numerical Relativity on AdS spacetimes is used as a tool to study systems in other fields of physics. Either because of its cosmological relevance or because of its use as an instrument, the physical properties of AdS need to be understood and in the present thesis we have studied some aspects of the dynamics of AdS spacetimes.

In Chapter 1 we start by giving an introduction to the concepts that are going to be used during the thesis. We begin by introducing the key elements of Albert Einstein's General Relativity that are needed for the rest of the chapters. We also present a brief review of the mathematical preparations to solve Einstein's equations numerically in digital computers. The main motivation is to bring to the attention of the reader some of the most important issues that this problem involves more than to give a full guide, an impossible task in the space that can be dedicated in this thesis. At the end of the first chapter we present the pseudo-spectral collocation method, one of the most powerful tools to solve numerically partial differential equations. This method is going to be used in all the chapters of the thesis and therefore is worth to describe in some detail its main properties and mathematical foundations in order to understand its application during the thesis.

Chapter 2 is dedicated to the problem of the gravitational collapse on asymptotically Anti-de Sitter spacetimes. To that end, we need first to introduce the revolutionary work of Choptuik on critical collapse and describe in detail the structure of AdS. Once this is established, we describe a new method to simulate the gravitational collapse of massless scalar fields in AdS. This method uses two completely different formulations of Einstein's equations. The simulation start with a Cauchy evolution and when the collapse is taking place, it performs a change of coordinates to a characteristic one to track the formation of the apparent horizon. With this new scheme, we have discovered a new power law for the mass of the formed black holes in configurations with less initial energy than the critical one. This is a new phenomenon, not present in flat spacetime, for which we give numerical evidence and that brings some intriguing questions about the critical collapse in AdS and in another confined geometries.

AdS is not studied just for its own importance but also because of its use as a dual tool to address other interesting problems. And this is exactly what we have proposed in Chapter 3. There, we focus on the problem of heavy ions collisions. When these particles collide at very high velocities, like it happens at

the LHC and RHIC, the system forms a plasma of quarks and gluons (QGP). This plasma is not only a good test case for the theory of the nuclear interactions, the quantum chromodynamics, but it also has interest because current cosmological models incorporate it in the early states of the Universe. The QGP is described with high accuracy as a perfect fluid but the description of the dynamics between the moment of the collision and the formation of the QGP remains a challenge. The strong interactions between quarks and gluons in this regime make it very difficult the treatment using perturbation theory. It is for this reason that other methods, in particular the gauge/gravity correspondence, where we use a 4+1 asymptotically AdS spacetimes to model the collision, are getting a lot of attention as an alternative to deal with this phenomenon. One of the problems that these holographic collisions usually exhibit is that the gauge models represent conformal field theories when the real quantum chromodynamics is not. In this chapter, we present our work where the first collisions in a non-conformal model has been simulated.

One of the problems to get a high accuracy with numerical methods on a digital computer is directly related with the number of precision digits that we use in the computations. This limitation generates what is known as the machine round-off error, which can only be improved by increasing the number of digits of our representation of the real numbers. Nowadays, in most computers, these real numbers are represented in floating-point format, similar as they are written in scientific notation, with 64-bits. This is equivalent to around sixteen digits of precision. This accuracy is more than enough to deal with most of the problems that we usually address making us forget that we are not computing with exact real numbers but with a limited representation of them. There are physical problems that are very sensitive to the initial conditions or that are very delicate to some of the parameters of the system where this precision can be very limiting and we need to go beyond the standard precision. Also, this precision can be not enough when we have to deal with cases where there are two very different scales in our problem that cannot be separated. The main problem to use higher precision is usually the reduction of the computational speed. Given that current processing units (CPUs) are adapted to double precision, computations with a different type of data types always involve some software layer than reduces our efficiency in more than two orders of magnitude. Based on our experience and on all the previous work, in Chapter 4 we argue that pseudo-spectral methods can be a very powerful option when we perform computations with arbitrary precision arithmetic. Due to their exponential convergence for smooth problems, we can reach very high accuracy with very few discretisation points as compared with other methods. The potential that pseudo-spectral methods offer for the computations with arbitrary precision arithmetic are tested using Numerical Relativity examples where we give a glimpse of the full possibilities that these methods can offer.

As we have presented in all the previous paragraphs, in this thesis we have studied different problems in Anti-de Sitter spacetimes using Numerical Relativity

where we have shown the great value of the numerical methods and, more precisely, pseudo-spectral collocation methods, in gravitation. We also show the new results that we have discovered in the topics of gravitational collapse and the AdS/CFT and our novel proposal to address problems with arbitrary precision arithmetic.

Resumen

El uso generalizado de métodos numéricos en aplicaciones científicas y tecnológicas en las últimas décadas ha incrementado enormemente el número y la complejidad de los problemas que la ciencia y la tecnología es capaz de afrontar. Aunque este hecho pueda llevar a pensar que el cálculo numérico es una rama novedosa de las matemáticas, está idea no podía estar más equivocada. Tenemos evidencias de que una aproximación numérica de la raíz cuadrada de dos ya era conocida en Mesopotamia hace más de tres mil quinientos años. A lo largo de este tiempo, esta disciplina ha sido usada en problemas como la estimación de números irracionales o la resolución ecuaciones algebraicas, por poner un par de ejemplos. Y desde el siglo diecinueve, los métodos numéricos también ha sido adaptados a otro problema que va a ser muy relevante en esta tesis, la solución de ecuaciones diferenciales ordinarias y en derivadas parciales.

Desde que se introdujeran en la modelización de fenómenos naturales hace más de trescientos años, las ecuaciones diferenciales han sido una herramienta clave en física y en otras ramas de la ciencia. En este tiempo, ha habido un gran desarrollo en su resolución analítica, especialmente en el caso lineal con los métodos de Sturm–Liouville. No obstante, para sistemas de ecuaciones diferenciales en derivadas parciales no lineales, en general sólo podemos resolver casos en los que hemos impuestos algún tipo de simetría o condiciones de contorno especiales. Por este motivo, la inclusión de métodos numéricos es un enfoque para obtener soluciones que, aunque no son exactas, se aproximan mucho al fenómeno que queremos describir con las ecuaciones diferenciales. Además, el incremento de la resolución utilizada hace que nos acerquemos asintóticamente a la solución correcta de una manera controlada. Su principal desventaja es que hace que tengamos que lidiar con una miríada de operaciones aritméticas fundamentales. Especialmente cuando resolvemos problemas complejos con una resolución aceptable, la necesidad de recursos computaciones pueden fácilmente exceder las tecnologías actuales. Por eso aunque podíamos utilizar estos métodos anteriormente; es ahora, gracias al progreso de los ordenadores y de la tecnología actual que se encuentra en su

camino hacia la computación Exascale [2], cuando las posibilidades de esta rama de las matemáticas se han incrementado exponencialmente. Y eso es esencial porque la potencia de esta tecnología no sólo mejora la velocidad y la resolución que podemos alcanzar sino que también nos impulsa a considerar modelos y teorías más complejas.

En el campo de la gravitación, la gran revolución llegó en 1915 cuando Albert Einstein culminó su trabajo en la teoría de la Relatividad General. Desde entonces, la gravedad es interpretada como una manifestación de la curvatura del espacio-tiempo. A pesar de su enorme complejidad matemática, en los últimos cien años se han encontrado muchas soluciones exactas aunque la mayoría de ellas, y sin duda las más relevantes físicamente, corresponden a casos con un alto grado de simetría. En este escenario, el uso de métodos numéricos se alza como una herramienta muy potente para, al menos en principio, poder enfrentarse a problemas generales como sistemas binarios de agujeros negros. En este sentido, el descubrimiento del comportamiento crítico en el colapso gravitacional por Matthew Choptuik en 1992 es un momento clave en el desarrollo del campo de la *Relatividad Numérica*. Todavía hoy, el colapso crítico es uno de los mejores ejemplos de un fenómeno totalmente nuevo que fue descubierto de manera numérica y sólo entonces pudo ser estudiado desde un punto de vista analítico. Otro hito importante llegó en 2005 cuando Frans Pretorius presentó la primera simulación dinámica de un espacio-tiempo con la colisión de dos agujeros negros y la extracción de dos las ondas gravitacionales emitidas. Desde entonces, muchos otros problemas en gravitación relativista han sido considerados usando Relatividad Numérica y, hoy en día, el desarrollo de estas técnicas, que también incluyen el tratamiento analítico, es una de las ramas matemáticas esenciales en el estudio de la gravedad.

En esta tesis, vamos a usar métodos numéricos para estudiar diferentes problemas en espacio-tiempos asintóticamente Anti-de Sitter (AdS). Unos pocos años después de la publicación de las ecuaciones de Einstein, un término con constante cosmológica Λ fue añadido. Actualmente, la solución de vacío con Λ positiva representa un universo en expansión similar al nuestro. Por otra parte, AdS es una solución maximalmente simétrica con constante cosmológica negativa. Según el conocimiento actual de nuestro universo, AdS puede parecer una solución muy exótica. A veces se le conoce como la "caja infinita". Cualquier punto del interior está a una distancia infinita de su frontera pero la luz que llega del interior puede alcanzar dicha frontera. En el interior, la constante cosmológica actúa como un muelle. Si lanzamos una partícula desde el origen de coordenadas, ésta volverá en un tiempo fijo. Ampliamente ignorado durante todo el siglo XX, en las últimas décadas se le está prestando mucha atención. Por ejemplos, los modelos de Randall–Sundrum presentan una brana de 3+1 dimensiones embebida en un espacio-tiempo AdS de

[2]Computación Exascale se refiere a la posibilidad de llegar a construir equipos que tengan una potencia de un exaFLOPS, 10^{18} operaciones en coma flotante por segundo. Este límite no se espera que sea superado antes de 2020.

cinco dimensiones. La gravedad vive en el espacio cincodimensional completo pero se localiza muy cerca de brana, lo que hace a estos modelos con las observaciones con un límite superior para el radio de AdS de $\ell = 0.01$ mm. Por el contrario, la materia está confinada en la brana. Esto es una propuesta para tratar el problema de la jerarquía, la enorme diferencia en órdenes de magnitud entre la intensidad de la gravedad y la del resto de interacciones fundamentales. Es también un buen ejemplo de como hasta un espacio-tiempo tan extraño puede llegar a ser importante en la descripción de la realidad. En cualquier caso, esa no es la única razón por la que AdS ha atraído miradas en los últimos años. En el contexto de la teoría de cuerdas y la termodinámica de los agujeros negros, Juan Maldacena introdujo en 1995 la dualidad gauge/gravedad. Ésta establece una dualidad holográfica entre una teoría gauge sin gravedad y una teoría gravitatoria en más dimensiones. Y en los casos más estudiados, la teoría gravitatoria tiene que ser asintóticamente AdS. Ejemplos de fenómenos que pueden ser descritos por esta dualidad pueden ser encontrados en en diversos campos de la física como las colisiones de partículas que ocurren en los aceleradores, superconductores, materia condensada e información cuántica. Desde este punto de vista, la Relatividad Numérica en AdS se utiliza como una herramienta para estudiar sistemas de otros campos. Ya sea por su importancia física o por su uso como instrumento, entender las características de este espacio-tiempo es muy importante y en esta tesis hemos estudiado algunos aspectos de la dinámica de AdS.

En el capítulo 1 vamos a dar una breve introducción a las conceptos que van a ser claves durante toda la tesis, empezando por los elementos básicos de la Relatividad General de Albert Einstein que son necesario para el resto de los capítulos. También presentamos una breve revisión de los desarrollos matemáticos necesarios para resolver las ecuaciones de Einstein numéricamente en ordenadores digitales. La principal motivación aquí es atraer a la atención del lector algunos de los problemas más comunes más que dar una completa guía del tema, algo imposible en el espacio que se dedica. Al final del capítulo, presentamos los métodos de colocación pseudo-espectrales, una de las más potentes herramientas para resolver numéricamente ecuaciones diferenciales en derivadas parciales. Este método va a ser ampliamente utilizado en todos los capítulos de la tesis y por tanto merece la pena describir en detalle sus propiedades principales y sus principios matemáticos básicos para entender su aplicación durante la tesis.

El capítulo 2 está dedicado al problema del colapso gravitatorio en espacio-tiempos asintóticamente Anti-de Siter. Para ello, necesitamos primero necesitamos introducir el revolucionario trabajo de Choptuik en el colapso crítico para posteriormente describir la estructura de AdS. Una vez todo esto está establecido, describimos en detalle el nuevo método que hemos desarrollado para simular el colapso gravitacional de campos escalares sin masa. Este método utiliza dos formulaciones de las ecuaciones de campo de Einstein. La simulación comienza con una evolución de Cauchy y, para cuando ésta detecta que el colapso está empezando, realiza un cambio de coordenadas a un esquema característico para monitorizar la

formación del horizonte aparente. Con este nuevo método, hemos descubierto una nueva ley de potencias universal para la masa de los agujeros negros que se forman con configuraciones de energía ligeramente menores que las críticas. Esto es un fenómeno nuevo que no está presente en espacio-tiempo plano para el cual hemos dado evidencia numérica y origina algunas preguntas muy interesantes acerca del colapso crítico en AdS y en otras geometrías confinadas.

Pero AdS no solamente se estudia por su propia importancia sino también por su utilización como herramienta dual para tratar con otros problemas interesantes. Y esto es precisamente lo que hacemos en el capítulo 3. Aquí, nos enfocamos en el problema de la colisión de iones pesados. Cuando estas partículas colisionan a velocidades muy altas, como pasa en aceleradores como el LHC y el RHIC, se forma un plasma de quarks y gluones. Este plasma no es sólo un buen campo de pruebas para la teoría de las interacciones nucleares fuertes, la cromodinámica cuántica, sino también es interesante porque los modelos cosmológicos actuales lo incorporan en las etapas iniciales de la Historia del Universo. El plasma de quarks y gluones puede describirse con bastante precisión como un fluido perfecto pero la descripción de la dinámica entre el momento de la colisión y su formación todavía es un desafío. Las interacciones fuertemente acopladas de los quarks y los gluones en este régimen hacen que sea muy complicado el tratamiento usando teoría de perturbaciones. Es por esa razón que otros métodos están obteniendo mucha atención, en particular la correspondencia gauge/gravedad donde utilizamos un espacio-tiempo asintóticamente AdS en 4+1 dimensiones para modelizar la colisión. Uno de los principales problemas que éstas colisiones holográficas exhiben es que los modelos gauge representan teorías de campos conformes mientras que la cromodinámica cuántica no lo es. En este capítulo, presentamos nuestro trabajo donde las primeras colisiones en una teoría no conforme han sido simuladas.

Uno de los problemas para obtener una buena precisión numéricamente en un ordenador está relacionada con el número de dígitos que usamos en las variable de nuestro cálculo. Esta limitación genera lo que se conoce como error de redondeo, que solo puede ser mejorado incrementando el número de dígitos que usamos en la representación. Actualmente, en la mayoría de los ordenadores, los números reales son representado en formato de coma flotante, muy similar a la notación científica, con 64 bits. Esto es equivalente aproximadamente a quince o dieciséis dígitos de precisión. En general, eso es más que suficiente para tratar con la mayoría de los problemas a los que nos enfrentamos actualmente y eso hace que olvidemos que nunca estamos tratando con números reales sino con representaciones limitadas de ellos. Hay algunos problemas que ya sea porque la física es muy sensible a las condiciones iniciales o a algún parámetro esta precisión puede limitar nuestro estudio y que nos haga necesitar ir más allá de la precisión estándar. También en casos en los que tenemos que lidiar con fenómenos que operan en escalas muy diferentes y no pueden ser separados puede limitarnos operar con una precisión fija. El problema principal al usar más precisión es la reducción en la velocidad de

cálculo. Las CPUs actuales son capaces de realizar operaciones básicas de doble precisión, 64 bits, y por tanto cualquier otra precisión requerirá algún tipo de capa de software que puede reducir nuestra eficiencia hasta dos ordenes de magnitud. Basándonos en nuestra experiencia y en todo el trabajo previo presentando en esta tesis, en el capítulo 4 razonamos que los métodos espectrales pueden ser una opción muy potente para realizar cálculos con un número muy grande de dígitos. Debido a que éstos ofrecen convergencia espectral para funciones diferenciales, podemos alcanzar muy buena precisión usando muy pocos puntos en la discretización comparado con otros métodos. Su potencial para el tratamiento de problemas con precisión arbitraria ha sido probado usando problemas de gravitación donde hemos podido vislumbrar las posibilidades que estos métodos nos ofrecen.

En resumen, en esta tesis hemos estudiando diferentes problemas relacionados con los espacio-tiempos asintóticamente Anti-de Sitter usando Relatividad Numérica donde hemos presentado el enorme valor que tienen en gravitación los métodos numéricos y, más precisamente, los métodos de colocación pseudo-espectrales. También hemos mostrado nuevos resultados en los importantes temas del colapso gravitatorio y de la dualidad AdS/CFT y, además, nuestra novedosa propuesta para tratar problemas con precisión arbitraria.

Chapter 1

Numerical Relativity Methods

> We are a way for the cosmos to know itself
>
> Carl Sagan

Albert Einstein's General Relativity (GR) changed not only the way we understand the physics of gravitation but also how we *formulate* it. And during the last hundred years, a lot of scientists that came after Einstein continue to comprehend and to discover completely new phenomena that this beautiful theory brought to us. In this chapter we are going to make a brief introduction to the theory of **General Relativity** and how we can manipulate the field equations into a form that computers can digest for helping us to study the physics behind it. We start by making a historical description of the gravity theory before GR and to introduce the geometrical language in which we express Einstein's Field Equations. After reviewing some known analytical solutions that are relevant for this thesis, we explain how we need to formulate the equations to solve them numerically and, finally, we introduce the main numerical methods to discretise the partial differential equations behind the theory. Unless otherwise stated, along this chapter we are taking physical units in which the speed of light c is equal to unity.

1.1 General Relativity Basics

1.1.1 Gravity as Geometry

When **Isaac Newton** in the year 1687 wrote in his **Philosophiae Naturalis Principia Mathematica** [1] the well-known law of universal gravitation, he

established the perfect culmination of the previous work of many others like **Nicolaus Copernicus**, **Galileo Galilei** and **Johannes Kepler** that, in their determination of careful observation and scientific reasoning, were able to unlock the building blocks of how the Universe works. But the key feature that makes Newton's law so important and revolutionary is not the exact formula itself but the fact that his theory allowed him to explain phenomena apparently so different as the movement of the planets, why an apple falls down from a tree or why the Moon does not. The process that leads us to understand that Earth and heavens were not separated entities with different laws but a single physical reality is a crucial idea not only for science but also in our history as a civilisation.

The law of universal gravitation establishes that any two bodies attract themselves with a force proportional to their masses (m_1, m_2) and inversely proportional to the square of the distance that separates them (r) and can be written as:

$$F_{grav} \propto \frac{m_1\, m_2}{r^2}. \tag{1.1}$$

Since the beginning, Newton and others recognised immediately the intrinsic problems of the previous physical law. The main one was the concept of a force actuating instantaneously at arbitrary distances. For the previous to be true, it supposes that the gravitational force is acting instantly and without any material interaction between the bodies. This was of course an absurdity and Newton itself wrote in a letter *"Gravity must be caused by an agent acting constantly according to certain laws; but whether this agent be material or immaterial, I have left to the consideration of my readers"* [2]. This lack of a mechanism that explained the gravitational interaction was an open question for the following two hundred years. There were a lot of different and imaginative proposals but in the end, all of them presented conflicts with observations. One of the most well-known was the mechanical explanations of screening by **Nicolas Fatio de Duillier** (1690), **Georges-Louis Le Sage** (1748) [3] and others. Roughly speaking, they proposed that the universe is full of tiny particles moving at very high speeds. The density of these particles is high enough that for an isolated body the net force cancels in all directions. If we consider a second body, the direction to it is partially blocked so there are less particles coming from there. This produces a net force in the direction of the bodies that is supposed to be the force that we explained in the law of universal gravitation. Although this theory solved some of the problems, generated a lot more like the presence of a drag, thermal issues, etc. Although during the years modifications of the previous model and new ones were presented, none of them was really accepted and the real explanation of the gravitational force was hidden, until **Albert Einstein**.

Between 1907 and 1915 Einstein developed the ideas that allowed him to extend his Special Relativity theory to include gravitation. In his theory of General Relativity [4, 5] he did not only need to create a new theory, he also had to introduce a change in the mathematical language. From that moment, gravitation was not longer

understood as a force but as the geometrical curvature of spacetime and Newton's force is just the phenomenological result of the presence of matter acting through the spacetime at the speed of light.

1.1.2 A Geometrical Language

The central role of geometry in the theory of General Relativity replaces classical physics concepts as forces, particles and gravitational potentials by a completely different language. Here we are going to introduce some basic concepts that will allow us to formulate gravity as a geometrical theory in the next section [6, 7, 8].

The key ingredient is going to be the spacetime metric $g_{\mu\nu}$, a four dimensional tensor that determines the invariant spacetime interval between two spacetime events:

$$ds^2 = g_{\mu\nu} dx^\mu dx^\nu, \tag{1.2}$$

where dx^μ is the infinitesimal interval between two events with spacetime coordinates x^μ and $x^\mu + dx^\mu$. Greek indices denote spacetime coordinates in a range 0-3.

For a general spacetime we can make a transformation to a system of coordinates for any particular event to be *locally* at an inertial reference frame, where the metric is the Minkowski one:

$$g_{\mu\nu} = \eta_{\mu\nu} = \mathrm{diag}(-1, 1, 1, 1), \tag{1.3}$$

and its first derivative vanish at that point:

$$\partial_\lambda g_{\mu\nu} = 0. \tag{1.4}$$

In these coordinates, the nongravitational laws of physics are *locally* the same as in special relativity. This is commonly known as the **Einstein Equivalence Principle** [9, 10]. Only in the case of empty flat spacetime, it is always possible to choose our coordinates to be everywhere as the Minkowski metric.

In a coordinate basis, the basis vectors $e_{(\mu)}$ can be written as the tangent vectors to coordinates lines and can be written as:

$$e_{(\mu)} = \partial_\mu. \tag{1.5}$$

The components of the metric tensor are given by the scalar dot products $(\cdot)$ between the four the basis vectors that span the vector space tangent to the spacetime manifold:

$$g_{\mu\nu} = e_{(\mu)} \cdot e_{(\nu)}, \tag{1.6}$$

where indices without the parenthesis denotes the components of the tensor meanwhile (μ) denotes the (μ)th vector of the basis.

With our vector basis, we define four-vectors as:

$$A = A^{\mu} e_{(\mu)}, \tag{1.7}$$

where A^{μ} are the contravariant components of the vector and $e_{(\mu)}$ are, again, the (μ)th vector of our vector basis. In the same way, we can define a basis of covectors $\omega^{(\mu)}$ dual to our vector basis that satisfies:

$$\omega^{(\mu)} e_{(\nu)} = \delta^{(\mu)}_{\ \ (\nu)}. \tag{1.8}$$

Then, we can define also covectors:

$$\tilde{A} = A_{\mu} \omega^{(\mu)}, \tag{1.9}$$

and, if the vector and covector represent the same information, they can be related via the metric tensor as:

$$A_{\mu} = g_{\mu\nu} A^{\nu}, \tag{1.10}$$

where, in the index notation, repeated indices mean a summation over the four values of that index.

In the same way, we can define tensors of any rank with covariant and contravariant indices and relate them via the metric tensor:

$$B^{\mu\nu}_{\ \ \ \sigma} = g_{\rho\sigma}\ B^{\mu\nu\rho} = g_{\rho\sigma}\ g^{\nu\gamma}\ B^{\mu}_{\ \ \gamma}{}^{\rho}, \tag{1.11}$$

For a general change of coordinates[1] $x^{\mu} \to \bar{x}^{\sigma'}$, vectors and tensors transform as:

$$\begin{aligned} A^{\sigma'} &= M^{\sigma'}_{\ \ \mu}\ A^{\mu} \\ B^{\sigma'}_{\ \ \rho'} &= M^{\sigma'}_{\ \ \mu}\ B^{\mu}_{\ \ \nu}\ M^{\nu}_{\ \ \rho'}, \end{aligned} \tag{1.12}$$

where $M^{\sigma'}_{\ \ \nu} = \frac{\partial \bar{x}^{\sigma'}}{\partial x^{\nu}}$ is a matrix that represents the change of coordinates.

The concept of moving a vector along a path, keeping it constant all the while is known as parallel transport and depend strongly in the path taken. The covariant derivative measures the rate of change of a tensor field with respect to this parallel transport. It is always a tensor of a one rank higher than the original tensor and it is defined as:

$$\nabla_{\sigma} A^{\mu} = \partial_{\sigma} A^{\mu} + \Gamma^{\mu}_{\ \ \rho\sigma} A^{\rho}, \tag{1.13}$$

in the case of vectors and:

$$\nabla_{\sigma} B^{\mu}_{\ \ \nu} = \partial_{\sigma} A^{\mu}_{\ \ \nu} + \Gamma^{\mu}_{\ \ \rho\sigma} A^{\rho}_{\ \ \nu} - \Gamma^{\rho}_{\ \ \sigma\nu} A^{\mu}_{\ \ \rho}, \tag{1.14}$$

[1] This describes a change of the coordinates without changing the vector basis.

in the case of tensors. $\Gamma^{\mu}{}_{\rho\sigma}$ are the components of the Levi-Civita connection, defined as:

$$\Gamma^{\mu}{}_{\rho\sigma} = \frac{1}{2} g^{\mu\nu} \left(\partial_\rho g_{\nu\sigma} + \partial_\sigma g_{\nu\rho} - \partial_\nu g_{\sigma\rho} \right), \tag{1.15}$$

notice here that $\Gamma^{\mu}{}_{\rho\sigma}$ is not a tensor since it does not transform under general change of coordinates as Eqs. (1.12) dictate.

As a consequence of the equivalence principle, the real curvature of the spacetime, and therefore gravity, can only be measured by second order derivatives of the metric. The geometrical object that encodes the relevant information of the spacetime curvature is the Riemann curvature tensor and is defined as:

$$R^{\mu}{}_{\nu\sigma\rho} = \partial_\sigma \Gamma^{\mu}{}_{\nu\rho} - \partial_\rho \Gamma^{\mu}{}_{\nu\sigma} + \Gamma^{\mu}{}_{\gamma\sigma} \Gamma^{\gamma}{}_{\nu\rho} + \Gamma^{\mu}{}_{\gamma\rho} \Gamma^{\gamma}{}_{\nu\sigma}, \tag{1.16}$$

and from it we construct two other important objects: the Ricci tensor:

$$R_{\mu\nu} = R^{\rho}{}_{\mu\rho\nu}, \tag{1.17}$$

and the scalar of curvature:

$$R = R^{\rho}{}_{\rho}. \tag{1.18}$$

Although the Riemann tensor has rank four, the number of independent components is lower than the total possible number because of all the symmetries and identities that it satisfies. These symmetries are:

$$R_{\mu\nu\sigma\rho} = -R_{\nu\mu\sigma\rho}, \tag{1.19}$$

$$R_{\mu\nu\sigma\rho} = -R_{\mu\nu\rho\sigma}, \tag{1.20}$$

$$R_{\mu\nu\sigma\rho} = +R_{\sigma\rho\mu\nu}, \tag{1.21}$$

and also the first Bianchi identities:

$$R_{\mu\nu\sigma\rho} + R_{\mu\rho\nu\sigma} + R_{\mu\sigma\rho\nu} = 0, \tag{1.22}$$

as well as the second Bianchi identities:

$$\nabla_\lambda R_{\mu\nu\sigma\rho} + \nabla_\rho R_{\mu\nu\lambda\sigma} \nabla_\sigma R_{\mu\nu\sigma\rho\lambda} = 0, \tag{1.23}$$

that contracting indices $\mu\sigma$ and $\nu\lambda$ with the metric tensor lead to the following important expression:

$$\nabla^\nu R_{\nu\rho} = \frac{1}{2} \nabla_\rho R. \tag{1.24}$$

1.1.3 The Einstein Field Equations

With the elements introduced in the previous section, we have all the ingredients needed to formulate gravity as geometry [6, 11, 12]. As in Newtonian gravitation we have that matter generates a force or a gravitational field, in Einstein's General Relativity we need to relate the curvature of the spacetime with the presence of matter and, as a consequence of Special Relativity, also with energy. Then our final goal is to obtain an equation that determines the geometry of the spacetime in terms of a given distribution of matter and energy.

The distribution of matter and energy can be modelled, convariantly, by the stress-energy tensor $T_{\mu\nu}$, which takes different expressions depending on the matter model we consider. Just to give a few examples, for vacuum is simple:

$$T_{\mu\nu} = 0, \tag{1.25}$$

for a scalar field ϕ with mass m, we have:

$$T_{\mu\nu} = \partial_\mu\phi\partial_\nu\phi - \frac{1}{2}\left(g_{\mu\nu}\partial_\alpha\phi\partial^\alpha\phi + m^2\phi^2\right), \tag{1.26}$$

and in the case of a perfect fluid the expression is:

$$T_{\mu\nu} = (\rho + p)\, u_{\mu\nu} + p g_{\mu\nu}, \tag{1.27}$$

where p is the fluid pressure, ρ its density and u^μ its four velocity.

As we saw in Sec. 1.1.2, the simplest way to have non trivial (covariant) curvature requires second order derivatives of the metric. As we need a tensor of the same rank as the stress-energy tensor, the object to start with is the Ricci tensor. Then, it seems straightforward to write:

$$R_{\mu\nu} = \kappa T_{\mu\nu}, \tag{1.28}$$

as Einstein suggested at one point. But this equation has several issues. The conservation of energy is going to require that the divergence of the stress-energy tensor vanishes:

$$\nabla^\mu T_{\mu\nu} = 0, \tag{1.29}$$

but this condition implies via Eq. (1.28) that the divergence of the Ricci tensor also vanishes:

$$\nabla^\mu R_{\mu\nu} = 0, \tag{1.30}$$

which makes no sense for a general geometry. As we saw in Eq. (1.24), as a consequence of the Bianchi identities we can write:

$$\nabla^\mu R_{\mu\nu} = \frac{1}{2}\nabla_\nu R, \tag{1.31}$$

and for Eq. (1.28) the scalar of curvature is proportional to the trace of the stress energy tensor: $R = \kappa T$ and therefore:

$$\nabla^\mu R_{\mu\nu} = \frac{1}{2}\nabla_\nu R = \frac{1}{2}\kappa\nabla_\nu T, \tag{1.32}$$

or just:

$$\partial_\nu T = 0, \tag{1.33}$$

which means that the trace of the stress energy tensor needs to be constant in the whole spacetime. This, of course, is not true aside from the case of vacuum where $T = 0$ everywhere. Therefore we need to try something a different. If we require Eq. (1.29) to be true, we need the left-hand side of the equation to be a tensor also with a null divergence. Fortunately, we have already seen something that can be useful in Eq. (1.31). Using that expression as the geometrical part, which is usually known as the Einstein tensor:

$$G_{\mu\nu} = R_{\mu\nu} - \frac{1}{2}g_{\mu\nu}R, \tag{1.34}$$

for which it is obvious that:

$$\nabla^\mu G_{\mu\nu} = 0, \tag{1.35}$$

and therefore we can write consistently:

$$G_{\mu\nu} = \kappa T_{\mu\nu}. \tag{1.36}$$

From that expression, we can see that the scalar of curvature is:

$$R = -\kappa T, \tag{1.37}$$

and therefore rewrite Eq. (1.36) as:

$$R_{\mu\nu} = \kappa\left(T_{\mu\nu} - \frac{1}{2}g_{\mu\nu}T\right), \tag{1.38}$$

that represents the exact same information as Eq. (1.36) but written differently.

The only thing left is to determine the meaning of the proportionality constant κ. As the Newtonian theory of gravitation is valid with high precision in some scenarios, Einstein's General Relativity needs to be an *extension* of the previous, reducing into the classical limit in the conditions where the first seems to be valid. The limits that we need to force in GR to reduce to Newtonian theory are basically two. The first is the weak-field, for example for the gravitational field produced by a massive body this is true if we are far enough from the object. In the solar system, the influence of GR in the calculus of the orbits of the planets is important only in Mercury. The second limit to consider is slow motion. This is understandable if we consider that in Newtonian theory the speed of light is effectively infinite.

The weak-field approximation indicates that the metric in a suitable coordinate system is a perturbation of the Minkowski one:

$$g_{00} = -1 - 2\Phi, \tag{1.39}$$

where Φ is the Newtonian gravitational potential. For a massive object with a distribution of matter ρ that does not carry a flux of momentum or energy through space, the only non-zero component of the stress-energy tensor is the energy density component:

$$T_{00} = \rho, \tag{1.40}$$

and then its trace is just:

$$T = -\rho, \tag{1.41}$$

where, since we are in the weak-field limit, we have assumed that the energy density is much bigger than the gravitational potential:

$$\rho >> \Phi \tag{1.42}$$

We can compute the $(0,0)$ component of the Ricci scalar using Eqs. 1.16, 1.17:

$$R_{00} = \nabla^2\Phi = \delta^{ij}\partial_i\partial_j\Phi, \tag{1.43}$$

where δ^{ij} is the Kronecker delta and Latin indices denotes space coordinates. The $(0,0)$ component of Eq. (1.38) becomes:

$$R_{00} = \nabla^2\Phi = \frac{1}{2}\kappa\rho. \tag{1.44}$$

We can compare this with the Poisson equation that describe the gravitational potential generated by a mass distribution with density ρ:

$$\nabla^2\Phi = 4\pi G\rho, \tag{1.45}$$

where G, of course is Newton's gravitational constant, and then we can identity the constant κ:

$$\kappa = 8\pi G. \tag{1.46}$$

With all of this we can finally write the final form of the Einstein Field Equations (EFEs) as:

$$G_{\mu\nu} = R_{\mu\nu} - \frac{1}{2}\, g_{\mu\nu}R = 8\pi G T_{\mu\nu}, \tag{1.47}$$

where, since both $G_{\mu\nu}$ and $T_{\mu\nu}$ are symmetric tensors, the EFEs represent a set of ten differential equations. Both the Ricci tensor and the scalar of curvature are constructed from contractions of the Riemann tensor that involve first and second order derivatives of the metric so that one can imagine that the Einstein tensor

includes the components of the metric and its derivatives mixed between them in a non-linear way. This non-linearity means that the solutions of the EFEs can be a very complicated task for general situations, and sometimes also in simple cases. For example, the superposition principle no longer applies to gravity. In Newton's theory, the gravitational potential due to several masses is just the sum of the individual potentials generated by the masses independently and this is not true in GR. This non-linearity of the equations present in GR is just the mathematical realisation of the backreaction of the action of gravity on itself.

Another important fact to consider is that, due to the second Bianchi identities, $\nabla^{\mu} G_{\mu\nu} = 0$; we have four constrains. This is pertinent because there is always an ambiguity choosing the coordinates that label our spacetime. In this way, four of our equations represent *constrain* equations and only six of them can be dynamical equations. In terms of the metric, this means that the metric has only six physical degrees of freedom. This is discussed in more detail in Sec. 1.2.1.

We can always add a constant term to the field equations:

$$R_{\mu\nu} - \frac{1}{2}\, g_{\mu\nu} R + \Lambda g_{\mu\nu} = 8\pi G T_{\mu\nu}, \tag{1.48}$$

where Λ is called the cosmological constant because it was introduced by Albert Einstein in an attempt to get an stationary solution for the spacetime geometry of the Universe. Currently, it is used for explaining a universe in accelerated expansion as our own (de Sitter solution) with $\Lambda > 0$. The solution with $\Lambda < 0$, known as Anti-de Sitter, is going to be the key spacetime in this thesis. This maximally symmetric manifold corresponding to a hyperbolic geometry has been very important in the last few years thanks to the AdS/CFT correspondence [13, 14] and some cosmological models [15] and it is described in detail in Sec. 2.2.

1.1.4 Exact Solutions of the Einstein Field Equation

The Einstein Field Equations are a set of ten non-linearly coupled partial differential equations. At first sight, it was thought that no analytical solution could exist. In fact, in the original paper of Albert Einstein, the precession of the perihelion of Mercury was calculated using an approximation. Currently, there is plenty of spacetimes with exact analytical expressions but most of them, and certainly the most interesting ones, are cases of high degree of symmetry that allow us to simplify the equations in one way or another so that they become solvable.

The first of these exact solutions to be discovered, apart from the **Minkowski** metric that of course is a trivial solution of the EFEs, was introduced by Karl Schwarzschild in 1916, about a month after the publication of the final version of the EFEs. He considered the vacuum spacetime with spherical symmetry outside

a object of mass M and now it is known as the **Schwarzschild** solution and in coordinates $\{t, r, \theta, \phi\}$ can be expressed as:

$$ds^2 = -\left(1 - \frac{2GM}{r}\right) dt^2 + \left(1 - \frac{2GM}{r}\right)^{-1} dr^2 + r^2 d\Omega^2, \tag{1.49}$$

where $d\Omega^2$ is the metric on the unit two-sphere and can be written in terms of the angles θ and φ as:

$$ds^2 = d\theta^2 + \sin^2\theta d\varphi^2 \tag{1.50}$$

The first obvious application of this solution is to use it to model the solar system as the vacuum solution outside the Sun and with it, the calculation of the precession of the perihelion of Mercury was redone. The solution is obtained as a vacuum solution an therefore it is only valid for the exterior of the star. If we observe the expression of Eq. (1.49), there is a divergence in g_{rr} for $r = 2GM$. In this case, there is no problem because the radius of the star is much greater than $2GM$. Here we can see straightforward features. In the limit $M \to 0$ we recover the Minkowski metric as expected. In the limit $r \to \infty$ we also approach to Minkowski. Spacetimes that shares the same properties at infinity are known as asymptotically flat.

A careful study of this solution indicates that Schwarzschild is the **only** possible vacuum solution with spherical symmetry. This is known as Birkhoff's theorem [16]. This is a very strong remark if we take in account that no assumptions are done besides the need for spherical symmetry and vacuum. This is true even outside a non-static source as a collapsing star, as long as the collapse is spherical the solution outside will be Schwarzschild, which is static

Another different problem arises when we ask ourselves what happens if the radius of the "star" is smaller than $2GM$. In that case we call the object a black hole (BH) and several new features appear. Looking to Eq. (1.49), we observe singularities in the metric at $r = 0$ and at $r = 2GM$, but the two are very different. In general a singularity in the metric does not need to mean that physical quantities blow up at that location because it can just be a coordinate singularity due to a particular choice of coordinates. For this reason, we need to look at invariant quantities such as the curvature invariant:

$$K = R^{\mu\nu\eta\sigma} R_{\mu\nu\eta\sigma} = \frac{48G^2M^2}{r^6}. \tag{1.51}$$

This shows that the origin $r = 0$ is a real physical singularity where the curvature of the spacetime diverges to infinity.

On the other hand, we do not see any problem at $r = 2GM$ and in this case we could say now that the problem is due to the choice of coordinates, however, things are more complicated. Although these coordinates are not optimal to describe the solution, they are not a weird election: they represent the coordinates associated to

an inertial observer at infinity. If we look at the null geodesics $ds^2 = 0$ we get:

$$\frac{dr}{dt} = \pm\left(1 - \frac{2GM}{r}\right), \tag{1.52}$$

where we see that null geodesics reach $r = 2GM$ at infinite time, so this point can not be crossed, at least for the point of view of an observer at infinity. The two signs represent that there are going to be two sets of geodesics, the outgoing ($+$ sign) that are supposed to escape to infinity and the ingoing ($-$ sign) that go in the direction of the origin.

Let us introduce some new coordinates known as **Eddington-Finkelstein** coordinates [6], which are more adapted to the null geodesics described by Eq. (1.52):

$$u = t - r - 2GM \ln\left(\frac{r}{2GM} - 1\right), \tag{1.53}$$

$$v = t + r + 2GM \ln\left(\frac{r}{2GM} - 1\right). \tag{1.54}$$

In these coordinates, outgoing null geodesics are given just by $u =$ constant and infalling ones by $v =$ constant.

Rewriting the metric in (v, r) coordinates we have:

$$ds^2 = -\left(1 - \frac{2GM}{r}\right) dv^2 + 2dvdr + r^2 d\Omega^2, \tag{1.55}$$

and, although the g_{vv} metric component vanish at $r = 2GM$ the metric is regular and invertible at that point. The null geodesics look a bit different as compared with the previous case. The infalling ones:

$$\frac{dv}{dr} = 0, \tag{1.56}$$

are at $v =$ const as we advanced before. The outgoing are:

$$\frac{dr}{dv} = \frac{1}{2}\left(1 - \frac{2GM}{r}\right), \tag{1.57}$$

where we see how the outgoing really behave around $r = 2GM$. In the outside region, outgoing geodesics are not bounded and can continue to infinity but in the region $r < 2GM$, all the null geodesics end at $r = 0$ with $r = 2GM$ being the surface that separate these two regions. This is represented in Fig. 1.1.

Now we can interpret $r = 2GM$ as a surface that separates two casual regions and, for that reason, we call it **event horizon**. Once a particle or a light ray crosses this surface is trapped inside and cannot escape. Then, for any observer in the outside region is impossible to know what happens inside. This is the reason why

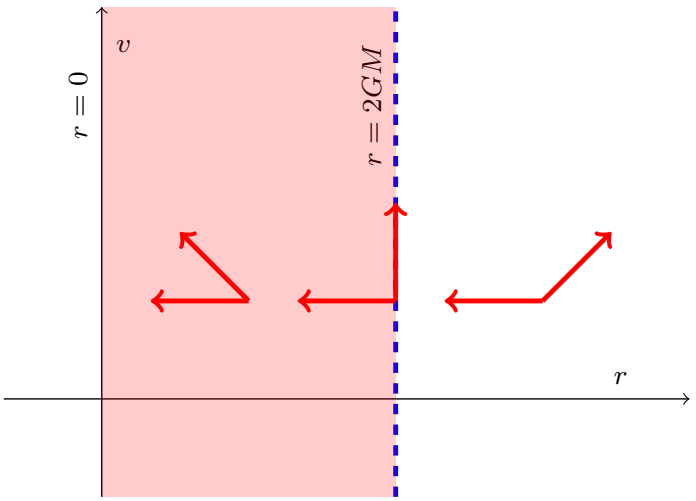

Figure 1.1: Future Lightcones for the Schwarzschild Geometry. In this diagram we can see the two causal regions of the Schwarzschild geometry. The arrows represents null geodesics. The ingoing $v = 0$ always ends at $r = 0$ in the future but the other one reaches null infinity only for $r > 2GM$. The separation between this two regions is the event horizon at $r = 2GM$.

this kind of objects are called **black holes**. As a separation between two different causal regions, the event horizon is a null 3-dimensional hypersurface that, in order to be located, requires the knowledge of the whole spacetime. This should not be confused with the notion of **apparent horizon** (AH) that is frequently used in this thesis and that we proceed to explain.

Let us consider a family of curves in an open region of the spacetime, for each of its points only passes one of curves of the family. This is known as a *congruence* [7]. If all the curves are null geodesics, we have a congruence of null geodesics. The tangent vector field to this geodesics is k^μ that, of course, is null and it is affinely parametrised by λ. We define the expansion θ of the geodesics as:

$$\theta = \nabla_\mu k^\mu. \tag{1.58}$$

The expansion represents the fractional rate of change of the congruence's cross-sectional area:

$$\theta = \frac{1}{\delta A}\frac{d}{d\lambda}\delta A, \tag{1.59}$$

where the two-dimensional area δA is transverse to k^μ. Now, we can define the concept of *trapped surface* as a closed two-dimensional surface S in which for both congruences of outgoing and ingoing null geodesics, the expansion is negative for all the points of S. The AH, is the outermost trapped surface, the boundary of the region that contains all the trapped surfaces, where the expansions vanish [17]. This

can be studied locally and therefore does not require the knowledge of the whole spacetime. The drawback is that they are slicing dependent and therefore they are not as meaningful as the concept of event horizon. Only in simple cases like in the case of static spacetimes, the event horizon can be seen as the continuous apparent horizon through time.

The introduction of the null coordinates (u, v) is going to be very important for us in the following chapters since they are very useful to track trapped surfaces. We can use them to generate two new ways of writing the Schwarzschild metric. The first one uses the radial coordinate r and the ingoing null time u (Eq. (1.54)):

$$ds^2 = -\left(1 - \frac{2GM}{r}\right) du^2 - 2dudr + r^2 d\Omega^2. \tag{1.60}$$

We can also use both Eddington-Finkelstein coordinates:

$$ds^2 = -\left(1 - \frac{2GM}{r}\right) dudv + r^2 d\Omega^2. \tag{1.61}$$

The Schwarzschild metric is not the only analytical solution that describes objects with event horizons, what we have called black holes. We can have more complex objects. We are not going to enter in details because they are not relevant for this thesis but we give here expressions of some of them for the sake of completeness. If we have a charged object in spherical symmetry, we have the **Reissner–Nordström** metric [18, 19]

$$ds^2 = -\Delta dt^2 + \Delta^{-1} dr^2 + r^2 d\Omega^2, \tag{1.62}$$

where Δ depends on the mass M and the charge Q of the object through the expression:

$$\Delta = 1 - \frac{2GM}{r} + \frac{GQ^2}{r^2}, \tag{1.63}$$

In this case, we do not have vacuum anymore because the charge of the BH generates an electromagnetic field with acts a source of energy-momentum. In Eq. (1.63) we can see that in the case $Q^2 < GM^2$ there are two metric singularities at:

$$r_\pm = GM \pm \sqrt{G^2M^2 - GQ^2}. \tag{1.64}$$

A careful study indicates that both are of them are event horizons [6] that generate a richer causal structure with three different causal region. For this reason this kind of objects are stimulating to consider but its astrophysical interest is limited. Any charged BH is expected to attract opposite sign charge very fast and neutralise itself so the possibility to observe it is very tiny.

The obvious generalisation is to look for rotating black holes. This is not only an interesting theoretical and astrophysical consideration, but also a needed one to rule out the possibility that all the behaviour that we have seen before was just an artifact of the spherical symmetry. This solution was found by Roy Kerr in 1963 [20] and since then it is known as the **Kerr metric**. It describes an stationary object with axial symmetry around the rotation axis, being M the mass of the object and a its momentum per mass unit, the metric in **Boyer–Lindquist** coordinates can be expressed as:

$$\begin{aligned} ds^2 = &-\left(1-\frac{2GMr}{\rho^2}\right)dt^2 - \frac{4GMar\sin^2\theta}{\rho^2}\left(dtd\phi\right) + \frac{\rho^2}{\Delta}dr^2 \\ &+ \frac{\sin^2\theta}{\rho^2}\left[(r^2+a^2)^2 - a^2\Delta\sin^2\theta\right]d\phi^2 + \rho^2 d\theta^2, \end{aligned} \tag{1.65}$$

with $\Delta = r^2 - 2GMr + a^2$ and $\rho^2 = r^2 + a^2\cos^2\theta$. In the limit $a \to 0$, it reduces to the Schwarzschild metric of Eq. (1.49). According to General Relativity and accepting the no-hair theorem [21], all the BHs known in the universe from the supermassive ones at the galactic centres to the stellar ones recently seen by LIGO (see Ref. [22]) are supposed to be described by the previous expression.

Another important type of spacetime are the maximally symmetric ones. This means that the spacetime has the maximum of Killing symmetries [23] and all of the points of the spacetime are indistinguishable between them. The simplest example is Minkowski spacetime but it is not the only one. The vacuum solutions with cosmological constant different from zero present constant curvature determined by the value Λ. In these spacetimes the Riemann tensor is determined only by the value of the scalar of curvature:

$$R_{\mu\nu\eta\sigma} = \frac{1}{12}R\left(g_{\mu\eta}g_{\nu\sigma} - g_{\mu\sigma}g_{\mu\sigma}\right). \tag{1.66}$$

From this and the EFEs we can deduce that the scalar of curvature is just:

$$R = 4\Lambda. \tag{1.67}$$

The solution of positive curvature is known as **de Sitter metric** and it was presented in 1917 by Willem de Sitter. It can be written in the static coordinates as:

$$ds^2 = -\left(1-\frac{\Lambda}{3}r^2\right)dt^2 + \left(1-\frac{\Lambda}{3}r^2\right)^{-1}dr^2 + r^2 d\Omega^2, \tag{1.68}$$

this solution represents a universe in accelerated expansion with a cosmological horizon at $r = \sqrt{3/\Lambda}$.

We are more interested in the case with negative cosmological constant. The

maximally symmetric spacetime with constant negative curvature it called **Anti-De Sitter** (AdS) [12] and can be represented by the same metric of Eq. (1.68) but considering $\Lambda < 0$. For the sake of clarity we introduce the AdS length scale $\ell = -3/\Lambda$. Our study requires to deal with the boundary of AdS at $r = \infty$. As computationally we can not deal with infinities, we introduce a compactified coordinate:

$$r = \tan(x), \tag{1.69}$$

and the metric becomes:

$$ds^2 = \frac{\ell}{\cos^2(x)}\left(-dt^2 + dx^2 + \sin^2 x\, d\Omega^2\right), \tag{1.70}$$

All the details about AdS spacetime are described in Chapter 2 where this spacetime is going to be very important but it is worth mention that with a negative cosmological constant Λ we also have BH solutions and the spherically symmetric uncharged is known as: Schwarzschild-AdS and can be written as:

$$ds^2 = -\left(1 - \frac{2GM}{r} + \frac{r^2}{\ell^2}\right)dt^2 + \left(1 - \frac{2GM}{r} + \frac{r^2}{\ell^2}\right)dr^2 + r^2 d\Omega^2, \tag{1.71}$$

in that expression is clear that when $r \to \infty$ the metric have the same behaviour as AdS spacetime. The same that happened before with the asymptotically flat spacetimes, in these cases we call these spacetimes to be asymptotically AdS (AAdS).

1.2 Formulations of the EFEs for Numerical Relativity

In the previous chapter, we have seen the geometrical formulation of gravity and its realisation in the form of the Einstein Field Equations. We have also seen some of the most important exact solutions that have been found during the past century. These exact solutions are very useful because they contain the full information about the spacetime structure in a very compact and elegant way. But all the solutions we presented are highly symmetric and simple. In general, to expect to have analytical expressions for the general evolution problems is a bit unrealistic taking into account the non-linear character of the EFEs. The main solution to this is to integrate numerically the equations. Although this may seem powerful enough to address general problems, in reality it is far from ideal. Big problems arise from a lot of different places. The key point from the theoretical point of view is the choice of the foliation of the spacetime and the coordinates associated with it. Actually, this was the main obstacle to have a full 3+1 simulation of binary black holes with gravitational-wave extraction until the work of Frans Pretorius in 2005 [24]. Another important issue is the question of the numerical algorithm to be used for the discretization of our equations. This problem is shared between all the different

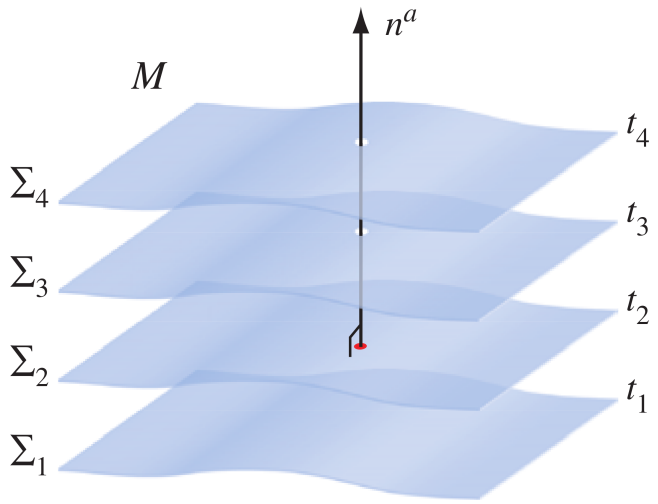

Figure 1.2: Foliation of the Spacetime in Cauchy Hypersurfaces. The hypersurfaces Σ are labelled by the time t = const. We use the evolution equations to successively construct their geometry and their extrinsic curvature that describe how the are embedded in the spacetime manifold from the initial conditions set at Σ_1. Figure taken from Ref. [8]

fields in computational physics and we are going to make a brief introduction to it in the next section.

In this introduction, we give a glimpse of the problematic of evolving numerically full 3+1 spacetimes in numerical relativity, focusing in some parts on the spherically symmetric case that is specially relevant in some chapters of the thesis. For a more detailed presentation on this topic, Refs. [8, 25, 26] can be checked.

1.2.1 The Cauchy Problem

The Einstein Field Equations, as they were presented in Sec. 1.1.3, are written in a very beautiful and compact manner but totally unpractical from the numerical point of view. In order to solve the EFEs in a computer, the first thing we need to do is to break the covariant form and set up a particular coordinate system adapted to an evolutionary problem. The first way in which we can do that is to separate the spacetime in non intersecting spacelike hypersurfaces Σ of constant time coordinate t as shown in Fig. 1.2 and formulate EFEs as a Cauchy problem. In this sense, since our goal is to obtain the components $g_{\mu\nu}$ through time, we set initial conditions on one hypersurface Σ_1, that is, we prescribe as function of the coordinates of the slice Σ_1, $g_{\mu\nu}(t_1)$ and $\partial_t\, g_{\mu\nu}(t_1)$. Then, we use the evolution equations to construct the geometry of the next hypersurface.

The metric is a symmetric tensor and then we have ten independent metric components hence we need ten evolution equations to have a well-posed formulation of the Cauchy problem. We have ten Einstein equations so it seems that the problem is solved. The truth is more complicated. If we remember the second contracted Bianchi identities:

$$\nabla_\nu G^{\mu\nu} = 0, \tag{1.72}$$

they can be written as:

$$\partial_t G^{\mu t} = -\partial_i G^{\mu i} - \Gamma^\mu_{\ \nu\lambda} G^{\nu\lambda} - \Gamma^\nu_{\ \nu\lambda} G^{\mu\lambda}, \tag{1.73}$$

where Latin indices refers to space coordinates $i = 1..3$, the coordinates of the hypersurfaces Σ.

Looking carefully at the right-hand side of the previous equation, we can see that there are no third order time derivatives which implies that $G^{\mu t}$ cannot contain time derivatives of second order. Then, it is clear that the evolution equations need to come from the following components of the EFEs:

$$G^{ij} = 8\pi G T^{ij}. \tag{1.74}$$

In addition, if we take into account that we always have the choice to introduce coordinate transformations on the hypersurfaces Σ without changing its geometry and we also have the freedom to choose the initial hypersurface we end up with having four free quantities that correspond with the two dynamical modes of the gravitational field, the two polarisation states of a gravitational wave.

One important problem in the thesis is going to be the evolution of scalar fields in spherical geometry. In this case, the additional symmetries reduce the degrees of freedom in such a way that the geometry of the spacetime does no have free propagating modes. This implies that the dynamical modes in this scenario come from the scalar field and once it is set in an spacelike hypersurface, the geometry is fixed.

The foliation in Fig. 1.2 is consistent with any temporal coordinate t and with non intersecting spacelike hypersurfaces but, of course, we have a lot of freedom to choose it. We define the unit normal vector to the hypersurfaces of constant t as:

$$n_\mu = -\alpha \nabla_\mu t, \tag{1.75}$$

with:

$$g^{\mu\nu} n_\mu n_\nu = -1, \tag{1.76}$$

and where α is the *lapse* function:

$$\alpha = \frac{1}{\sqrt{-g^{\mu\nu}\nabla_\mu t \nabla_\nu t}} \tag{1.77}$$

that controls how the time elapses between hypersurfaces. We also define the *shift* vector:

$$\beta^\mu = \delta^\mu_t - \alpha n^\mu, \tag{1.78}$$

that is tangent to only in the spacelike hypersurfaces ($\beta^t = 0$) and defines how we relabel the points of our space through the different hypersurfaces.

Now, we can introduce the form of the EFEs known as ADM equations [27] where the metric is expressed as:

$$g_{\mu\nu} = \begin{pmatrix} -\alpha^2 + \beta_k\beta^k & \beta_i \\ \beta_j & \gamma_{ij} \end{pmatrix}. \tag{1.79}$$

where the γ_{ij} is the 3-metric of the spacelike hypersurfaces. The constrain equations are the *Hamiltonian constrain*:

$$R + K^2 - K_{ij}K^{ij} = 16\pi\rho, \tag{1.80}$$

where K_{ij} is the extrinsic curvature of the spacelike hypersurfaces that describes how the spacelike hypersurfaces are embedded in the spacetime. We also have the *momentum constrain*:

$$\nabla_j \left(K^{ij} - \gamma^{ij}K\right) = 8\pi S^i. \tag{1.81}$$

The evolution equations are then:

$$\partial_t \gamma_{ij} = -2\alpha K_{ij} + \nabla_i\beta_j + \nabla_j\beta_i, \tag{1.82}$$

for the space metric and:

$$\begin{aligned} \partial_t K_{ij} =& \alpha\left[R_{ij} + KK_{ij} - 2K_{ik}K^k_j - 8\pi\left(S_{ij} - \frac{1}{2}\gamma_{ij}(S-\rho)\right)\right] \\ &- \nabla_i\nabla_j\alpha + \beta^k\partial_k K_{ij} + K_{ik}\partial_j\beta^k + K_{kj}\partial_i\beta^k, \end{aligned} \tag{1.83}$$

for the extrinsic curvature, where ρ, S^i, S_{ij} and S are the matter source terms defined as:

$$\begin{aligned} \rho &= n_\mu n_\nu T^{\mu\nu} \\ S^i &= -\gamma^{ij}n^\mu T_{\mu j} \\ S_{ij} &= \gamma_{i\mu}\gamma_{j\nu}T^{\mu\nu} \\ S &= \gamma^{ij}S_{ij}. \end{aligned} \tag{1.84}$$

The correct choice of the *lapse* and *shift* functions is a key issue in the numerical evolution of the Einstein equations. Although this is a great advance, the history of numerical relativity shows that the ADM equations are not enough for produce stable evolutions in 3+1 dimensions for configurations without symmetry. Modifications of it have been proven more successful. Introducing the generalised harmonic family of gauges, Frans Pretorius [24] was able to evolve for the fist time a binary black hole (BBH) system and to extract the gravitational-wave signal emitted. Before that, the BSSN formulation [28, 29] was shown much more stable than the ADM equations, although the BBH evolution with gravitational wave extraction had to wait until a better family of gauges was proposed [30, 31]. This section just give a glimpse of the problems of evolving numerically Einstein's Field Equations but it does not address all the issues that it exhibits.

1.2.2 Characteristic Initial Value Problem

As it was seen in Sec. 1.1.4, the intrinsic freedom to choose the foliation of the spacetime not only means that we can deform our space and time coordinates to adapted to our problem. We can also use the path of light, the null geodesics, as our coordinates in the characteristic approach to numerical relativity. Of course, most of the mathematical developments presented in the previous section are not valid here and we need to look for new methods. In this section, we described some coordinate choices and uses in a general way focusing in its interest for the following chapters. For more details about this kind of evolution, the reader can look at Refs. [32, 33].

A characteristic foliation has always null hypersurfaces $u =$ const generated by a two-dimensional set of null rays x^A, and a coordinate λ parametrising the null rays. We have now two kind of variables, ones that can be determined on a hypersurface (f) and other ones that evolve from one hypersurface to another (Φ). Then, we have two type of equations, the ones defined on the hypersurface:

$$f_\lambda = L_f[f, \Phi] \tag{1.85}$$

and the evolution ones:

$$\Phi_{u\lambda} = L_\Phi[f, \Phi]. \tag{1.86}$$

Characteristic evolutions have proven to be very robust and stable. In fact, the first long term simulation of a black hole was performed using this formulation [34]. A general feature of this formulation is that the initial data is not subject to elliptic constrains. This makes the imposition of initial conditions very flexible but more difficult to discriminate realistic ones. It also has the property that no second-order u-time derivatives are present and therefore we reduce the integration problem to half of variables.

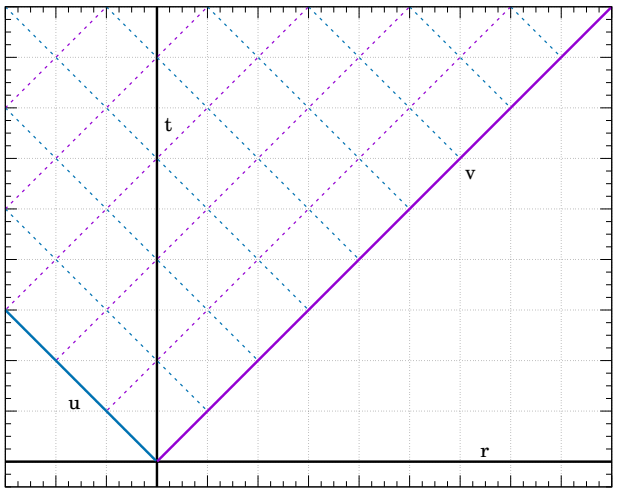

Figure 1.3: Double Null Characteristic Grid. Foliation in (u, v) coordinates in top of a Cauchy grid (r, t). The angular coordinates are hidden so every point in the grid represents a two-dimensional sphere. The equivalence between the two coordinate systems are shown according with a vacuum spacetime where $u = t - r$ and $v = t + r$. In a general case, the null directions are curved in the (r, t) plane.

One important application of the characteristic evolution exploits the fact that gravitational waves are better defined in null coordinates [32]. This is an important motivation for the use of this formulation. Even so, as we commented in the previous section, one of the most important problems in Numerical Relativity, the evolution and merge of binary black holes, was first done, and nowadays continues be treated that way, using the Cauchy formulations. This is because, although all of the advantages of the characteristic formulation, its main drawback is that the formation of caustics in the light rays generating the null hypersurfaces prevents to have a good evolution. For this reason, an alternative approach uses the characteristic evolution to extend data generated a Cauchy evolution [35].

Another feature to be notice is the fact that null foliations adapt very well to the formation of horizons. As a consequence the characteristic scheme has been used in the case of gravitational collapse since the initial formulation of Christodoulou [36] and later used for the numerical implementation by Goldwirth and Piran [37] and Garfinkle [38]. In this thesis, we incorporate this formulation adapted to the gravitational collapse of scalar fields in Anti-de Sitter spacetime, see Chapter 2.

The usual way of doing it is to write the metric of the spacetime in a form where the initial conditions are set on a null hypersurface $u = \text{const}$. We are going to illustrate this with the case in spherical symmetry. The coordinate used to label can

be chosen to be a spacelike coordinate r in what case we can write the metric as:

$$ds^2 = -g_{uu}(u,r)du^2 - g_{ur}(u,r)dudr + r^2 d\Omega^2, \tag{1.87}$$

or it can also be parametrised using a second null coordinate v in which case the metric is expressed as:

$$ds^2 = -g_{uv}(u,v)dudv + r(u,v)^2 d\Omega^2, \tag{1.88}$$

that is represented in Fig. 1.3 for the vacuum case. There, it is illustrated the double null grid in top of Cauchy grid (r,t) in which each point represents a two-dimensional sphere.

1.2.3 Well-posedness and Hyperbolicity

The intrinsic coordinate freedom presented in the EFEs implies that the same physical phenomena can be written in very different forms as we have seen in the previous pages. Of course all the ways do not have the same mathematical properties when we perform numerical evolutions. Here, we present the concepts of well-posedness and hyperbolicity [39, 40, 41] that help us to analyse systems of partial differential equations (PDEs) that admit the following form:

$$\partial_t \mathbf{W} = H\mathbf{W}, \tag{1.89}$$

where H is a general operator that can contain spatial derivative operators and $\mathbf{W}$ is the vector of our variables. In the previous two sections we have described the *initial value* problem in which we find the solution $\mathbf{W}(t,x)$ integrating from initial data at an initial time $\mathbf{W}(t=0,x)$. Notice that here we are talking about general PDEs and t is just a label. We are going to say that a system is well-posed [42] if we can define a norm $||\cdot||$ such that the norm of the solution can be bounded:

$$||\mathbf{W}(t,x_i)|| \leq \; ke^{\alpha t}\; ||\mathbf{W}(0,x_i)||, \tag{1.90}$$

where α and k are constants that needs to be the same for all the initial data. Well-posedness of a system is a necessary condition for having a stable evolution so it is going to be a condition to pursued when we analyse our problem. Although most problems we find in physics are well-posed it is not difficult to find very simple examples of PDEs that do not fulfil the previous condition. Some of these examples can be found in [42].

In order to study the stability of a system we introduce the concept of *hyperbolicity*. This concept is associated with systems of evolution equations that behave as generalisations of the wave equation. We start by writing our system of

PDEs in the following way:

$$\partial_t \mathbf{W} + \mathcal{A}^i \partial_i \mathbf{W} = \mathbf{S}(x_i, \mathbf{W}), \tag{1.91}$$

where $\mathcal{A}^i$ are a set of matrices, or a single matrix in the case of one space coordinate. Notice that way of writing the equations does not restrict ourselves to first-order problems because it can be done with any system of partial differential equations can be cast in this form by increasing the number of variables $\mathbf{W}$.

We can construct the principal symbol of the system of equations as:

$$\mathcal{P}(n_i) = \mathcal{M}^i n_i, \tag{1.92}$$

where n_i is a unit vector. The system is said to be *strongly hyperbolic* if the eigenvalues of this operator are real and we have a complete set of eigenvectors for all n_i. If the $\mathcal{M}^i$ are all symmetric, the system it is said to be *symmetric hyperbolic* and it is obviously *strongly hyperbolic*. On the other hand, if all the eigenvalues are real but we do not have a complete set of eigenvectors the system said to be *weakly hyperbolic*.

If the system is *strongly hyperbolic*, we can construct an invertible matrix $\mathcal{K}$ with the eigenvectors as columns, so that the principal symbol can be diagonalise as:

$$\mathcal{D}_\mathcal{P} = \mathcal{K}^{-1} \mathcal{P} \mathcal{K}. \tag{1.93}$$

Then we can write a new set of variables Y as:

$$\mathbf{Y} = \mathcal{K}^{-1} \mathbf{W}, \tag{1.94}$$

known as *characteristic variables*. The reason we care about this is because using it we can transform the the system described in Eq. (1.91) and in the case of one space dimension x into:

$$\partial_t \mathbf{Y} + \mathcal{D}_\mathcal{A} \partial_x \mathbf{Y} = \mathbf{S}(x, \mathbf{Y}). \tag{1.95}$$

This is important to analyse the stability of our evolution problem but it is also fundamental in the case of multidomain methods. In the boundaries of the domains in a multidomain scheme is very important to communicate our variables using the characteristic ones because we now exactly how the propagate, this is given by the eigenvalues of the previous problem or, equivalently, by the values contained in the diagonal of $\mathcal{D}_\mathcal{A}$.

1.3 Pseudo-Spectral Collocations Methods

In the previous sections, we have discussed the formulation of the EFEs and the proper manner that we need to set up the coordinates. But EFEs are written as differential equations, so the last step is to transform the smooth and continuous to a discrete and algebraic form an algorithm that computers can understand. This is known as **Numerical Methods**.

The simplest and most widely used, at least historically, are the ones called finite differences (FDs). First, we transform our continuous and differentiable spacetime into individual discrete points. Then, we replace the differential operators by algebraic expressions. For instance, for a smooth function and a uniform grid of spacing Δx we can write:

$$\left.\frac{df(x)}{dx}\right|_{x_0} = \frac{f(x_0+\Delta x) - f(x_0-\Delta x)}{2\Delta x} + \mathcal{O}\left(\Delta x^2\right). \tag{1.96}$$

This produces a discretisation error determined by the spacing Δx whose proper form can be derived using a Taylor series. In general the error scales with the spacing as a power, i.e. Δx^n where the power is determined by particular FD expressions that we choose. Using this type of expression we transform our differential equations into algebraic equations in all the points of our grid. The resulting discretised equations are coupled between them and the coupling degree is determined by the *stencil*, the number of points we use to estimate our operations. Once we have replace all our differential operators by algebraic ones, we have our system of equations that we can solve by linear algebra methods. Discretisation of this kind can be found in important works like Refs. [43, 24] being currently the fundamental ingredient on numerous numerical relativity codes.

Although it is deeply used in another fields and maybe is the most important method to discretise in engineering, the use of the finite elements methods (FEM) is very limited in numerical relativity and we can only find a few examples like Refs. [44, 45]. In these methods, we divide our computational domain in disjoint subdomains, the *elements*. In each of the elements, we approximate our solutions by a simple function. Then, we formulate the PDEs in its weak formulation, transforming the differential form into an integral that involves the boundary conditions and in this form we can define a residual function that it is minimised using variational methods.

In this thesis, the most widely used methods are Pseudo-Spectral methods (PSC) and in this section we introduce them showing their advantages, in particular their unbeatable order of convergence. Their properties make them a very good option to discretise EFEs and nowadays are deeply used in a lot of different problems.

1.3.1 Basics of PSC Method

We start from a very general point of view. The method of mean weighted residuals (MWR) is a set of techniques[2] to discretise the solutions of differential equations using a basis of functions to approximate the solution.

We can write the partial differential equations (PDE) in the following form:

$$L[u] = 0, \tag{1.97}$$

where L is a differential operator and u is its solution. This set of PDEs is expressed as an integral over the computational domain $\mathcal{D}$:

$$\int_{\mathcal{D}} L[u]\ \Psi_j dx = 0, \tag{1.98}$$

where Ψ_j are a set of test functions that depend of the specific of the method. Any of the solutions functions u can be represented in terms of a series of functions like:

$$u(x) = \sum_{k=0}^{\infty} \boldsymbol{a}_k\, \phi_k(x) \tag{1.99}$$

where ϕ_k are the trial or basis functions and a_k the coefficient of this expansion. This expansion is exact as we are accounting the infinite terms of it. As we are going to see, in the numerical computations we neglect terms above some k, generating the discretization error that decreases as we increase the number of modes introduced in the approximation. In the previous expression we have assumed that the differential equations to be one-dimensional. In the case of more than one dimensions, one set of basis functions are needed for each dimension. If we discretise all the coordinates but one, the time t, following the method of lines [46], the expansion coefficients will depend on this undiscretised coordinate.

One type of MRW are the Pseudo-Spectral Collocation methods (PSC) (see, e.g. [47, 48, 49]). Here, the test functions are just Dirac distributions:

$$\Psi_j = \delta\left(x - x_j\right), \tag{1.100}$$

associated with the grid points x_j. The imposition of this functions in the equation 1.98 set the condition that the differential equation needs to be fulfilled exactly in the collocation points x_j.

The most efficient choice for the the test functions in Eq. (1.99) depends on the exact geometry of our problem. For example, Fourier polynomials are very

[2]The method of MWR can be seen as a framework where the choice of basis and test functions lead us to PSC methods, FEM or others.

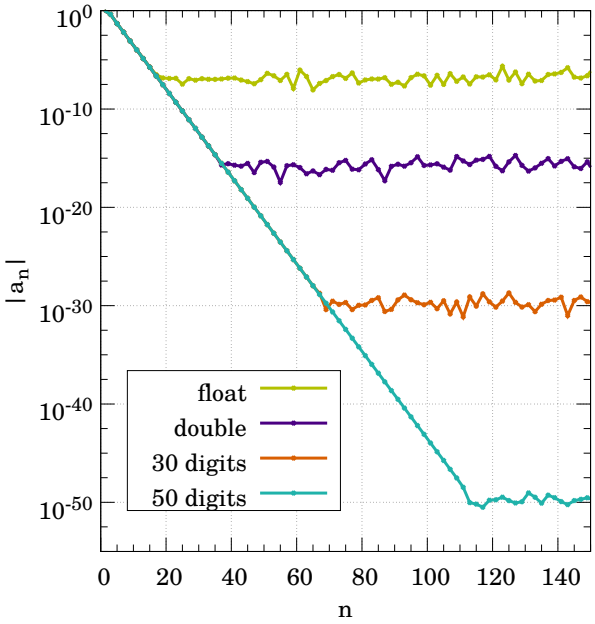

Figure 1.4: Representation of the Spectral Coefficients of a Test Function. In the general case order the modes decay exponentially until the reach of the round-off error that limits the minimum error that we can obtain with this data type. With the use of arbitrary precision, more number of digits, we can control this error.

precise with systems with periodic boundary conditions and spherical harmonics are specially suitable where we are dealing with spherical coordinates. In the general case the best solution are Chebyshev's polynomials,

$$T_n(X) = \cos\left(n \cos^{-1}(X)\right) \ , \tag{1.101}$$

that are defined in $X \in [-1, 1]$. From the Cauchy interpolation error theorem and the Chebyshev minimal amplitude theorem [48] can be shown that the optimal interpolation points are the roots of the Chebyshev polynomial of order $N + 1$. One of the possibilities that fulfils this condition is to take the *Lobatto-Chebyshev* grid that are the roots of:

$$(1 - X^2)\, T'_N(X) = 0, \tag{1.102}$$

that are:

$$X_i = -\cos\left(\frac{\pi\, i}{N}\right) \qquad (i = 0, 1, \ldots, N)\,. \tag{1.103}$$

Assuming the use of Chebyshev polynomials as basis in one direction X, the coefficients depends in the undiscretised coordinate t, our standard spectral

representation is:

$$u_N(t, X) = \sum_{n=0}^{N} \boldsymbol{a}_n(t)\, T_n(X)\,, \tag{1.104}$$

where the $\boldsymbol{a}_n$ is a (t-dependent) vector that contains the spectral coefficients of the expansion of our variables. In this representation, the order of magnitude of the spectral coefficients decay exponentially with the degree of the polynomial:

$$|a_n| \sim e^{-\alpha n}, \tag{1.105}$$

where α is an arbitrary parameter. This behaviour can be seen in Fig. 1.4, so does the discretization error provoked for taking a finite number of them.

In addition, in the case of the PSC method we also have a expansion in the collocation points, which looks as follows:

$$u_N(t, X) = \sum_{i=0}^{N} \boldsymbol{u}_i(t)\, \mathcal{C}_i(X)\,, \tag{1.106}$$

where $u_i(t)$ are the values of our variables in the collocation points and $\mathcal{C}_i(X)$ are the *cardinal* functions [48] associated with our choice of basis functions and set of collocation points. In our case the cardinal functions can be expressed as

$$\mathcal{C}_i(X) = \frac{(1-X^2)T'_N(X)}{(1-X_i^2)(X-X_i)T''_N(X_i)}\,. \tag{1.107}$$

Both the spectral modes and representation in the collocation points are related via a matrix transformation and, in this sense, the computations required increase quadratically with the number of collocation points as $\sim N^2$. Nevertheless, the use of trigonometric representation of the Chebyshev polynomials and the Lobatto-Chebyshev grid points allow to express the transformation as the Discrete Cosine Transform (DCT). This is very useful because this transformation can be computed as a $2N$ Fast-Fourier Transform (FFT) algorithm. With this, we can decrease the number of computations and the number of operations scale as $\sim N \ln N$ with the number of collocation points [47, 48].

As the Chebyshev polynomials are defined in the range $X = [-1, +1]$, the simplest scenario is to define our computational domain in this same range. Of course, this is not always possible, nor desirable in the general case. The solution is to introduce a mapping between the coordinate X and another *physical* coordinate x defined in an arbitrary range $\Omega = [x_L, x_R]$. The simplest mapping is of course a linear one:

$$X \longrightarrow x(X) = \frac{x_R - x_L}{2}\, X + \frac{x_L + x_R}{2}\,, \tag{1.108}$$

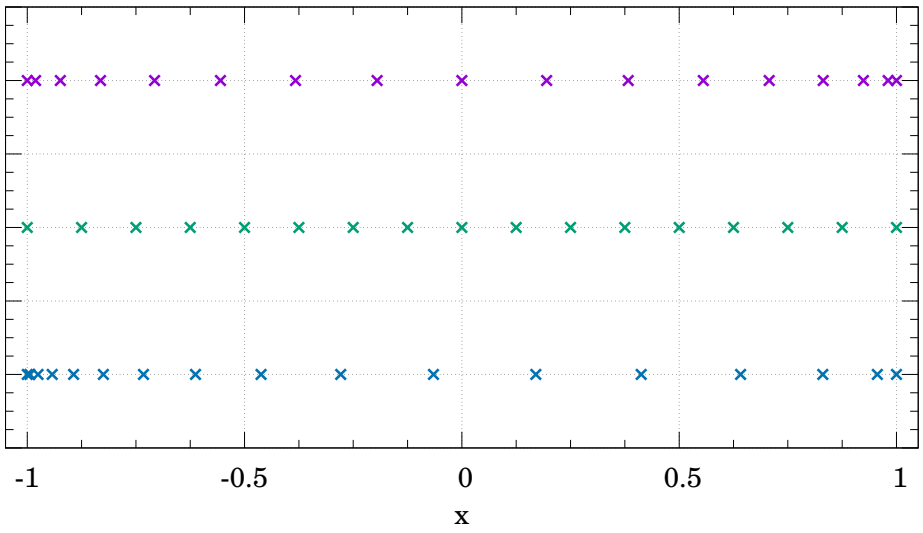

Figure 1.5: Mappings for the Spectral Grid. The upper (purple) points show the distribution of points in an usual Lobatto-Chebyshev grid, Eqs. (1.103) and (1.108). The middle (green) ones represent a uniform mapping as defined in Eq. (1.109) with $\alpha = 1$. In the bottom (blue), the distributions of points is the one of Eq. (1.110) with $\alpha = 1$.

where the distribution of the collocation points x are the same as the ones of X in a different range.

Creating a non-trivial map between a general coordinates x and the spectral ones X is not only motivated by the necessity of changing the computational domain. The collocation points X are distributed according to Eq. (1.103) that produces an accumulation of the points near the boundaries. The mapping x(X) can be used to change this distribution adapting our grid to the functions we want to describe. Any reasonable function can be used as mapping, checking that is smooth and have a non-vanishing derivative in the coordinate range considered [50]. We give here two examples of the several that can be used. To mimic a uniform grid, we can consider the mapping:

$$X \longrightarrow x(X) = \gamma + \beta \, \frac{\arcsin(\alpha \, X)}{\arcsin(\alpha)}, \tag{1.109}$$

where the uniformity of the points can be controlled by the parameter α. Setting it to one, make the grid exactly uniform but singular. This can be avoid taking $\alpha = 1 - \epsilon$ with ϵ very small. That reproduces an almost uniform grid without any singularity. Setting this parameter to zero, we recover the Lobatto-Chebyshev grid. The range of the coordinates of x can be easily controlled with β and γ. Now, we present a mapping that accumulate points in only one of the two boundaries with a simple

exponential function:

$$X \longrightarrow x(X) = \gamma + \beta\, e^{\alpha(1+X)}, \tag{1.110}$$

where, again, β and γ control the range and α set how strong is the accumulation. The three mappings here defined can be found in Fig. 1.5

The change between the collocation and spectral representations is a key issue in the PSC methods. In the case of derivatives, the computation in the physical representation can be perform as a matrix multiplication that use all the points of the domain. In the spectral representation this is much simpler involving just linear operations between coefficients. So, we can transform from the physical to the spectral representation, compute derivatives there, and finally transform back to the physical representation as is presented in the following scheme

$$\partial_x : \{\boldsymbol{U}_i\} \overset{DCT}{\longrightarrow} \{\boldsymbol{a}_n\} \overset{\partial_x}{\longrightarrow} \{\boldsymbol{b}_n\} \overset{DCT}{\longrightarrow} \{(\partial_x \boldsymbol{U})_i\}\,, \tag{1.111}$$

where $\{\boldsymbol{b}_n\}$ are the spectral coefficients associated with the spatial derivative ∂_x, and their relation to the spectral coefficients of the variables, $\{\boldsymbol{a}_n\}$, is given by [47]:

$$\begin{aligned} b_N &= 0 \\ b_{N-1} &= 2N a_N\,, \\ b_n &= \frac{1}{c_n}\left[2(n+1)\,a_{n+1} + b_{n+2}\right] \qquad n = N-2\ldots 0 \end{aligned} \tag{1.112}$$

where the coefficient c_n is two for $n = 0$ and one otherwise. Including the use of the FFT as DCT, the total operation scales as $N\log(N)$ as we see that the derivative in the spectral representation is linear giving a much better performance for a large number of N.

A considerable number of linear differential equations can be rewritten as direct integrals as for example the simplest possible differential equation:

$$\frac{df(x)}{dx} = g(x), \tag{1.113}$$

is solved just by:

$$f(x) = f(x_0) + \int_{x_0}^{x} g(\tilde{x})d\tilde{x}. \tag{1.114}$$

In this sense we implement a generic integration scheme that we call integral from the left because we choose to impose the boundary condition at $x_0 = X_- = -1$:

$$I_L(X) = I(X_-) + \int_{X_-}^{X} dX'\, f(X'). \tag{1.115}$$

To compute we can follow a similar scheme than in the derivative case:

$$\int_{X_-}^{X} : \{\boldsymbol{U}_i\} \overset{DCT}{\longrightarrow} \{\boldsymbol{a}_n\} \overset{\int}{\longrightarrow} \{\boldsymbol{b}_n\} \overset{DCT}{\longrightarrow} \{(\int_{X_-}^{X} \boldsymbol{U})_i\}\,, \tag{1.116}$$

where $\{\boldsymbol{b}_n\}$ are the spectral coefficients associated with the integral $I_L(X)$, and their relation to the spectral coefficients of the function $f(X)$, $\{\boldsymbol{a}_n\}$, are given by

$$b_N^L = \frac{a_{N-1}}{2N}\,, \tag{1.117}$$

$$b_n^L = \frac{1}{2n}\left\{\bar{c}_{n-1}\, a_{n-1} - a_{n+1}\right\} \qquad n = [N-1, 1]\,, \tag{1.118}$$

$$b_0^L = I(X_-) - \sum_{n=1}^{N} b_n\,(-1)^n\ . \tag{1.119}$$

Imposing the boundary condition in the right boundary $x_0 = I(X_+) = +1$, the process is totally equivalent:

$$I_R(X) = I(X_+) + \int_X^{X_+} dX'\, g(X'), \tag{1.120}$$

where the expression for the spectral coefficients for the integral are:

$$b_N^R = -\frac{1}{2N} a_{N-1}, \tag{1.121}$$

$$b_n^R = -\frac{1}{2n}\left(c_{n-1}\, a_{n-1} - a_{n\partial 1}\right) \qquad n = [N-1, 1], \tag{1.122}$$

$$b_0^R = I(X_+) - \sum_{n=1}^{N} b_n^R. \tag{1.123}$$

1.3.2 Multidomain PSC Method

The identification of the computational domain with a Lobatto-Chebyshev grid is not very practical in general. Even with the use of the non-trivial mappings defined in the previous section. To provide more flexibility to we are going to use a multidomain scheme, where the computational domain, say $\Omega = [x_L, x_R]$, is divided in several in several disjoint domains:

$$\Omega = \bigcup_{a=0}^{D-1} \Omega_a\,, \quad \Omega_a = \left[x_{a,L}, x_{a,R}\right]\,, \tag{1.124}$$

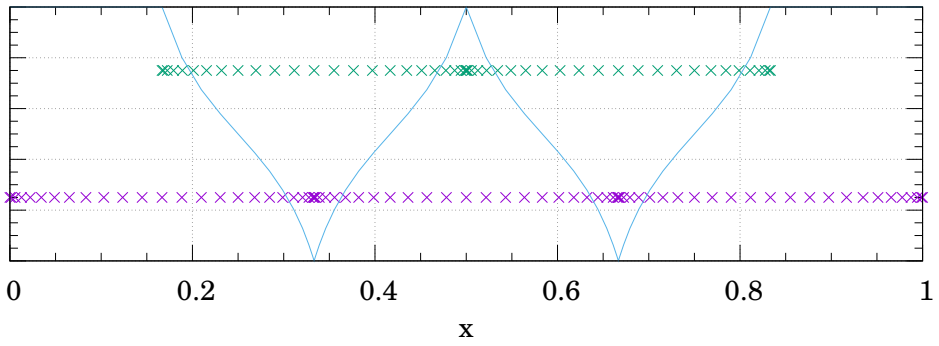

Figure 1.6: Structure of a Dual Grid. Diagram that shows the structure of a simple example of dual grid. The main grid(in purple) is composed of three domains and the dual grid (in green) is shift and have ones less domain. The blue line showed the $\pi(x)$ function of Eq. (1.129).

we are going to call this the multidomain scheme. Each of the domains is mapped into a spectral one $X_a = [-1, -1]$ using, by convenience [3] a linear mapping:

$$x \longrightarrow X_a(x) = \frac{2x - x_{a,L} - x_{a,R}}{x_{a,R} - x_{a,L}} \,. \tag{1.125}$$

and the inverse one is:

$$X_a \longrightarrow x(X_a) = \frac{x_{a,R} - x_{a,L}}{2} X_a + \frac{x_{a,L} + x_{a,R}}{2} \,. \tag{1.126}$$

and the Jacobian of the transformation is given by:

$$\frac{dx}{dX_a} = \frac{x_{a,R} - x_{a,L}}{2}, \tag{1.127}$$

where of course it is going to be different for each domain if they do not have the same coordinate length.

As we are going to see in Sec. 4.3, sometimes the computation of the derivative in the Lobatto-Chebyshev grid produces an accumulation of error in the points near the boundaries respect to the interior ones. In order to increase the precision we can use a dual grid scheme as it can be seen in Fig. 1.6. Here we superpose a second grid with the domains centred in the middle points of the original grid domains. When we compute the derivative in this dual grid, the points of lowest error coincide with the place where the error is maximum in the original domains. Once we have the

[3] We suppose here the simplest scenario but the domains can be map in a more general manner and also the mapping can be different in each of them.

derivatives in both grids, we can compute the ultimate derivative as a weighted sum of the original and the dual one as:

$$f'(x) = \pi(x) f'_{main}(x) + (1 - \pi(x)) f'_{dual}(x) \tag{1.128}$$

where $\pi(x)$ is the partition function that takes values between zero and one, being zero in the boundaries of the original domains and one in the boundaries of the dual grid and that needs to be smooth between the boundary and the centre of the domain. One example of a partition function is:

$$\pi(x) = \frac{(x - x_L) \cdot (x - x_R)}{(x - x_L) \cdot (x - x_R) + (x - \bar{x}_L) \cdot (x - \bar{x}_R)}, \tag{1.129}$$

Another advantages of the use of the multidomain scheme is the possible parallelism that can be emerge from the independence of the different domains as we are going to see in Sec. 4.3.3. This is obvious in the case of the derivatives where the all the domains are completely independent but it also can be true in the integration routines. Although the integral expression:

$$I_L(x) = I(x_{0,L}) + \int_{x_{0,L}}^{x} d\tilde{x}\, f(\tilde{x}), \tag{1.130}$$

seems sequential because values of high x depend in the previous integrals, the full integral can be computed in each domain separately

$$I_a(x) = \int_{x_{a,L}}^{x} d\tilde{x}\, f(\tilde{x}), \tag{1.131}$$

and then the full integral can be computed as:

$$I_L(x) = O_a + I_a(x), \tag{1.132}$$

where O_a is a value different in each domain:

$$O_a = I(x_{0,L}) + \sum_{i=0}^{a-1} I(x_{i,N}). \tag{1.133}$$

Both Eqs. 1.131 and 1.132 can be computed full independently in each domain and the only sequential part is now 1.133. This computation represents an insignificant part of the total computation and therefore should have very little effect in the parallelism of the computation.

The main advantage of the use of multidomain in the PSC methods is the flexibility that gives when we set our scheme. In a first approach, the domains can

be distributed concentrating them in the region where we need more accuracy. This is enough if we have the knowledge that the interesting physics is always happening in the same region. If we do not know in advance or if the region of interest moves during the simulation, the only way of avoid the necessity of increasing the resolution in the whole computational domain is to use adapting mesh refinement (AMR) techniques. In PSC methods this can be done by changing the location an distribution of the domains according with the demands of the simulation at each time. Not only that, the convergence of the spectral interpolation, make the regriding between the old and the new grids very efficient and accurate introducing almost no error during the operation. The use of AMR is going to be crucial in Chapter 2 where it is described one particular case of application.

Bibliography

[1] Isaac Newton. *Philosophiae naturalis principia mathematica*. J. Societatis Regiae ac Typis J. Streater, 1687.

[2] Isaac Newton. *Four letters to doctor Bentley containing some arguments in proof of a deity (in reply to inquiries made by him before publishing the last two lectures of A confutation of atheism).* 1756.

[3] Henri Poincaré. The New Mechanics. In *The foundations of science (Science and Method)*, page 486. New York: Science Press, 1913.

[4] Albert Einstein. Über das Relativitätsprinzip und die aus demselben gezogenen Folgerungen. (German) [On the Relativity Principle and the conclusions drawn from it]. *Jahrbuch der Radioaktivität und Elektronik*, 4:411–462, 1907.

[5] Albert Einstein. Grundgedanken der allgemeinen Relativitätstheorie und Anwendung dieser Theorie in Astronomie. (German) [Basic idea of the General Theory of Relativity and application of this theory in astronomy]. pages 315–315, 1915.

[6] Sean M. Carroll. *Spacetime and geometry: An introduction to general relativity*. 2004.

[7] Eric Poisson. *A Relativist's Toolkit. The Mathematics of Black-Hole Mechanics*. Cambridge University Press, Cambridge, 2004.

[8] Thomas W. Baumgarte and Stuart. L Shapiro. *Numerical Relativity: Solving Einstein's Equations on the Computer*. Cambridge University Press, Cambridge, 2010.

[9] Slava G. Turyshev. Experimental Tests of General Relativity. *Ann. Rev. Nucl. Part. Sci.*, 58:207–248, 2008.

[10] Clifford M. Will. The Confrontation between General Relativity and Experiment. *Living Reviews in Relativity*, 17(1):4, 2014.

[11] Robert M. Wald. *General Relativity*. The University of Chicago Press, Chicago, 1984.

[12] Stephen W. Hawking and George F. R. Ellis. *The Large scale structure of space-time*. Cambridge University Press, Cambridge, 1973.

[13] Juan Maldacena. The Large N limit of superconformal field theories and supergravity. *Int. J. Theor. Phys.*, 38:1113–1133, 1997.

[14] Edward Witten. Anti-de Sitter space and holography. *Adv. Theor. Math. Phys.*, 2:253–291, 1998.

[15] Lisa Randall and Raman Sundrum. A Large mass hierarchy from a small extra dimension. *Phys. Rev. Lett.*, 83:3370–3373, 1999.

[16] George D. Birkhoff and Rudolf E. Langer. *Relativity and Modern Physics*. Harvard University Press, 1923.

[17] Roger Penrose. Gravitational collapse and space-time singularities. *Phys. Rev. Lett.*, 14:57–59, 1965.

[18] Hans Reissner. Über die Eigengravitation des elektrischen Feldes nach der Einsteinschen Theorie. *Annalen der Physik*, 355:106–120, 1916.

[19] Gunnar Nordström. On the Energy of the Gravitation field in Einstein's Theory. *Koninklijke Nederlandse Akademie van Wetenschappen Proceedings Series B Physical Sciences*, 20:1238–1245, 1918.

[20] Roy P. Kerr. Gravitational field of a spinning mass as an example of algebraically special metrics. *Phys. Rev. Lett.*, 11:237–238, 1963.

[21] Stephen W. Hawking. Black holes in general relativity. *Comm. Math. Phys.*, 25(2):152–166, 1972.

[22] Benjamin P. Abbott et al. Observation of Gravitational Waves from a Binary Black Hole Merger. *Phys. Rev. Lett.*, 116(6):061102, 2016.

[23] Steven Weinberg. *Gravitation and Cosmology: Principles and Applications of the General Theory of Relativity*. Wiley, New York, NY, 1972.

[24] Frans Pretorius. Evolution of binary black hole spacetimes. *Phys. Rev. Lett.*, 95:121101, 2005.

[25] Eric Gourgoulhon. 3+1 Formalism and Bases of Numerical Relativity. 2007. gr-qc/0703035.

[26] Miguel Zilhao. *New frontiers in Numerical Relativity*. PhD thesis, Aveiro U., 2012.

[27] Richard L. Arnowitt, Stanley Deser, and Charles W. Misner. The Dynamics of general relativity. *Gen. Rel. Grav.*, 40:1997–2027, 2008.

[28] Masaru Shibata and Takashi Nakamura. Evolution of three-dimensional gravitational waves: Harmonic slicing case. *Phys. Rev.*, D52:5428–5444, 1995.

[29] Thomas W. Baumgarte and Stuart. L Shapiro. On the Numerical integration of Einstein's field equations. *Phys. Rev. D*, D59:024007, 1998. gr-qc/9810065.

[30] Manuela Campanelli, C. O. Lousto, P. Marronetti, and Y. Zlochower. Accurate evolutions of orbiting black-hole binaries without excision. *Phys. Rev. Lett.*, 96:111101, 2006.

[31] John G. Baker, Joan Centrella, Dae-Il Choi, Michael Koppitz, and James van Meter. Gravitational wave extraction from an inspiraling configuration of merging black holes. *Phys. Rev. Lett.*, 96:111102, 2006.

[32] Jeffrey Winicour. Characteristic Evolution and Matching. 2012.

[33] Thomas Mädler and Jeffrey Winicour. Bondi-Sachs Formalism. *Scholarpedia*, 11:33528, 2016.

[34] Roberto Gomez, Luis Lehner, Robert L. Marsa, and Jeffrey Winicour. Moving black holes in 3-D. *Phys. Rev.*, D57:4778–4788, 1998.

[35] Casey J. Handmer, Béla Szilágyi, and Jeffrey Winicour. Spectral Cauchy Characteristic Extraction of strain, news and gravitational radiation flux. *Class. Quant. Grav.*, 33(22):225007, 2016.

[36] Demetrios Christodoulou. The Problem of a Selfgravitating Scalar Field. *Commun. Math. Phys.*, 105:337–361, 1986.

[37] Dalia S. Goldwirth and Tsvi Piran. Gravitational Collapse of Massless Scalar Field and Cosmic Censorship. *Phys. Rev.*, D36:3575, 1987.

[38] David Garfinkle. Choptuik scaling in null coordinates. *Phys. Rev.*, D51:5558–5561, 1995.

[39] Richard Courant and David Hilbert. *Methods of Mathematical Physics Volume II*. John Wiley and Sons, 1989.

[40] Fritz John. *Partial Differential Equations*. Springer Verlag New York Inc., New York, 1991.

[41] Bertil Gustafsson, Heinz-Otto Kreiss, and Joseph Oliger. *Time dependent problems*. John Wiley & Sons, New York, 1995.

[42] Miguel Alcubierre. *Introduction to 3+1 numerical relativity*. International series of monographs on physics. Oxford Univ. Press, Oxford, 2008.

[43] Matthew W. Choptuik. Universality and scaling in gravitational collapse of a massless scalar field. *Phys. Rev. Lett.*, 70:9–12, 1993.

[44] Carlos F. Sopuerta and Pablo Laguna. A Finite element computation of the gravitational radiation emitted by a point-like object orbiting a non-rotating black hole. *Phys. Rev.*, D73:044028, 2006.

[45] Carlos F. Sopuerta, Pengtao Sun, Pablo Laguna, and Jinchao Xu. A Toy model for testing finite element methods to simulate extreme-mass-ratio binary systems. *Class. Quant. Grav.*, 23(1):251–286, 2006.

[46] Sarmin, EN and Chudov, LA. On the stability of the numerical integration of systems of ordinary differential equations arising in the use of the straight line method. *USSR Computational Mathematics and Mathematical Physics*, 3(6):1537–1543, 1963.

[47] Claudio Canuto, M Yousuff Hussaini, Alfio Quarteroni, and Thomas A. Zang. *Spectral methods in Fluid Dynamics*. Springer-Verlag, 1988.

[48] John P. Boyd. *Chebyshev and Fourier Spectral Methods*. Dover, New York, 2nd edition, 2001.

[49] Bengt Fornberg. *A Practical Guide to Pseudospectral Methods*. Cambridge University Press, Cambridge, 1996.

[50] Alvin Bayliss and Eli Turkel. Mappings and accuracy for chebyshev pseudo-spectral approximations. *Journal of Computational Physics*, 101(2):349 – 359, 1992.

Chapter 2

Critical Collapse in Asymptotically Anti-de Sitter Spacetimes

> Mirrors should think longer before they reflect.
>
> Jean Cocteau

The discovery of critical phenomena in the general relativistic gravitational collapse by Matthew Choptuik [1] remains nowadays as one of the main triumphs of Numerical Relativity. Following the question on whether gravitational collapse can form black holes with arbitrarily small mass [2], Choptuik investigated the gravitational collapse of a massless scalar field in spherically symmetric asymptotically flat spacetimes at the threshold between BH formation and dispersion, with flat spacetime as the end state. It was found that such system exhibits critical phenomena with the critical solution being discretely self-similar.

With the growing interest in the holographic methods provided by the AdS/CFT correspondence [3, 4], the dynamics of critical collapse and the stability of AdS have been studied in detail in the last years. The situation in AdS is very different from the asymptotically flat case. For space dimension $d \geq 3$, it has been shown that massless spherically symmetric scalar fields exhibit an instability [5], known as the AdS *weakly turbulent instability*, consisting in the formation of an apparent horizon (AH) in the evolution of general families of initial configurations and, in principle, for any value of the initial energy. This can be understood in terms of the global AdS causal structure since lightlike signals can reach the AdS timelike boundary in a finite proper time. Then, an initial configuration with arbitrary small initial energy bounces repeatedly off the AdS boundary while the non-linearity of gravity transfers energy from long wavelength to short wavelength modes (and hence the

name *turbulent* in analogy to what happens in the case of fluid turbulence [6]), until the profile becomes sharp enough to form an AH.

This chapter begins with an introduction to critical collapse where we review the problem of the stability of Minkowski spacetime and see what are the properties of the critical collapse there. Afterwards, we explain the structure and the main features of global AdS. In the rest of the chapter we present new work on the critical collapse in AdS spacetimes following Refs. [7, 8]. We start by introducing the Einstein-Klein-Gordon (EKG) system of equations and, for the spherically symmetric case, we adapt them to a Cauchy type formulation and to a characteristic formulation. Then, we explain our numerical scheme, which includes an initial stage of Cauchy evolution and a transition to the characteristic one when the collapse is approaching. Finally, using this hybrid Cauchy-characteristic scheme, we present new numerical results on the dynamics of AH formation that are completely different from the case of asymptotically flat spacetimes.

2.1 Gravitational Critical Collapse

2.1.1 The Stability of Minkowski Spacetime

The concept of stability is one of the recurring topics in physics and in dynamical systems. In General Relativity plays a crucial role in the analysis of the dynamics of our spacetimes. In a simple manner, we can say that an spacetime is *dynamical stable* if a perturbation introduced in the spacetime remains bounded through time. Let us imagine a BH where we throw a small perturbation. If the system reacts using this perturbation to increase a bit its mass or maybe getting rid of it by emitting radiation, the final state is going to be very close to the initial spacetime. This is an example of a stable scenario. But we can also imagine the case where the small perturbation excites certail modes of the system developing an instability that "destroys" the original spacetime and converts it into a complete different system, for instance by the formation of horizon and / or singularities. This would mean that our spacetime is *unstable*. This behaviour is present in all fields of physics from atmospherics to plasmas or structure formation in astrophysics and, of course, it can also happen in GR. In this chapter we are going to distinguish two different cases. The case of linear stability in which the perturbation is *infinitesimal* and the non-linear case in which the perturbation can be very small but finite and then the non-linear terms of EFEs can not be neglected in order to study the evolution. The study of stability is crucial for several reasons. Even if a solution is stationary, we cannot expect to find it realised in the Universe if it is not stable. The Kerr solution can be the final state of gravitational collapse but if a small perturbation can disrupt it, any Kerr BH would disappear before we can observe it. This is not the case and due to the no-hair theorem [9] Kerr is expected to be the final state of gravitational collapse.

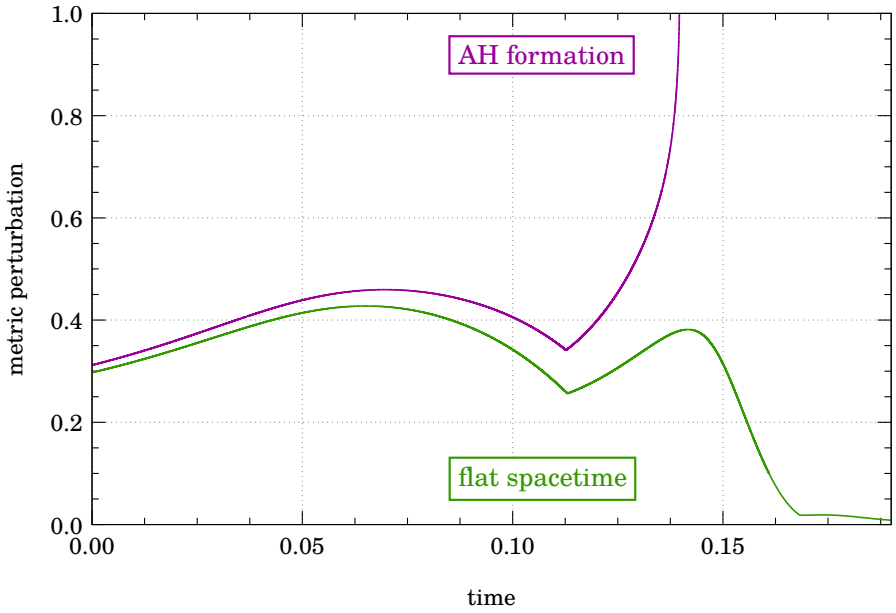

Figure 2.1: Possible End States for the Scalar Field Evolution. For an initial massless scalar field, there exists only two possible end states: Minkowski spacetime for small amplitudes and Black Hole formation for non-small ones. The plot shows the evolution of the metric perturbations for the two possible outcomes.

In the late eighties, Demetrius Christodoulou published a series of papers [2, 10, 11, 12, 13] where he constructed analytically a general solution for the collapse of small perturbations of a massless scalar field in spherical symmetry. In them, he showed that for general initial conditions, the scalar field converges near the origin and later, it disperses recovering Minkowski spacetime at future null infinity, $\mathcal{J}^+$. This result uses the restrictions of spherical symmetry and small enough amplitude of the scalar field. In any case, this was a step forward in the study of the stability of flat spacetime. The full nonlinear general proof of the stability can be found in the book that Christodoulou published with Sergiu Klainerman in 1994 [14].

As in all the previous works, we have been discussing small perturbations and the question to try to answer is about what happens for not so small perturbations. Do we still recover Minkowski spacetime? Do we find the formation of a BH? Can a naked singularity appear?

2.1.2 Choptuik's Work on Gravitational Collapse

The final and revolutionary answer to this question, in the case of massless scalar fields in spherical symmetry, was provided by Matthew Choptuik in 1992 [1],

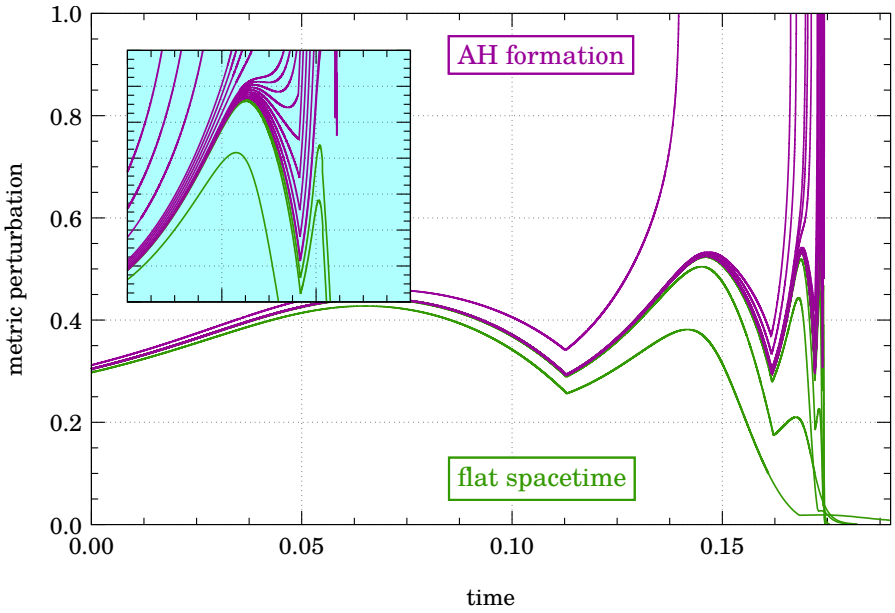

Figure 2.2: Study of the Threshold in the Scalar Field Evolution. Green lines show the evolution of configurations that end dispersing themselves while purple ones represents configurations that end up collapsing. The zoom in area represent a range in time of $3 \cdot 10^{-3}$ in the last stages before collapsing / dispersing.

although previous hints were presented by Choptuik himself [15] and by Goldwirth and Piran [16]. The use of scalar fields in this case is not only a good approach because it is the simplest. It is also because it ignores quantum effects that may create stable stationary states that do not collapse. Indeed, in the case of degenerate stars, quantum properties of matter establish a lower limit for the mass of an astrophysical BH [17]. With scalar fields there are only two possible final states: (i) The formation of a (Schwarzschild) BH. (ii) Dispersion of the scalar field leading to flat space as the final state of the evolution. In Fig. 2.1 we can see two evolutions that show this situation. The plot shows the evolution of a perturbation measured by the maximum of a particular metric function in a given time. This function is zero for a Minkowski spacetime and it is one when an apparent horizon is formed. When the perturbation is small the scalar field evolves until it disperses. In the case where the amplitude is big enough the scalar field collapses forming an AH when approaching the origin. In the works previously mentioned, different numerical schemes are used. A multigrid Cauchy formulation in Ref. [15] and a characteristic formulations like the one introduced by Christodoulou in Ref. [16].

This result anticipates the existence of a threshold between the two final states described before. The study of this separation region needs very high computational precision and that was achieved in Ref. [1] and later in Ref. [18] using the

characteristic formalism. We can study in detail what happens when we approach more and more this threshold as it is shown in Fig. 2.2. In that plot, we can see not only a clear threshold around a certain amplitude, that we call the *critical amplitude*, but also how in the proximity of it there appear some "oscillations" that become more and more compact over time. Notice the zoom-in plot inside Fig. 2.2 where the "oscillations" previously mentioned can be observed in a time range of $\Delta t = 3 \cdot 10^{-3}$ before the collapse takes place.

What these oscillations indicate is a self-similar structure that appears for any dimensionless quantity Z, that is:

$$Z(t, r) = Z(e^{\Delta} t, e^{\Delta} r), \tag{2.1}$$

where Δ is called the *echoing period*. When this type of symmetry is found, the critical solution is called discrete self-similar (DSS).

Apart from this, Choptuik studied the BH formed as the end state for the supercritical solutions, the ones above the critical amplitude. The mass of the BH formed was found to be given by the location of the AH formed:

$$M_{BH} = 2 r_{AH}. \tag{2.2}$$

Considering the amplitude p of the initial scalar field configuration and the critical amplitude p_c, a representation of what happens for $p \gtrsim p_c$ can be seen in the left plot of Fig. 2.3. The mass of the formed BH presents a scaling law given by:

$$M_{BH} \sim (p - p_c)^{\gamma}, \tag{2.3}$$

where the exponent γ of this power law can be determined by a direct linear fitting:

$$\log\left(M_{BH}\right) = \beta + \gamma \left(p - p_c\right), \tag{2.4}$$

where the importance of β and γ will be discussed later. As a connection with statistical mechanics, this kind of behaviour where the mass M_{BH} presents a continuous behaviour in the critical point is denominated critical behaviour of Type II.

When the solution is DSS, as in the case of massless scalar fields, a finer structure can be found [19, 20]:

$$\log\left(M_{BH}\right) = \gamma \log(p - p_c) + c + f(\log(p - p_c)), \tag{2.5}$$

where $f(x)$ is a periodic function with period $\Delta/2\gamma$. After analysing different families of initial conditions with different profiles, Choptuik conjectured that both the scaling exponent, $\gamma \approx 0.374$, and the echoing period, $\Delta \approx 3.44$, are universal. That is, they are the same for any family of initial conditions. On the other hand, β

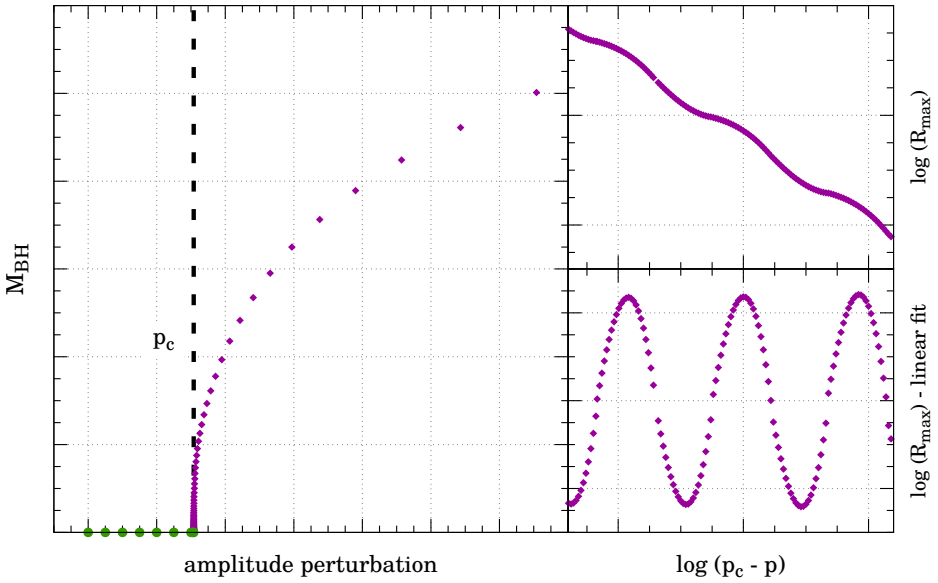

Figure 2.3: Scaling of the AH Mass of the Formed BHs. The left plot represents the mass of the BH as a function of the amplitude of the perturbation. On the right, the logarithmic scaling of the maximum of the scalar of curvature as in Eq. (2.6) (up) and subtracting the linear part (bottom).

and p_c depend on the family of initial configurations we propose.

The previous results have another important implication. We mentioned that one of the reasons for using scalar fields is to avoid quantum effects that create stable intermediate states. Those effects present in the physical gravitational collapse provoke that in stellar collapse, the minimum mass that a BH can have is a value between two and three solar masses (the Tolman–Oppenheimer–Volkoff limit [21, 22], the exact value of this limit depends on the equation of state of the type of matter considered). This is not the case here. As it can be seen in Eq. (2.4), it is possible to generate arbitrary small BHs from the collapse of massless scalar fields, and hence it is a real possibility to have BH in a range of masses smaller than the stellar ones.

Later on, it was shown that the same analysis can be done using the scalar of curvature at the origin [23]. The exact solution described by Eq. (2.1) exists only in the case where $p = p_c$ but this exact value is impossible to reach numerically. From Fig. 2.2 we can intuit that the approach to the critical solution can be done both from the subcritical solutions and from the supercritical solutions. Since in the case of subcritical configurations the final state is meaningless because we are always going to recover flat spacetime, we need to use some value before the dispersion. The quantity to track is going to be the scalar of curvature R at the origin. It can be

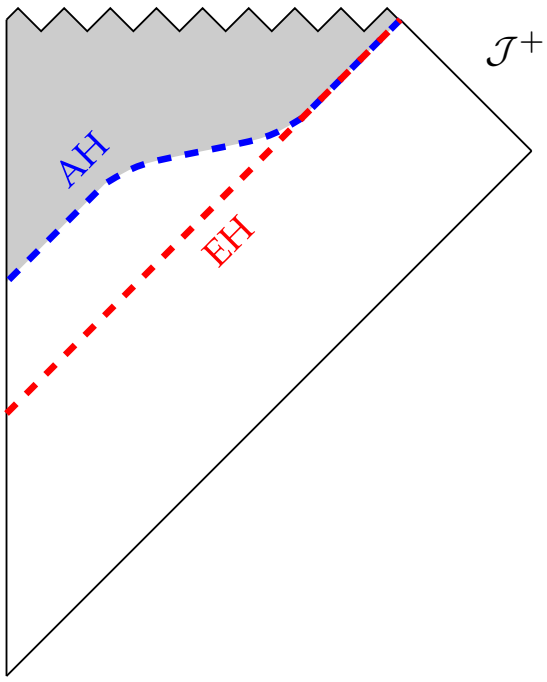

Figure 2.4: Difference between the AH Mass and the Final BH Mass. From now on, we call M_{AH} to the mass of the first AH formed in the evolution. Not to be confused with the asymptotic mass that coincide with the event horizon.

shown that the maximum of R during the evolution scales as:

$$\log R_{\max}|_{r=0} = (-2\gamma)\, \log(p_c - p) + b + f(\ln(p_c - p))\,, \tag{2.6}$$

where the exponent this time is 2γ and the period of f is $\Delta/2\gamma$. We show this scaling in Fig. 2.3. In the right upper plot, we can see the logarithm of the maximum of the scalar of curvature with respect to the logarithm of the difference between the parameter p of the initial configuration to the critical where the linear behaviour is used to estimate the critical exponent γ. In the right bottom plot, we subtract the linear fitting, we can see the periodic structure from where the echoing period can be estimated. We plot $R_{\max}$ and not M_{BH} for the sake of clarity. In the behavior of the scalar of curvature, the oscillatory structure is more prominent and hance easier to notice. If we would have plotted $\log(M_{BM})$ we would not have seen the oscillations without the subtraction of the linear fitting.

In the section we have used the term BH mass but this can mean different things. As Ref. [24] points out, when the first AH is formed, there is still energy from the scalar field going through the AH increasing in this way the mass of the BH until all the scalar field is disperse towards infinity or it is absorved by the AH. This is the moment when the AH and the event horizon (EH) coincide. This process can be seen in Fig. 2.4. What we have called M_{BH} until now is the mass of the first AH formed

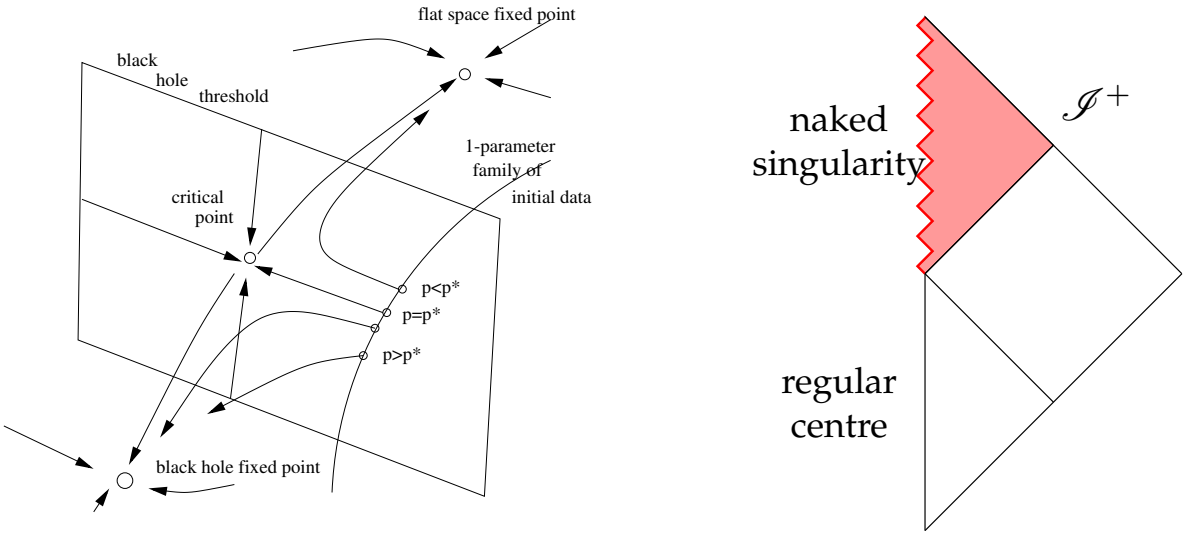

Figure 2.5:
Left Plot: Phase Space of the Critical Collapse. The evolution of a given initial configuration can end in one of the two fixed points (BH or flat space) depending only in the magnitude of the parameter that characterise the family of initial configurations. The threshold is the plane $p = p_c$ which contains an unstable attractor (the critical solution). Figure taken from [25].
Right Plot: Conformal Diagram of the Critical Solution. Diagram for all generic DSS continuations [26] of the scalar field critical solution where a timelike naked singularity appears. There are also continuations where a regular centre appears but it also contains one spacetime point with the naked singularity.

that is the quantity that presents the critical scaling found by Choptuik and that from now on we will call the AH mass, M_{AH}, to avoid confusion. The final mass, defined as the asymptotic limit at $\mathcal{J}^+$ does not present the critical scaling [25].

2.1.3 The Critical Solution

Although in the numerical work of Choptuik, the limit $p = p_c$ is not reachable, one can approach it to a level that indicates that for $p \approx p_c$ there exists a critical solution acting as an intermediate attractor that separates the two stable end states of the evolution of our system. This is illustrated in the phase space of the left plot of Fig. 2.5. The BH threshold separates the parameter region where we end up in the flat spacetime fixed point from the region that heads to the BH fixed point. Moreover, tuning our initial parameter to start as close as we can to the critical one, $p \approx p_c$, the evolution is attracted to the critical solution and shows the properties of it for a while before ending in one of the stable end points.

The critical solution shows a discrete homotheticity, or scale invariance, with

a logarithmic factor Δ, see Eq. (2.1). Few years after Choptuik's paper, Carsten Gundlach [27, 19, 26] used this symmetry to formulate an eigenvalue problem from which he constructed the critical solution. In the right plot of Fig. 2.5 we can see a spacetime continuation beyond the Cuachy horizon of the critical solution [26]. The red region represents an asymptotically flat region with a timelike naked singularity.

This is surprising in the sense that it means that we can tune our scalar field to $p = p_c$ and then generate a naked singularity starting from smooth initial data. This would imply a violation of the cosmic censorship hypothesis, which states that no observer at future null infinity should be in causal contact with any singularity. In reality, this case is nothing to worry about because, as we have seen, the critical solution only happens in the case of a "perfect" tuning and this will not happen in nature.

2.1.4 Generic Gravitational Critical Collapse

The discussion up to this point is about the case of a massless scalar field in spherical symmetry. We have focused on it because it was the first one to be analysed in depth and also because presents a lot of similarities with the AdS case although, of course, the change of the spacetime structure is going to modify the outcome of the evolution.

Since the nineties, critical phenomena has been found in a variety of different systems in gravitational collapse, finding a rich structure that only depends on the details of the physical system. In the Einstein-Yang-Mills case [28] a new phase with a gap in the BH mass, called Type I, appears along with the usual Type II phase. Similar to what happens also in the massive scalar field case [29, 30]. The case of higher dimensions have also been studied [31, 32]. The 2+1 case is not interesting in asymptotically flat spacetime because BHs cannot exist there, but it is interesting in AAdS spacetimes [33, 34]. In addition, AdS in 3+1 was studied in Ref. [35] and the main results so far are reviewed in the following section.

The study of gravitational collapse is in general difficult because of the numerical issues that arise in the moment of the collapse, specially for configurations near the critical point. For this reason, going beyond spherical symmetry is always a challenge. Nevertheless, there exist some examples, like the axisymmetry case [36], that prove that critical behaviour in gravitational collapse is not an artifact of spherical symmetry. A complete review of the different scenarios where critical gravitational collapse has been studied can be found in Ref. [25].

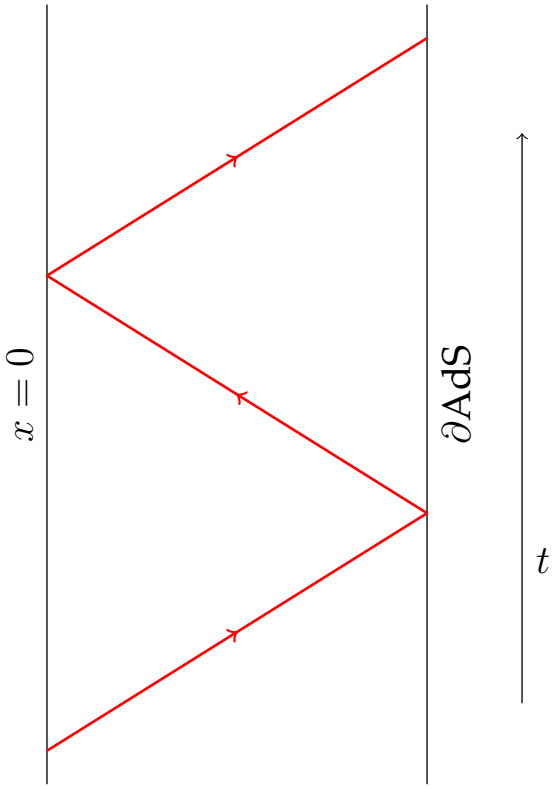

Figure 2.6: Penrose Diagram of AdS. The boundary of AdS is reachable by null geodesics (in red) in a finite time as measured at the origin.

2.2 Anti-de Sitter Spacetime

2.2.1 "The Infinite Box"

Anti-de Sitter spacetime is the maximally symmetric solution of the Einstein equations with negative cosmological constant [37]:

$$R_{\mu\nu} - \frac{1}{2} g_{\mu\nu} R + \Lambda g_{\mu\nu} = 0. \tag{2.7}$$

Indeed, as we saw in the previous chapter, in this case the Ricci tensor (and the Riemann tensor) are fully determined by the scalar of curvature and the EFEs reduce to:

$$R = 4\Lambda. \tag{2.8}$$

As we can see from this equation, we have a spacetime of constant negative curvature. The group of symmetries of this spacetime has ten parameters, which is the maximum number that it is possible in four dimensions, Ref. e.g. [37], and

hence it is maximally symmetric as it has been already mentioned, and so they are Minkowski and de Sitter spacetimes.

In spherical coordinates, the metric of AdS can be written as:

$$ds^2 = -\left(1 - \frac{\Lambda}{3}r^2\right) d\bar{t}^2 + \left(1 - \frac{\Lambda}{3}r^2\right)^{-1} dr^2 + r^2 d\Omega^2, \tag{2.9}$$

where r is a radial coordinate in the range $(0, \infty]$ and the temporal coordinate $\bar{t}$ is in $(-\infty, \infty)$. We can introduce the AdS length scale $\ell = \sqrt{-\Lambda/3}$, a compactified dimensionless spatial coordinate x and an dimensionless time t and then we can write the line element in the form:

$$ds^2 = \frac{\ell^2}{\cos^2(x)} \left(-dt^2 + dx^2 + \sin^2 x \, d\Omega^2\right). \tag{2.10}$$

In these coordinates we have mapped the boundary of AdS (from now on ∂AdS) from $r = \infty$ to $x = \pi/2$. Since the temporal coordinate t is not bounded, reducing one of the angular coordinates, we can see AdS as an infinite cylinder in three dimensions. In Fig. 2.6 we show a conformal diagram where we see that the boundary, ∂AdS, is a timelike hypersurface [38, 39]. However, for any point in the interior region, the bulk, the distance to the boundary is infinite:

$$l = \int_x^{\partial \text{AdS}} g_{xx} = \infty. \tag{2.11}$$

On the other hand, the radial null geodesics are just:

$$\frac{dx}{dt} = \pm 1, \tag{2.12}$$

and then a light ray can go to the boundary and come back. If we take an observer at the origin, he just need to wait a time $t = \pi$ for the light ray to come back. For this reason we can say that AdS is like an infinite box.

Both the coordinates of Eq. (2.9) and Eq. (2.10) represent the "whole" spacetime in what is usually known as *global AdS*. In most applications of the AdS/CFT correspondence, only a patch of the full spacetime is used correspondence but this will be explained in the next chapter.

One important question is how the cosmological constant affects the BH solutions, do they still exist? The answer is yes and one example can be seen in the conformal diagram of Schwarzschild-AdS (Fig. 2.7) where the spacetime looks very similar to the Schwarzschild spacetime. The only difference is, of course, the asymptotically AdS region (AAdS) outside the event horizon with the distinctive

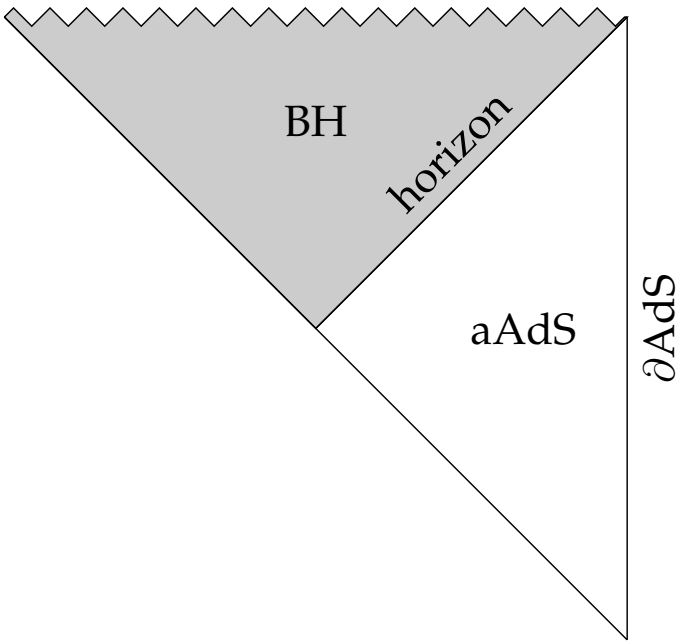

Figure 2.7: Penrose Diagram of Schwarzschild-AdS. The solution is similar to the Schwarzschild metric with the different of the conformal boundary of AdS.

AdS boundary. In spherical coordinates the line element can be written as:

$$ds^2 = -\left(1 - \frac{2GM}{r} + \frac{r^2}{\ell^2}\right) d\bar{t}^2 + \left(1 - \frac{2GM}{r} + \frac{r^2}{\ell^2}\right)^{-1} dr^2 + r^2 d\Omega^2, \tag{2.13}$$

where M is the BH mass.

The case of the BTZ black hole (Bañados, Teitelboim and Zanelli; see Ref. [40]) is also very interesting. It is a solution in 2+1 dimensions with negative cosmological constant that represents a BH with mass, angular momentum and electrical charge. The finding of such solution produced some surprise because in flat spacetime there are no BH solutions for lower dimensions than 3+1. The BTZ solution shares with the asymptotically flat Kerr solution some properties like the thermodynamics and the horizon structure but with less dimensions, what makes it easier to study. Due to that, the first studies in critical collapse at AAdS were done in 2+1 by Pretorius and Choptuik ([33]) where they studied the critical solutions and the causal structure of this spacetime. Another examples of the study of this gravitating collapse in 2+1 AAdS can be found in Refs [34, 41].

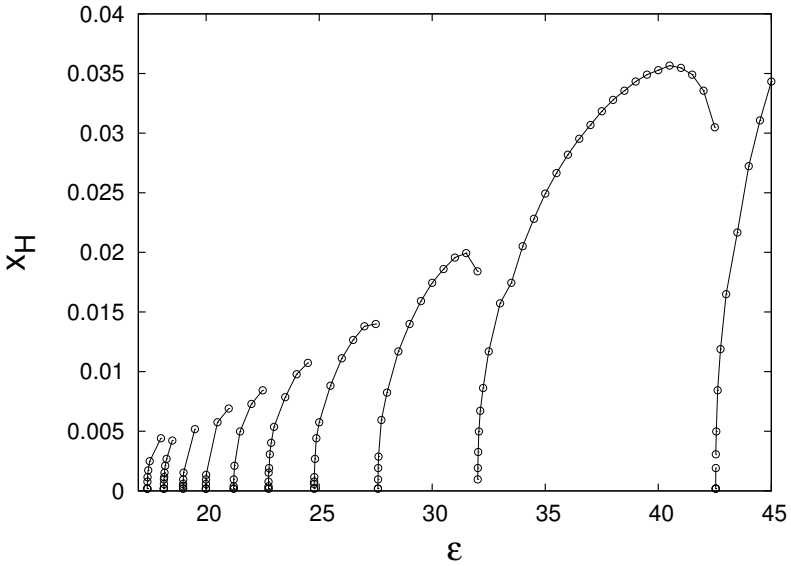

Figure 2.8: AH Radius in AdS. The rightmost branch is the equivalent to Choptuik's where the collapse happens without influence of the boundary. Each of the branches to the left of this one correspond with configurations that have bounce off in the boundary one more time for each branch and, up to the precision of the numerical computations, it seems that any configuration with arbitrary small amplitude will collapse. Original figure from [5].

2.2.2 The Turbulent Instability of Global AdS

A great revolution in our understanding of the asymptotically AdS spacetimes came in 2011 with the work of Bizoń and Rostworowski [5]. When the applications of AdS/CFT were creating more and more expectations they raised the question, is global AdS stable? This is of course very important if we want to develop tools to study asymptotically AdS spacetimes. They proposed the evolution of a massless scalar field in a Cauchy formulation similar to the one used by Choptuik [1] and also to the one presented in Eq. (2.10). Although the matter content is the same as in the case of cosmological constant, there is a big difference: the presence of a boundary that confines our scalar field as described in the previous section and also illustrated in Fig. 2.6. For low amplitudes the scalar field would disperse to infinity in an asymptotically flat spacetime but here in AAdS this dispersion is impossible. What it was shown in Ref. [5] is that there exist an energy transfer during the bounces of the AdS boundary from low to high frequency modes that triggers a *weakly turbulent instability* that provokes a collapse for "any" initial amplitude of the scalar field. The plot in Fig. 2.8 shows the position of the formed AH, x_{AH}, as a function of the initial amplitude of the scalar field, ϵ. The points on the right correspond to configurations collapsing directly without reaching the boundary. The next branch to the left represents configurations that have collapse after one bounce off the AdS

boundary and as we go to the left each of the branches collapses after one more bounce.

The situation that emerges is that we have an "infinite" series, up to the numerical precision B&R were able to achieve, of critical points $\{p_n\}$ with n being an integer number from zero to, in principle, infinite. It was also suggested that, within their numerical precision, the supercritical solutions follow the same scaling found by Choptuik [1] in flat spacetime with the same critical exponent $\gamma \approx 0.37$ and that across critical points there exists a gap between the mass of the AH formed coming from the supercritical configurations and from the subcritical ones. The exact behaviour in the threshold between branches is going to be the key subject of this chapter. A question that arises from the previous discussion is: is the boundary the only responsible of the *turbulent instability* or the presence of a cosmological constant also plays a role? One way of answering this question is to place an artificial boundary in an asymptotically flat spacetime like it is done in Refs. [42, 43, 44, 45, 46]. In that system, the same general behaviour of Fig. 2.8 is observed, although in the next sections we are going to discuss that some quantitative features of the subcritical configurations appears to be different [7, 8, 46].

There are still some open questions about this instability, in particular about how generic it is. Studies like those in Refs. [47, 48] show the existence of quasi-periodic solutions for widely spread initial configurations in which all the modes are initially populated and therefore the *turbulent cascade* of energy modes cannot happen. Although the existence of this kind of solutions is known, there is a debate about how large is the the size of the stable solutions in the space of possible initial configurations. There is some evidence obtained by combining non-linear perturbation methods and numerical simulations that these stable solutions can be somehow more general [49, 50] but this result has been put in question [51, 52] so that are still some discrepancies about the real importance of these stable solutions.

2.3 Formulation of the Field Equations

The field equations for a self-gravitating, real massless scalar field ϕ in an AAdS spacetime are the EKG equations for the metric $\mathrm{g}_{\mu\nu}$:

$$G_{\mu\nu} + \Lambda \mathrm{g}_{\mu\nu} = (d-1)\left(\phi_{;\mu}\phi_{;\nu} - \tfrac{1}{2}\mathrm{g}_{\mu\nu}\phi_{;\alpha}\phi^{;\alpha}\right) , \tag{2.14}$$

$$\mathrm{g}^{\mu\nu}\phi_{;\mu\nu} = 0 , \tag{2.15}$$

where $G_{\mu\nu}$ is the $(d+1)$-dimensional Einstein tensor and Λ is the (negative) cosmological constant.

We restrict our study to spherically symmetric configurations. This assumption simplifies the structure of the spacetime metric and the field equations. Spherically

symmetric spacetimes have a warped geometry, which means that their metric tensor can be written in the form:

$$ds^2 = \mathrm{g}_{AB}(x^C)dx^A dx^B + r^2(x^C)\gamma_{ab}dx^a dx^b, \tag{2.16}$$

with $A, B, C, ... = 0, 1$ and $a, b, c, ... = 2, ..., d$. The object g_{AB} is a Lorentzian metric, with associated two-dimensional manifold M^2, γ_{ab} is the metric on the $(d-1)$-sphere, with associated manifold S^{d-1}, and $r = r(x^A)$ is the radial area coordinate with depends only on the coordinates of M^2. The fact that $r^2(x^C)\gamma_{ab}$ is not a true metric on S^{d-1} is what prevents the spacetime manifold M^{d+1} to be a true product of the two manifolds M^2 and S^{d-1}. Instead, it is said that the spacetime manifold is the warped product of M^2 and S^{d-1} and this is sometimes denoted in the literature as $M^{d+1} = M^2 \times_r S^{d-1}$.

We can freely choose the coordinates in the Lorentzian manifold M^2. In this work we will consider two different choices according to the type of spacetime slicing that they induce:

- Timelike slicing: We will consider coordinates $(x^A) = (t, x)$ so that the spacetime is sliced in spacelike (with timelike normal 1-form) hypersurfaces $\{t = const.\}$. In addition, we take x to be a radial coordinate that compactifies the radial direction so that it is in the range $x \in [0, \pi/2]$, where $x = 0$ corresponds to the *centre* of the radial coordinate system and $x = \pi/2$ corresponds to the AdS boundary. Using these coordinates we can set up a Cauchy-type system of evolution equations with some constraints. Given the causal structure of AAdS spacetimes, the scalar field can propagate to reach the AdS boundary in a finite time. Previous works on this problem (see, e.g. [5, 53]) showed that we can expect the field to bounce off the AdS boundary a number of times and eventually collapse near the centre $x = 0$. It is for this reason that we use the compactified coordinate x in order to track the field up to the AdS boundary as many times as needed. The equations for this formulation are given in Sec. 2.3.1.

- Lightlike slicing: We will consider coordinates $(x^A) = (u, r)$ so that the spacetime is foliated by outgoing null hypersurfaces (composed by outgoing null rays) $\{u = const.\}$. The radial coordinate r is not a compactified radial coordinate as in the previous case, in the sense that the AdS boundary is located at $r \to \infty$. This system of coordinates allows us to set up a characteristic-type system of evolution of equations. In contrast to the coordinates (t, x), the coordinates (u, r) do not allow us to follow the field up to the AdS boundary. Instead, we want to use them in order to track the evolution of the field near collapse, that is, near the centre $r = x = 0$. The fact that the $\{u = const.\}$ hypersurface are outgoing means that as we evolve in u we approach faster the collapse than in the case of the Cauchy evolution. As we will see, the

characteristic evolution allows us to get much closer to the formation of an AH than the Cauchy evolution. The equations for this case are given in Sec. 2.3.2.

2.3.1 Cauchy-type Evolution of the EKG System

Following previous work on the evolution of scalar fields in AdS [5, 54] and our previous discussion, the metric of an spherically symmetric AAdS spacetime in $d+1$ dimensions can be written as

$$ds^2 = \frac{\ell^2}{\cos^2 x}\left(-Ae^{-2\delta}\,dt^2 + \frac{dx^2}{A} + \sin^2 x\, d\Omega_{d-1}^2\right), \tag{2.17}$$

where $d\Omega_{d-1}^2$ is the metric of the unit $(d-1)$-sphere S^{d-1}, A and δ are the two metric functions that completely determine the metric and depend only on (t, x), and ℓ is the AdS length scale, which is related to the cosmological constant Λ by the expression:

$$\ell^2 = -d(d-1)/2\,\Lambda. \tag{2.18}$$

The dimensionless time coordinate t has an infinite range, i.e. $t \in (-\infty,\infty)$, whereas x is a radial compactified coordinate that goes from $x = 0$ (centre) to $\pi/2$ (AdS boundary). We can recover AdS spacetime by setting $A = 1$ and $\delta = 0$.

From the Eqs. (2.14) and (2.15) we can derive partial differential equations (PDEs) for A, δ, and ψ (see, e.g. [5]). We are interested in discretising our equation using the pseudospectral multidomain method, see Sec. 1.3 for details. In this sense, and to have a proper communication between the boundaries of the domains, we need a first order formulation of the equations based on the characteristic variables associated with our dynamics. The Klein-Gordon equation (2.15) for our metric becomes the following second order PDE:

$$\begin{aligned}\ddot{\phi} - A^2e^{-2\delta}\phi'' =& \frac{\dot{A}}{A}\dot{\phi} - \dot{\delta}\dot{\phi} + Ae^{-2\delta}\phi'A' - A^2e^{-2\delta}\delta'\phi' \\ &+ \ (d-1)\frac{A^2e^{-2\delta}}{\cos x \sin x}\phi'\,.\end{aligned}$$

To reduce the order of the equation we introduce the variables:

$$\Pi = \dot{\phi}\,, \qquad \Phi = \phi'\,. \tag{2.19}$$

The equations for our dynamical variables $\boldsymbol{W} = (\phi, \Pi, \Phi)$ constitute a first order system of PDEs that can be derived from these definitions and from Eq. (2.19):

$$\dot{\phi} = \Pi\,, \tag{2.20}$$

$$\begin{aligned}\dot{\Pi} - A^2 e^{-2\delta}\Phi' &= \frac{\dot{A}}{A}\,\Pi - \dot{\delta}\,\Pi + A e^{-2\delta} A'\Phi \\ &- A^2 e^{-2\delta}\delta'\Phi + (d-1)\frac{A^2 e^{-2\delta}}{\cos x \sin x}\Phi\,,\end{aligned} \tag{2.21}$$

$$\dot{\Phi} - \Pi' = 0\,. \tag{2.22}$$

This set of first order PDEs admits the following compact form:

$$\partial_t \boldsymbol{W} + \mathcal{A}[x, \boldsymbol{W}] \cdot \partial_x \boldsymbol{W} = \boldsymbol{S}[x, \boldsymbol{W}]\,, \tag{2.23}$$

where $\mathcal{A}$ is a matrix and $\boldsymbol{S}$ a vector that depend on the radial coordinate x and the variables $\boldsymbol{W}$. From Eqs. (2.20)-(2.22), the components of the matrix $\mathcal{A}$ are:

$$\mathcal{A} = \begin{pmatrix} 0 & 0 & 0 \\ 0 & 0 & -A^2 e^{-2\delta} \\ 0 & -1 & 0 \end{pmatrix}\,, \tag{2.24}$$

and the components of the vector $\boldsymbol{S}$ are:

$$\boldsymbol{S} = \begin{pmatrix} \Pi \\ \frac{\dot{A}}{A}\,\Pi - \dot{\delta}\,\Pi + A e^{-2\delta} A'\Phi - A^2 e^{-2\delta}\delta'\Phi + (d-1)\frac{A^2 e^{-2\delta}}{\cos x \sin x}\Phi \\ 0 \end{pmatrix}\,. \tag{2.25}$$

The characteristic structure of this hyperbolic system of first order PDEs is determined exclusively by the matrix $\mathcal{A}$, see Sec. 1.2.3 for details, in such a way that the eigenvectors of $\mathcal{A}$ correspond to the different characteristic fields of the system and the eigenvalues to the characteristic speeds associated with the eigenvectors. To study the hyperbolicity of the problem, we have to solve the eigenvalue problem:

$$\mathcal{A}\,\boldsymbol{E} = \sigma \boldsymbol{E}\,, \tag{2.26}$$

where $\boldsymbol{E}$ is a vector in the space $\{(\phi, \Pi, \Phi)\}$. By analysing Eq. (2.26) we find that we have a complete set of real eigenvalues and eigenvectors, so our system is strongly hyperbolic, as expected for a system of PDEs that is equivalent to the Klein-Gordon equation. The resulting set of eigenvalues and eigenvectors is:

$$\sigma_1 = 0 \quad \longrightarrow \quad \boldsymbol{E}_1 = (1, 0, 0)\,, \tag{2.27}$$

$$\sigma_2 = +A e^{-\delta} \quad \longrightarrow \quad \boldsymbol{E}_2 = (0, -A e^{-\delta}, 1)\,, \tag{2.28}$$

$$\sigma_3 = -A e^{-\delta} \quad \longrightarrow \quad \boldsymbol{E}_3 = (0, +A e^{-\delta}, 1)\,. \tag{2.29}$$

The existence of the complete set of eigenvectors here obtained allows us to choose

a new set of variables, the characteristic variables, that have a known propagation velocity, these eigenvalues. The field ϕ does not propagate, or in other words, it propagates with zero speed, and we also have two more characteristic fields that propagate with speeds $\mp A\, e^{-\delta}$. We can diagonalise the matrix $\mathcal{A}$ by using the matrix transformation: $\mathcal{A} = \mathcal{K}\cdot\mathcal{D}_{\mathcal{A}}\cdot\mathcal{K}^{-1}$, where $\mathcal{D}_{\mathcal{A}} = \mathrm{diag}(0, A\, e^{-\delta}, -A\, e^{-\delta})$ and $\mathcal{K}$ is a matrix whose columns are made out of the eigenvectors $\boldsymbol{E}_i$, that is $\mathcal{K} = (\boldsymbol{E}_1, \boldsymbol{E}_2, \boldsymbol{E}_3)$. This transformation defines a new set of variables $\boldsymbol{Y}$ as follows: $\boldsymbol{Y} = \mathcal{K}^{-1}\cdot\boldsymbol{W}$. We can see that the principal part of our set of equations becomes completely decoupled for the variables $\boldsymbol{Y}$. These are the characteristic variables. The first one is ϕ, with zero associated propagation speed (eigenvalue), and the other two are:

$$Y_+ = \Phi - \frac{\Pi}{A\, e^{-\delta}}\,, \tag{2.30}$$

$$Y_- = \Phi + \frac{\Pi}{A\, e^{-\delta}}\,. \tag{2.31}$$

The characteristic variable Y_+ propagates with speed $A\, e^{-\delta}$ and Y_- with speed $-A\, e^{-\delta}$ respectively. Since $A\, e^{-\delta} > 0$, Y_+ is a field propagating to the right and Y_- is a field propagating to the left. For the purpuse of the numerical implementation of our equations, we rescale the variables by a cosine factor and the final version of our characteristic variables is:

$$U = \frac{1}{\cos^{d-2} x}\left(\phi' - \frac{e^{\delta}}{A}\dot{\phi}\right)\,, \tag{2.32}$$

$$V = \frac{1}{\cos^{d-2} x}\left(\phi' + \frac{e^{\delta}}{A}\dot{\phi}\right)\,. \tag{2.33}$$

We also introduce the normalised version of the scalar field itself:

$$\psi = \frac{\phi}{\cos^{d-1} x}\,. \tag{2.34}$$

The use of the (U, V) variables is crucial for our numerical scheme. As we have seen, these characteristic variables have a well defined propagation direction and that allows us to know how to deal with the fields at the boundaries between the different domains. In Fig. 2.9 there is a diagram of the algorithm used in our formulation. In principle, the right boundary of one domain and the left boundary of the following represent the same physical point and therefore they must be identified. The evolution ODEs that result from the spatial discretisation with the PSC method are solved in just one of these two points and then copied to the other. Which point we compute is determined by the propagation direction of the corresponding field as, it is shown in the figure. These variables are not important only for the domain boundaries but also for the global boundaries, $x = 0$ and $x = \pi/2$. With the characteristic variables any kind of boundary conditions can be set in a clear and simple manner.

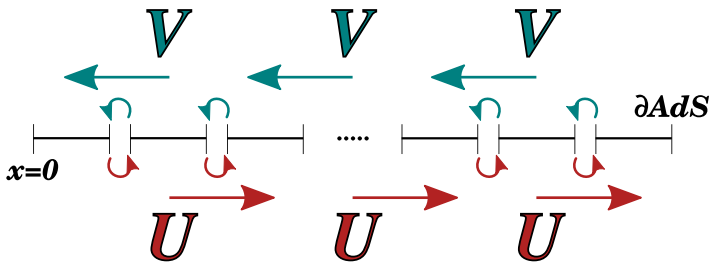

Figure 2.9: Diagram of the Multidomain Structure for PSC Methods. The evolution variables need to be communicated between domains using the characteristic variables, U and V, which have a well defined direction of propagation. The communication is done by copying the boundary values in the direction indicated by the arrows.

From Eqs. (2.14) and (2.15) we derive the set of PDEs for (ψ, U, V, A, δ):

(i) Evolution equations:

$$\dot{\psi} = \frac{Ae^{-\delta}}{2\cos x}(V-U)\,, \tag{2.35}$$

$$\begin{aligned}\dot{U} &= -Ae^{-\delta}U_{,x} - \frac{(d-2\cos^2 x)}{\sin x\cos x}U\,e^{-\delta}(1-A)\\ &- \tfrac{1}{2}\tfrac{(d-1)Ae^{-\delta}}{\sin x\cos x}(U+V) + (d-2)\tfrac{\sin x}{\cos x}U\,Ae^{-\delta}\,,\end{aligned} \tag{2.36}$$

$$\begin{aligned}\dot{V} &= Ae^{-\delta}V_{,x} + \frac{(d-2\cos^2 x)}{\sin x\cos x}V\,e^{-\delta}(1-A)\\ &+ \tfrac{1}{2}\tfrac{(d-1)Ae^{-\delta}}{\sin x\cos x}(U+V) - (d-2)\tfrac{\sin x}{\cos x}V\,Ae^{-\delta}\,,\end{aligned} \tag{2.37}$$

$$\dot{A} = -\tfrac{1}{2}A^2e^{-\delta}\sin x\,\cos^{2d-3}x\,(V^2-U^2)\,, \tag{2.38}$$

(ii) Constraint equations[1]:

$$A' = \frac{d-2+2\sin^2 x}{\sin x \cos x}(1-A) - \frac{A}{2}\sin x \cos^{2d-3} x \left(V^2+U^2\right) , \tag{2.39}$$

$$\delta' = -\tfrac{1}{2}\sin x \cos^{2d-3} x \left(V^2+U^2\right) . \tag{2.40}$$

It is interesting to note that we have an evolution and a constraint equation for A. As we have already indicated, only the scalar field sector has a hyperbolic structure, Eqs. (2.36) and (2.37), while the evolution of A does not contain any gradients of the variables. In practice, we can solve for A either by evolving it using Eq. (2.38) or by solving Eq. (2.39) which only involves radial derivatives. On the other hand, from the definitions of U and V, Eqs. (2.32) and (2.33), we can find a constraint equation for the scalar field ϕ:

$$\phi' = \frac{1}{2}\cos^{d-2} x \left(U+V\right) , \tag{2.41}$$

and therefore, a contrain equation also for the normalised scalar field ψ:

$$\psi' = \psi \frac{\sin x}{\cos x}(d-1) + \frac{1}{2}\frac{U+V}{\cos x} . \tag{2.42}$$

Then, like in the case of A, we can solve for ψ either by evolving Eq. (2.35) or by solving this constraint equation.

To be able to solve Eqs. (2.35)-(2.42) we need boundary conditions at the centre $x = 0$ and at the AdS boundary $x = \pi/2$. Near $x = 0$ we find that the scalar field variables admit the following power expansion:

$$\psi = \psi_0 + \psi_2 x^2 + O(x^4) , \tag{2.43}$$
$$U = U_0 + U_1 x + U_2 x^2 + O(x^3) , \tag{2.44}$$
$$V = -U_0 + U_1 x - U_2 x^2 + O(x^3) , \tag{2.45}$$

and the metric functions have the expansions:

$$A = 1 + A_2 x^2 + O(x^4) , \tag{2.46}$$
$$\delta = \delta_0 + \delta_2 x^2 + O(x^4) , \tag{2.47}$$

where δ_0 is a time-dependent quantity always greater than zero.

[1]The distinction between evolution and constraint equations we use here is not in correspondence with the evolution and constraint equations of the well-known 3+1 ADM formalism introduced in Sec. 1.2.1.

We can also obtain a power expansion near the AdS boundary by introducing a coordinate change in the radial direction:

$$\rho = \pi/2 - x. \tag{2.48}$$

Then, the expansions for the normalised scalar field ψ and the characteristic variables U and V are:

$$\psi = \psi_1 \rho + O(\rho^3)\,, \tag{2.49}$$
$$U = U_1 \rho + U_2 \rho^2 + O(\rho^3)\,, \tag{2.50}$$
$$V = U_1 \rho - U_2 \rho^2 + O(\rho^3)\,, \tag{2.51}$$

and for the metric functions A and δ:

$$A = 1 + O(\rho^d)\,, \tag{2.52}$$
$$\delta = O(\rho^{2d})\,. \tag{2.53}$$

From this expansions we obtain the boundary conditions for the origin:

$$\psi = \psi_0 \tag{2.54}$$
$$U = -V \tag{2.55}$$
$$A = 1 \tag{2.56}$$
$$\delta = \delta_0 \tag{2.57}$$

and for the AdS boundary:

$$\psi = U = V = 0 \tag{2.58}$$
$$A = 1 \tag{2.59}$$
$$\delta = 0 \tag{2.60}$$

2.3.2 Characteristic-type Formulation of the EKG System

For the characteristic evolution, we adapt the scheme used in Refs. [16, 18] to the case of AAdS spacetimes with spherical symmetry. The form of the metric is:

$$ds^2 = -g\bar{g}\, du^2 - 2g\, du dr + r^2\, d\Omega^2_{d-1}\,, \tag{2.61}$$

where u is an outgoing null coordinate ($u = const.$ is a family of outgoing null geodesics) and r is the radial area coordinate. The coordinate range for (u, r) is: $u \in (-\infty, \infty)$ and $r \in (0, +\infty)$. The AdS boundary corresponds to $r \to \infty$. The functions $g = g(u, r)$ and $\bar{g} = \bar{g}(u, r)$ are always greater that some normalisation value at the origin that we choose to be unity. The AdS limit for the metric variables

is:

$$\begin{aligned} g &\to 1, \\ \bar{g} &\to 1 + \frac{r^2}{\ell^2}. \end{aligned} \tag{2.62}$$

The coordinates (u, r) have dimensions of length and, throughout this chapter, the numerical values that we quote are in units of the length scale ℓ.

To write down the field equations, Eqs. (2.14) and (2.15), in the coordinates of Eq. (2.61) we introduce two variables associated with the scalar field ϕ:

$$\bar{h} = \phi \,, \tag{2.63}$$

and

$$\frac{d-1}{2} r^{\frac{d-3}{2}} h = \left(r^{\frac{d-1}{2}} \bar{h} \right)_{,r} . \tag{2.64}$$

Then, we can recover $\bar{h}$ from h by integration as follows

$$\bar{h}(u, r) = \frac{d-1}{2} r^{\frac{1-d}{2}} \int_0^r r'^{\frac{d-3}{2}} h(u, r') \, dr' \,. \tag{2.65}$$

Moreover, from the (r, r) and (u, r) components of the EFEs for the metric of Eq. (2.61), we get:

$$g_{,r} = r g (\bar{h}_{,r})^2 \,, \tag{2.66}$$

$$\left(r^{d-2} \, \bar{g} \right)_{,r} = \left(d - 2 + d \frac{r^2}{l^2} \right) r^{d-3} g \,, \tag{2.67}$$

and from here, we can solve for the metric variables $(g, \bar{g})$ in terms of the scalar field variables $(h, \bar{h})$ as follows:

$$g(u, r) = \exp \left\{ \frac{(d-1)^2}{4} \int_0^r dr' \frac{\left(h(u, r') - \bar{h}(u, r') \right)^2}{r'} \right\} \,, \tag{2.68}$$

$$\bar{g}(u, r) = \frac{1}{r^{d-2}} \int_0^r dr' \left(d - 2 + d \, \frac{r'^2}{\ell^2} \right) r'^{d-3} \, g(u, r') \,. \tag{2.69}$$

Therefore, we can find all the variables of the problem from h. An important observation about Eq. (2.69) is that both the numerator and denominator of the right-hand side go to zero as we approach the origin, i.e. $r = 0$, although they do it in a way that the limit is well-defined and finite. However, this can problematic from the point of view of the convergence of a numerical algorithm. Then, following [31, 32] we can get an alternative form for this equation by using integration by parts. The

result is:

$$\begin{aligned}\bar{g}(u,r) = &\left(1+\frac{r^2}{\ell^2}\right) g(u,r) - \\ &- \frac{(d-1)^2}{4\,r^{d-2}} \int_0^r dr' r'^{d-3} \left(1+\frac{r'^2}{\ell^2}\right) \left(h(u,r') - \bar{h}(u,r')\right)^2 \, g(u,r')\,,\end{aligned} \tag{2.70}$$

where we have used the boundary conditions at the origin and Eq. (2.68) for $g(u,r)$. Now, the second term in this equation goes to zero as we approach the origin and hence, it is more amenable for numerical computations. The only remaining equation is the one for h, which can be obtained from the Klein-Gordon equation 2.15

$$\frac{\partial^2 \bar{h}}{\partial u \partial r} - \frac{1}{2}\frac{\partial}{\partial r}\left(\bar{g}\frac{\partial \bar{h}}{\partial r}\right) + \frac{d-1}{2r}\left(\frac{\partial \bar{h}}{\partial u} - \bar{g}\frac{\partial \bar{h}}{\partial r}\right) = 0\,. \tag{2.71}$$

Using Eq. (2.64), the equation for h is

$$\frac{\partial h}{\partial u} - \frac{1}{2}\bar{g}\frac{\partial h}{\partial r} = \frac{h-\bar{h}}{2\,r}\left[\left(d-2+d\frac{r^2}{\ell^2}\right) g - \frac{d-1}{2}\bar{g}\right]\,. \tag{2.72}$$

We use the characteristic initial-value problem in the traditional way, integrating the hyperbolic equations along their associated characteristic lines (see, e.g. [55, 56]). Then, we set up initial data on an initial outgoing null hypersurface $\{u = u_o = const.\}$ and evolve that data onto the next one $\{u = u_o + \Delta u = const.\}$ through the ingoing null geodesics (the purple lines in Fig. 2.10), which are given by

$$\frac{dr}{du} = -\tfrac{1}{2}\bar{g}\,. \tag{2.73}$$

Integrating along the ingoing null geodesics allows us to exchange partial derivatives of our variables by total derivatives with respect to u. For instance, in the case of the field variable h we have

$$\frac{dh(u,r(u))}{du} = \left(\frac{\partial h}{\partial u}\right)_{r=r(u)} + \left(\frac{\partial h}{\partial r}\right)_{r=r(u)} \frac{dr(u)}{du}\,, \tag{2.74}$$

where $r(u)$ is an ingoing null geodesic, a solution of Eq. (2.73). In this way we can replace Eq. (2.72) by two ODEs, one for the variable h,

$$\frac{dh}{du} = \frac{h-\bar{h}}{2\,r}\left[\left(d-2+d\,\frac{r^2}{\ell^2}\right) g - \frac{d-1}{2}\bar{g}\right]\,, \tag{2.75}$$

and another one for $r(u)$, namely Eq. (2.73). The first one, Eq. (2.75), tells us how to evolve h from a $\{u = \text{const.}\}$ hypersurface to the next one. The second one tells us that the coordinate r of a point in $\{u = \text{const.}\}$ changes following its own ingoing

null radial geodesic.

The expressions of Eqs. (2.65), (2.70), (2.75) are problematic at $r = 0$ because of the appearance of $1/r$ factors. To understand whether this produces a singularity or the final results are finite we need to study the behaviour of our variables around $r = 0$. Assuming the following expansion for the scalar field $\phi = \bar{h}$:

$$\bar{h} = \phi_0 + \phi_1\, r + \phi_2\, r^2 + O(r^3)\,, \tag{2.76}$$

we obtain the following expansions for the rest of variables:

$$h = \phi_0 + \frac{d+1}{d-1}\phi_1\, r + \frac{d+3}{d-1}\phi_2\, r^2 + O(r^3)\,, \tag{2.77}$$

$$g = 1 + \frac{1}{2}\phi_1^2\, r^2 + O(r^3)\,, \tag{2.78}$$

$$\bar{g} = 1 + O(r^2)\,. \tag{2.79}$$

As we see, the $1/r$ factors should cancel and the final values needs to be finite and can be computed through this expansions.

2.3.3 Transition between the two Formulations

During the Cauchy evolution we can monitor our variables to see when we approach the formation of an AH. Then, at that point we can make the transition from the Cauchy evolution of Sec. 2.3.1 to the characteristic evolution of Sec. 2.3.2 in order to follow better the dynamics near collapse. This transition consists in constructing initial data on an initial null hypersurface $\{u = u_o = \text{const.}\}$ from the outcome of the Cauchy evolution. To that end, it is important to cover a portion of the spacetime that guarantees that the characteristic evolution will cover the formation of the AH. This is illustrated in Fig. 2.10, where the first purple line (a null outgoing geodesic) indicates the initial slice that we choose for the characteristic evolution. As we can see, the initial data for the characteristic evolution needs to be computed using the information from the Cauchy evolution corresponding to an evolution time of $\Delta t \approx \pi/2$ in this way the AH formation is covered.

This transition requires to find the relations between different objects of the Cauchy and characteristic evolutions. First, we need to find the relation between the coordinates (t, x), used for the Cauchy evolution, and the coordinates (u, r) of the characteristic one. The relation between the radial coordinates x and r is quite straightforward considering the factor in front of the metric of the unit $(d-1)$-sphere in Eqs. (2.17) and (2.61), from where we get:

$$r = \ell\, \tan x\,. \tag{2.80}$$

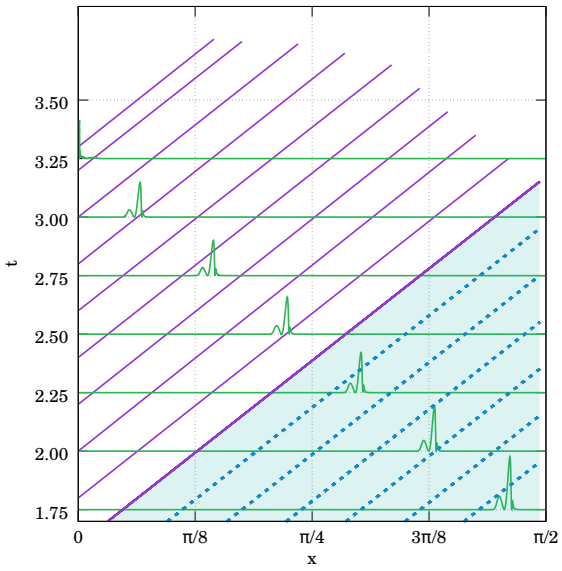

Figure 2.10: Cauchy / Characteristic Evolutions in AdS.. The green (mostly horizontal) lines represent the energy density as computed using the Cauchy evolution at different times (evolution goes in the vertical time direction). Blue dashed lines are characteristics (outgoing null geodesics) computed through the Cauchy data. Purple lines represent the null *surfaces* we have evolved using the characteristic scheme, being the thickest purple line the initial one. The characteristic grid moves according to Eq. (2.73) and therefore the range in r covered decreases over time.

The second important ingredient is the construction of the initial null hypersurface for the characteristic evolution from the information extracted from the Cauchy evolution. This can be done by finding the outgoing null geodesics from the Cauchy evolution. From the expression of the metric in Eq. (2.17) the outgoing null geodesics are given by:

$$\frac{dx}{dt} = +Ae^{-\delta} \equiv v(t,x)\,, \tag{2.81}$$

where the plus sign denotes that these radial null geodesics are outgoing (a minus sign corresponds to ingoing null geodesics). To integrate this ODE we need the values of the metric functions $A(t,x)$ and $\delta(t,x)$, from the Cauchy evolution, over the spacetime region that includes the null geodesics of interest. Some of these geodesics are shown in a $t-x$ diagram in Fig. 2.10.

The next important ingredient is the construction of initial data for the characteristic evolution on one of the null outgoing geodesics that constitute the slicing $\{u = \text{const.}\}$. To begin with, let us apply the coordinate transformation of

Eq. (2.80), adding also the transformation:

$$\tau = \ell\, t, \tag{2.82}$$

to the metric in Eq. (2.17). This brings the metric to a more familiar form:

$$ds^2 = -Ae^{-2\delta}\left(1+\frac{r^2}{\ell^2}\right)d\tau^2 + \frac{dr^2}{A\left(1+\frac{r^2}{\ell^2}\right)} + r^2\, d\Omega_{d-1}^2\,. \tag{2.83}$$

The AdS limit $A \to 1$ and $\delta \to 0$ gives us the well-known form of the AdS spacetime metric. With this in mind, let us perform a general coordinate transformation from the Cauchy-formulation metric to the characteristic-formulation metric:

$$\tau = \mathcal{F}(u, r)\,, \tag{2.84}$$

which transforms the metric in Eq. (2.83) into the metric

$$\begin{aligned} ds^2 &= -Ae^{-2\delta}\left(1+\frac{r^2}{\ell^2}\right)\mathcal{F}_u^2\, du^2 \\ &- 2Ae^{-2\delta}\left(1+\frac{r^2}{\ell^2}\right)\mathcal{F}_u\mathcal{F}_r\, du dr \\ &+ \left[1 - A^2e^{-2\delta}\left(1+\frac{r^2}{\ell^2}\right)^2\mathcal{F}_r^2\right]\frac{dr^2}{A\left(1+\frac{r^2}{\ell^2}\right)} \\ &+ r^2\, d\Omega_{d-1}^2\,, \end{aligned} \tag{2.85}$$

where $\mathcal{F}_u \equiv \partial\mathcal{F}/\partial u$ and $\mathcal{F}_r \equiv \partial\mathcal{F}/\partial r$. Now, let us impose two conditions on the general coordinate transformation of Eq. (2.84). The first one comes from the comparison of this general metric to the characteristic metric of Eq. (2.61) and the fact that the vector $\partial/\partial r$ is a null vector for the second metric. This imposes the condition:

$$\mathrm{g}_{rr} = 0, \tag{2.86}$$

on the general metric of Eq. (2.85). And this translates into the following condition on $\mathcal{F}$:

$$\mathcal{F}_r = \frac{1}{\left(1+\frac{r^2}{\ell^2}\right)Ae^{-\delta}}\,. \tag{2.87}$$

Here we have made a sign choice. In the case of ingoing null geodesics we would have chosen the opposite sign for $\mathcal{F}_r$. The second condition that we impose on the coordinate change has to do with the freedom in rescaling the coordinate u, which is a freedom in the choice of the quantity $\mathcal{F}_u$. Our choice, motivated by the implementation of the Cauchy-characteristic transition, is:

$$\mathcal{F}_u = e^{\delta_0}\,, \tag{2.88}$$

where δ_0 is the value of the metric function δ at $x = 0 = r$. Now, by comparing the line element in Eq. (2.85) with the one for the characteristic formulation in Eq. (2.61), and using the conditions on the function $\mathcal{F}$ given in Eqs. (2.87) and (2.88), we find the following relations between (A, δ) and $(\bar{g}, g)$:

$$g = e^{\delta_0 - \delta}\,, \tag{2.89}$$

$$\bar{g} = A e^{\delta_0 - \delta}\,\frac{1}{\cos^2 x}\,, \tag{2.90}$$

$$A = \frac{\bar{g}}{g\left(1 + \frac{r^2}{\ell^2}\right)}\,. \tag{2.91}$$

These are key relations for the construction of the initial data at $u = u_0$. Given that AH formation in the Cauchy evolution is given by the limit $A \to 0$, from Eq. (2.91) we have that in the characteristic evolution we can track AH formation by monitoring the right-hand side of this equation using the values of $(r, g, \bar{g})$.

On the other hand, from our particular coordinate change, Eqs. (2.84), (2.87), and (2.88), we have the following relation between τ and u (and r):

$$\begin{aligned}\tau &= u + \ell \int_0^x \frac{dx'}{v(t_+(x'), x')} \\ &= u + \int_0^r \frac{dr'}{\left(1 + \frac{r'^2}{\ell^2}\right) v(t_+(r'), r')}\,,\end{aligned} \tag{2.92}$$

where $t_+(x)$ denotes the solution for the outgoing null geodesics, Eq. (2.81), and v is the function of (t, x) defined there.

Finally, we give the relations between the metric and scalar field variables in both formulations. First, ψ and $\bar{h}$ are, by definition, directly related with the scalar field:

$$\bar{h} = \phi = \cos^{d-1} x\, \psi\,. \tag{2.93}$$

The scalar field variable h can be constructed along the outgoing null geodesics in term of the Cauchy variables as follows:

$$\begin{aligned}h &= \bar{h} + \frac{2}{d-1} r\, \bar{h}_{,r} \\ &= \phi + \frac{2}{d-1} r(x) \left(\frac{\partial x}{\partial r}\frac{\partial}{\partial x} + \frac{\partial t}{\partial r}\frac{\partial}{\partial t}\right)\phi \\ &= \cos^{d-1} x \left(\psi + \frac{2}{d-1}\sin x\; V\right)\,,\end{aligned} \tag{2.94}$$

where we have used Eqs. (2.33), (2.64), (2.80), and (2.92). It is important to notice that h depends on the scalar field itself, through the variable ψ, and the ingoing (negative speed) characteristic variable V [see Eq. (2.33)], but not on the outgoing (positive

speed) characteristic variable U [see Eq. (2.32)]. The reason for this is that we are carrying out the characteristic evolution using null slices made out of outgoing null geodesics, and hence the evolution of h from one slice to the next one takes place along ingoing null geodesics [see Eq. (2.73)].

In summary, Eqs. (2.89)-(2.94) provide all the information we need to construct the initial null slice using the Cauchy evolution, the associated coordinate change, and the initial data to initiate the characteristic evolution. This completes the design of the procedure to perform the transition from the Cauchy evolution to the characteristic one.

2.4 Basics of the Numerical Implementation

In this section we describe the basic ingredients for the numerical implementation of the two evolution schemes and the transition between them. In the case of the Cauchy evolution we use pseudospectral collocation methods with multiple domains, building on previous works that have developed this type of techniques for the computation of the self-force on a charge particle orbiting a black-hole spacetime [57, 58, 59]. For the characteristic evolution we use the method introduced in Ref. [16], consisting in using a null foliation where the points of each slice follow ingoing null geodesics (the *characteristic lines*). Finally, we describe how we store the information from several Cauchy slices in order to construct the initial null slice and initial data for the characteristic evolution.

2.4.1 Numerical Implementation of the Cauchy Evolution

In order to have a precise numerical evolution we are going to use Pseudo-Spectral Collocation (PSC) methods for the space discretization, which in our case is just the radial direction, the compactified radial coordinate x to be more precise. The main tools of the PSC method that we use are described in Sec. 1.3. In a standard spectral method the outcome of the spatial discretization of a set of hyperbolic PDEs is a set of ODEs for the time-dependent spectral coefficients. Instead, in the PSC method we obtain a set of ODEs for the time-dependent values of our evolution variables, $\boldsymbol{U} = (U, V, ...)$, at the collocation points, $\{\boldsymbol{U}_i(t) \equiv \boldsymbol{U}(t, x_i)\}$, where the equations are forced to be satisfied exactly. The number of ODEs that we obtain is equal to the total number of variables (N_v) times the number of collocation points (N), i.e. $N \times N_v$. The numerical evolution of the resulting ODEs for the collocation values $\{\boldsymbol{U}_i(t)\}$ is performed using a standard Runge-Kutta 4 (RK4) algorithm (see, e.g. [60, 61]).

The great advantage of the PSC method is that for smooth solutions it provides exponential convergence, i.e. the truncation error of the spectral series, which can

be approximated by the absolute value of the last spectral coefficient, $|a_N|$, decays as e^{-N}. In contrast, the cost of most operations like derivatives, computation of non-linear terms, etc. increases as N^2 with the number of collocation points, unless we use a fast Fourier algorithm to transform from the physical space (the collocation values of our variables) to the spectral space (the coefficients of the spectral series for our variables), in which case the cost increases only as $N \log N$. In addition, the Courant-Friedrichs-Lewy (CFL) condition for the stability of the evolution of the PDEs (see, e.g. [62]), in the case of our PSC scheme, is of the form $\Delta t < C\, N^{-2}$ (where C is a certain constant independent of N). This is in contrast with the typical form of standard finite-difference schemes for PDEs, where $\Delta t < C'\, N^{-1}$ and C' is another constant. This is due to the structure of the Lobatto-Chebyshev grid that we use, where the points cluster near the boundaries of the domain. As a consequence, the evolution in the PSC method can be significantly more expensive than in the case of finite-difference schemes. A way to alleviate this is to use refinement via a multidomain PSC method. The idea is to adapt the size and number of the domains so that different regions in the radial direction with different resolution requirements are covered by an adequate number of collocation points. We can change the number and size of the different domains along the evolution, following the resolution needs of the problem. The practical implementation of the AMR is described in Sec. 2.4.2. Most computations are done at each domain in an independent way. The different domains are connected via the corresponding matching conditions as it was described in Sec. 2.3.1.

The Cauchy evolution allows us to follow the system from its initial conditions to the latest stages, just before the collapse and the formation of an AH. As we have already mentioned we can expect the scalar field to travel to the AdS boundary ($x = \pi/2$) several times, and in this sense using the compactified radial coordinate x gives us control over the whole space. On the other hand, when the scalar field is close to collapse, large gradients will be generated in our variables and the AMR is crucial in order to guarantee the high resolution requirements needed to resolve the dynamics.

In Sec. 2.3.1 we have presented the equations we obtain from Einstein's field equations and from energy-momentum conservation in terms of the Cauchy-type variables, namely (ψ, U, V, A, δ). Some variables have two equations, for instance the metric function A can be obtained either by evolving Eq. (2.38) or by integrating Eq. (2.39) and the same happens with the scalar field variable ψ [See Eqs. (2.35) and (2.42)]. We have numerically implemented several combinations of equations but, in general, we have obtained the best results and efficiency by evolving in time U and V [with Eqs. (2.36) and (2.37)] and then obtaining ψ, A, and δ from radial integration [with Eqs. (2.42), (2.39), and (2.40) respectively].

From Eqs. (2.39) and (2.40) we can find an integral expression for the metric functions A and δ in terms of radial integrals:

$$A(t,x) - 1 = \\ -\frac{\cos^d x\, e^{\delta}}{2\sin^{d-2} x}\int_0^x dy\, e^{-\delta}\sin^{d-1} y\cos^{d-3} y(U^2+V^2)\,, \tag{2.95}$$

$$\delta(t,x) = \frac{1}{2}\int_x^{\frac{\pi}{2}} dy\, \sin y\cos^{2d-3} y\left(U^2+V^2\right)\,, \tag{2.96}$$

and using Eq. (2.42) we have the following expression for the scalar field:

$$\psi(t,x) = -\frac{1}{\cos^{d-1} x}\int_x^{\pi/2} dy\, \cos^{d-2} y\left(U^2+V^2\right)\,. \tag{2.97}$$

On the other hand, we can introduce the energy density

$$\mathcal{E}(t,x) = e^{-\delta}\sin^{d-1} y\cos^{d-3} y\left(\frac{U^2+V^2}{2}\right)\,, \tag{2.98}$$

and from it we can compute the energy contained inside a sphere of a given radius x, which we call the mass function:

$$\mathcal{M}(t,x) = e^{\delta}\int_0^x dy\,\mathcal{E}(t,y)\,, \tag{2.99}$$

which is related to the metric function A by

$$A(t,x) = 1 - \frac{\cos^d x}{\sin^{d-2} x}\mathcal{M}(t,x)\,. \tag{2.100}$$

Then, the ADM mass is just the limit:

$$M_{\rm ADM} = \lim_{x\to\pi/2}\mathcal{M}(t,x). \tag{2.101}$$

The ADM mass is a constant that should not change during the evolution and then it can be used in our simulations to check the numerical accuracy of the numerical method. In addition, we can define the following quantity:

$$x_{\rm CM} = \frac{1}{M_{\rm ADM}}\int_0^x dy\, y\,\mathcal{E}(t,y)\,, \tag{2.102}$$

which plays the role of a radial *centre of mass*, in the sense that we can use it to track where the energy of the scalar field is concentrated, which is specially useful when

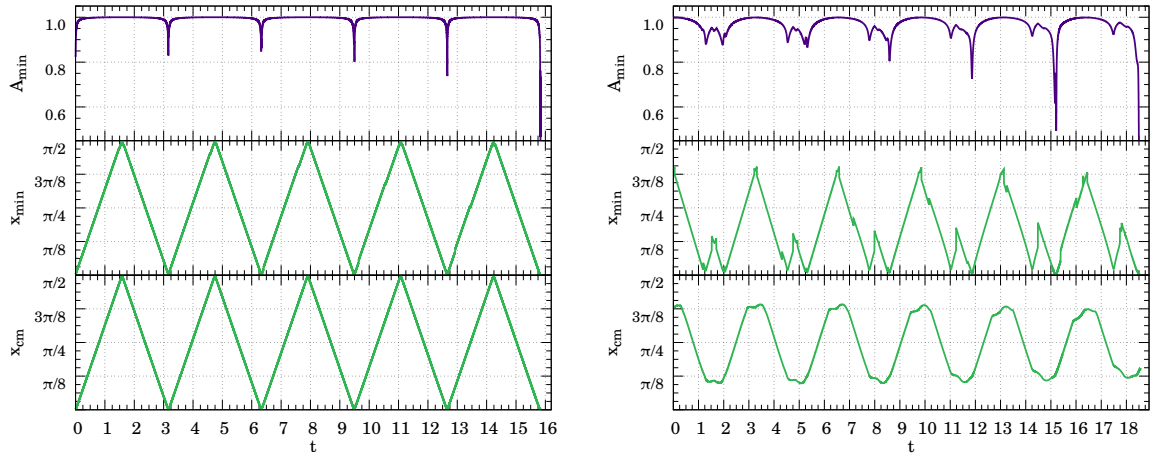

Figure 2.11: ***Centre-of-mass* Evolution.** In the left plot we show the evolution of $A_{\rm min}$, $x_{\rm min}$, $x_{\rm CM}$ for the initial conditions in Eq. (2.113), that collapse after five bounces. In the right plot we use an initial profile from Eq. (2.121).

evolving localised scalar field configurations, like for instance those corresponding to the initial conditions given in Eq. (2.113). There are other possible definitions of a radial centre of mass, for instance we can use the radial position of the minimum of the metric function A, i.e. $x_{\rm min}$ such that $A(x_{\rm min}) = \min(A(x)) \equiv A_{\rm min}$. We compare these two definitions of radial centre of mass, $x_{\rm CM}$ and $x_{\rm min}$, in Fig. 2.11, where their evolution is compared with the evolution of $A_{\rm min}$ for two different sets of initial data, the one given in Eq. (2.113), which collapses after five round trips to the AdS boundary, and the one given in Eq. (2.121). As we can see in Fig. 2.11, for the initial profiles in Eq. (2.113) (left panel) the differences between $x_{\rm min}$ and $x_{\rm CM}$ are quite small although $x_{\rm min}$ presents some small abrupt features. These features are more prominent for the more complex initial profile of Eq. (2.121) (right panel), where the evolution of both $x_{\rm CM}$ and $x_{\rm min}$ is more complex, but x_{cm} appears to be a much smoother indicator to track the evolution of the scalar field profile.

Finally, regarding more technical details of the numerical implementation, it is important to mention that all the operations involving the spatial radial direction, including the integrals, are performed within the framework of the multidomain PSC method. Another important ingredient of the numerical implementation is how to deal with the multiple domains. In our scheme, the boundaries of each domain have duplicated information because the boundary points of one domain are identified, with the exception of the global boundaries ($x = 0$ and $x = \pi/2$), with the boundary points of the contiguous domains. Although most operations are done locally at each domain we need to communicate the different domains through these boundary points. This is the main reason why we have introduced the characteristic variables U and V, which are crucial in order to establish the communication between domains. The characteristic variable U always propagates with positive

speed (in direction to the AdS boundary) and the characteristic variable V always travels with negative speed (towards the origin). Then, the way to communicate two given contiguous domains during the Cauchy evolution is to take the value of the variable U from the right boundary of the domain to the left and to copy it into the U-value of the left boundary of the domain to the right (see Fig. 2.9) and the equivalent procedure for V: We take the value of the variable V from the left boundary of the domain to the right and copy it into the V-value of the right boundary of the domain to the left. This way of communicating the characteristic variables ensures that we will not find discontinuities in our variables across the boundaries during the numerical evolution. In other words, we perform the communication between domains according to the directions of propagation of the information.

2.4.2 Adaptive Mesh Refinement for the Cauchy Evolution

The typical scalar field configurations that we consider in this work, which are localised in the radial direction, follow the same evolutionary pattern, already described in Sec. 2.3.1. The scalar field attempts to collapse near the origin but if the initial amplitude is below some threshold, the scalar field disperses towards the AdS boundary. Then, it bounces off the AdS boundary and travels again towards the origin. This sequence is repeated until the scalar field distribution is compact enough to collapse and form an AH. This means that we need to simulate a compact scalar field distribution back and forth and some of the scalar field variables exhibit growing gradients as the evolution proceeds. In order to track the pronounced features of the scalar field during the evolution in an efficient way we resort to AMR techniques based on our multidomain PSC approach, see Sec. 1.3. The aim is to design a method in which the resolution follows the field during the round trips to the AdS boundary with the minimal loss of precision and without slowing down much the evolution. In this sense, it is important to mention that although we know the evolutionary pattern, the details can vary significantly as we change the initial conditions. To illustrate this, in Fig. 2.12 we show the profile of the scalar field variable U at a similar time for two different simulations where collapse happens after one bounce. We see that the shapes are quite different and require different grids in order to resolve them. In Fig. 2.13 we show the profile of U at three different times of a simulation where collapse takes place after three bounces. The snapshots of these figures are taken when the field is travelling towards the boundary so most of the energy is concentrated in the U mode (the one propagating to the right as shown in Fig. 2.9). These figures clearly illustrate the need for AMR in our simulations. We have developed two AMR methods for our simulations.

First Approach: Gradient Density Estimator

The first AMR method for our spectral multidomain grid is based on a functional that we call the *gradient density* functional, defined at each domain as:

$$\rho_{\mathcal{D}} = \frac{1}{N}\int_{\mathcal{D}} dx\, |V_{,x}| \;\geq\; 0\,, \tag{2.103}$$

where $\mathcal{D}$ denotes one of the domains. This indicator is based on the characteristic variable V because is the one that concentrates the energy during the collapse and where more precision is needed. The main idea is to distribute the domain nodes to minimise the gradient density functional. In our numerical experiments we find a threshold for $\rho_{\mathcal{D}}$ above which the evolution is no longer valid because of the appearance of high-frequency numerical noise. Then, during the simulations we modify the domain structure to keep $\rho_{\mathcal{D}}$ below that threshold, adding more domains if needed.

This method works reasonably well for capturing the gradients generated during the collapse but it has several caveats. In particular, it can generate numerical noise far from the region where the scalar field is localised if we do not allow for a minimum resolution there. It can also give problems when the scalar field presents very sharp features that have to be propagated to the AdS boundary and back, which are precisely the most relevant cases in our study.

Second Approach: Domains over a Curve in Configuration Space

We have developed an alternative method that appears to be more robust for dealing with the most extreme cases where the gradients of variables like U and V, despite being smooth functions, are very large at specific locations. The starting point is to consider a combination of our Cauchy variables that reflects in a very clear way the regions where more refinement is needed, that is, where we find the largest variations in our variables, let us call it $\gamma(A, \delta, \psi, U, V)$. For a fixed time, when large gradients in our variables appear, the length of the curve defined in the plane $(x, \gamma(x))$ has a large contribution from the relatively small x-interval where gradients occur. In this situation, let us consider the length of this curve from the origin to a certain radial location x:

$$L(x) = \int_0^x d\tilde{x}\, \sqrt{1 + \gamma'(\tilde{x})^2}\,, \tag{2.104}$$

where $\gamma' = (\partial\gamma/\partial A)A' + \ldots$. The key idea of this refinement method is to distribute the nodes of our domains so that they cover the same length of the curve $(x, \gamma(x))$, in contrast with the traditional choice of taking them equally distributed over the x direction. That is, we select the nodes of our domains, $\{\bar{x}_i\}$, such as: $L(\bar{x}_i) = i\, L(\pi/2)/D$ ($i = 0, \ldots, D$), where D is the total number of domains.

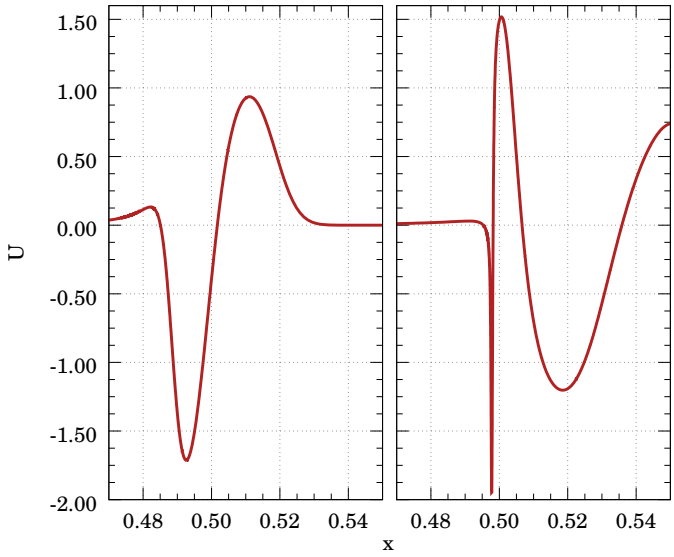

Figure 2.12: Cauchy Refinement: Comparison of Different Initial Configurations. Comparison of the U profile in two different simulations at a similar time. Both of them are supposed to collapse after one bounce but the resolution requirements to follow them are very different.

In our simulations we have seen that this method does not require to establish any threshold, instead we just have to change the multidomain structure after a certain number of time steps to adapt to the changes in the variables in a smooth way. Every time we change the domain structure we have to interpolate the variables into the new grid. The interpolation between the old and new grids is performed via the pseudospectral representation and in this way the numerical error introduced is relatively small.

The specific choice of the function γ is the key ingredient of this method and is quite flexible in the sense that we can tune this choice to the type of initial scalar field profiles or even to the particular state of the numerical evolution. For not very demanding simulations in terms of gradients of our variables we can choose γ to be just A and this provides a very good performance. For more demanding simulations, a better choice is the scalar field characteristic variable U when the field is travelling to the AdS boundary, and V when it is travelling towards the origin. This is motivated by the character of these variables, see Sec. 2.4.1, U is the eigenfunction that captures the movement with positive velocity and V the one that captures the movement with negative velocity. In practice, we have seen that these simple choices work quite well and allow us to resolve the large changes in these variables that appear during the collapse in the most extreme cases.

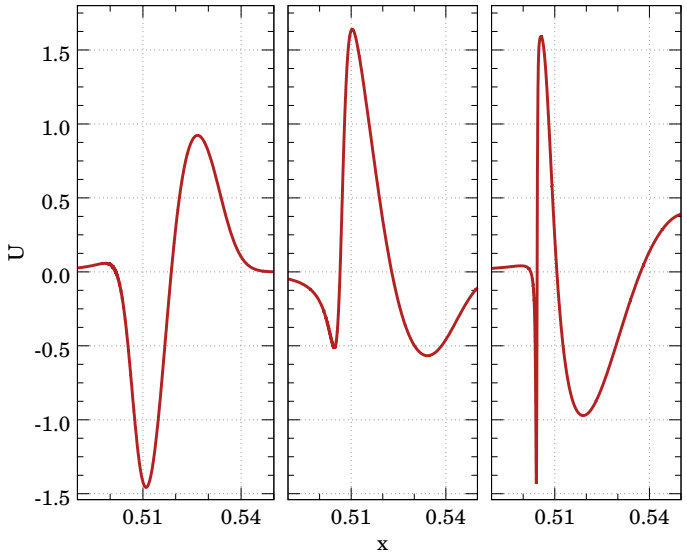

Figure 2.13: Cauchy Refinement: Comparison of Different Time Snapshots. Comparison of U profiles from the same simulation at different times. This configuration collapses after three bounces. The snapshots are taken at the same position during the trip to the AdS boundary.

2.4.3 Numerical Implementation of the Characteristic Evolution

The characteristic evolution described in Sec. 2.3.2 is completely different from the Cauchy one. We need to set a grid on the initial null slice in terms of the radial coordinate r. When we evolve to the next null slice, the r-values of each grid point change following the ingoing null geodesics, see Eq. (2.73). This has two main effects: First, our last grid point (largest value of r, $r_{\max}$) evolves making our physical computational domain to shrink as it is shown in Fig. 2.10. Second, the points near the origin are swallowed because, according to the equation for ingoing null geodesics, these points should evolve to negative values of r which in principle do not have a well-defined physical meaning. This means that we need to control the size of our grid and be careful with the computations near the origin, but other than that the characteristic evolution is not problematic. Actually, the reduction of the grid as we proceed with the evolution helps us to focus our numerical resolution around the region where the collapse takes place so that we do not need mesh refinement methods in this case. In the cases where the collapse does not occur we see that the field gets scattered towards infinity as it would do in the asymptotically flat case [16, 18]. However, since we are considering AAdS spacetimes, the scalar field has to reach the AdS boundary in a finite time, but the region around the AdS boundary is not covered by our characteristic grid. This means that we have made the transition from the Cauchy to the characteristic evolution too early, and therefore

we need to continue the Cauchy evolution until we can construct an initial null slice whose evolution covers the collapse.

To set up our initial characteristic grid it is very important to establish its coordinate size, determined by $r_{\max}$, the r-coordinate of the last grid point. Once this is done, we can freely distribute the other points. A uniform distribution of the grid points in the radial coordinate r is not a good choice because of the CFL condition. For the characteristic evolution the CFL condition implies:

$$\Delta u < \frac{1}{2}\min\left(\frac{r_i - r_{i-1}}{\bar{g}_i}\right) , \tag{2.105}$$

where r_i and r_{i-1} are two contiguous grid points and $\bar{g}_i = \bar{g}(r_i)$. If we have a uniform grid, $r_i - r_{i-1} = \Delta r$ is the same for any i. But when we go to large values of r we have that the metric function $\bar{g}$ behaves as in pure AdS spacetime (because the field is mostly concentrated near $r = 0$), that is: $\bar{g} \sim r^2$. This means that the CFL condition in this case is controlled by the outer grid points, the ones with largest r, where Δu should be too small. But on physical grounds it should be the opposite, the CFL condition should be dominated by the points where we need more resolution, around the region where the AH forms. What we do is to construct a grid where the grid point separation is constant with respect to the radial coordinate x instead of r, thus the outer points are well separated in r. From the Cauchy evolution we extract the values of the scalar field variable h at the different grid points and, from the values of h we find the other variables, $\bar{h}$, g and $\bar{g}$, by integration [using Eqs. (2.65)-(2.69), or Eq. (2.70)]. The first grid point for integration is the origin, where we need to prescribe the boundary conditions:

$$\begin{aligned} &\bar{h}(r=0) = h(r=0)\,, \\ &\bar{g}(r=0) = g(r=0) = 1\,. \end{aligned} \tag{2.106}$$

The integration proceeds to the following grid points by using Simpson's rule:

$$\begin{aligned} I_i &\equiv \int_0^{r_i} dr\, f(r) \\ &= I_{i-1} + \frac{r_i - r_{i-1}}{6}\left[f\left(r_{i-1}\right) + 4f\left(r_M\right) + f\left(r_i\right)\right] , \end{aligned} \tag{2.107}$$

where $r_M \equiv (r_i + r_{i-1})/2$ is the r-coordinate of the midpoint between r_i and r_{i-1}, where the value of the integrand is evaluated using spline interpolation [63].

Each grid point evolves according to the ODE system of Eqs. (2.75) and (2.73). To that end, we use again a standard RK4 algorithm (see Refs. [60, 61]).

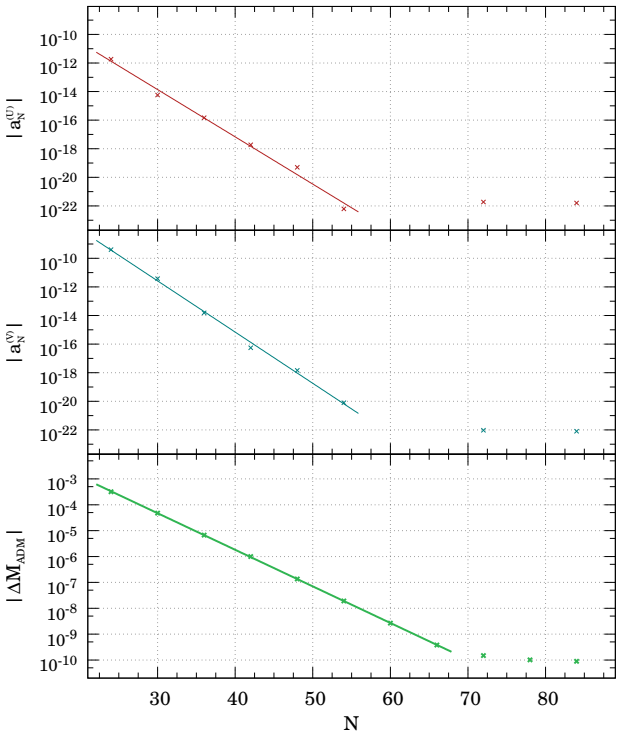

Figure 2.14: Convergence Analysis in the Cauchy Evolution. The upper and middle plots show the truncation error for the variables U and V, $|a_N^{(U)}|$ and $|a_N^{(V)}|$ respectively, as a function of the number of collocation points per domain, N. From all the truncation errors, one at each domain, we take the one where the variables reach their maximum values. The linear fitting with the logarithmic scale in the vertical axis shows the expected exponential convergence (see Sec. 2.5.1). The plot in the bottom shows that deviations in the ADM mass during the evolution also decrease exponentially with the number of collocation points per domain until saturation due to round-off error.

2.5 Test for Code Validation

In this section we show the performance of the different pieces of the numerical code that we have developed to implement the Cauchy-characteristic scheme described in the previous sections to study gravitational collapse in spherically symmetric AAdS spacetimes.

2.5.1 Convergence Analysis for the Cauchy Evolution

The Cauchy evolution uses a PSC discretization method for the radial direction with multiple domains. At each domain we use a Chebyshev-Lobatto grid with

a linear mapping to the physical radial space, see Sec. 1.3.2 for details. The PSC method provides two representations for each variable, the spectral representation typical of general spectral methods, and the *physical* representation where the values of our variables at the collocation points are the unknowns to be found numerically. As we have mentioned before, the truncation error is estimated by using the absolute value of the last spectral coefficient, $|a_N|$. For smooth functions, the convergence rate of the Chebyshev series is exponential. We check convergence for our Cauchy-evolution code by performing a series of runs with the same number of domains ($D = 50$), uniformly distributed in the radial coordinate x, and with no refinement. We set the same initial conditions for all of them, from the family of configurations in Eq. (2.113), and evolve them it for a fixed interval of time ($t_f \approx 2$, i.e. after a bounce off the AdS boundary). Then, we look at the last spectral coefficients for the characteristic variables U and V. Here, we only show results from the domain where these variables present more features, which is in principle the most challenging one from the numerical point of view, and we have checked that we obtain equivalent results for the other domains. In Fig. 2.14, at the upper and middle panels, we show the spectral convergence for these two variables in a logarithmic plot of the absolute value of the last spectral coefficient versus the number of collocation points. As we can see, the linear scaling in the logarithmic plot stops at some point, followed by an almost flat profile, indicating that we have reached the round-off error of the computer and hence we cannot expect to improve the truncation error any further. In the bottom panel of Fig. 2.14, we show the variations in the ADM mass, $M_{\rm ADM}$, with respect to its initial value, $M_{\rm ADM}(t_0)$, due to numerical inaccuracies during the Cauchy evolution (in an ideal situation this quantity should vanish for all times). Actually, what we show in this figure is the normalised quantity:

$$\Delta M_{\rm ADM}(t) = \frac{|M_{\rm ADM}(t) - M_{\rm ADM}(t_0)|}{M_{\rm ADM}(t_0)} \,. \tag{2.108}$$

In Fig. 2.14 we see exponential convergence of the deviations from the ADM mass ($\Delta M_{\rm ADM}(t_f)$, with $t_0 = 0$) that saturate at a value around 10^{-10} for our particular test runs.

2.5.2 Convergence Analysis for the Characteristic Evolution

In the characteristic scheme, we have a non-uniform discretization in the radial coordinate r in the initial grid, and it turns out that the evolution of the r-coordinate of the grid points [according to the ingoing null geodesics in Eq. (2.73)] makes our grid even more unequally spaced. Despite of this, the resolution increases with the number of grid points and we can study how the results converge as we increase this number. To that end, we run simulations with different initial number of grid points (the number of grid points changes along the evolution because we lose points through the origin) but with the same initial scalar field profile, see Eq. (2.117). These

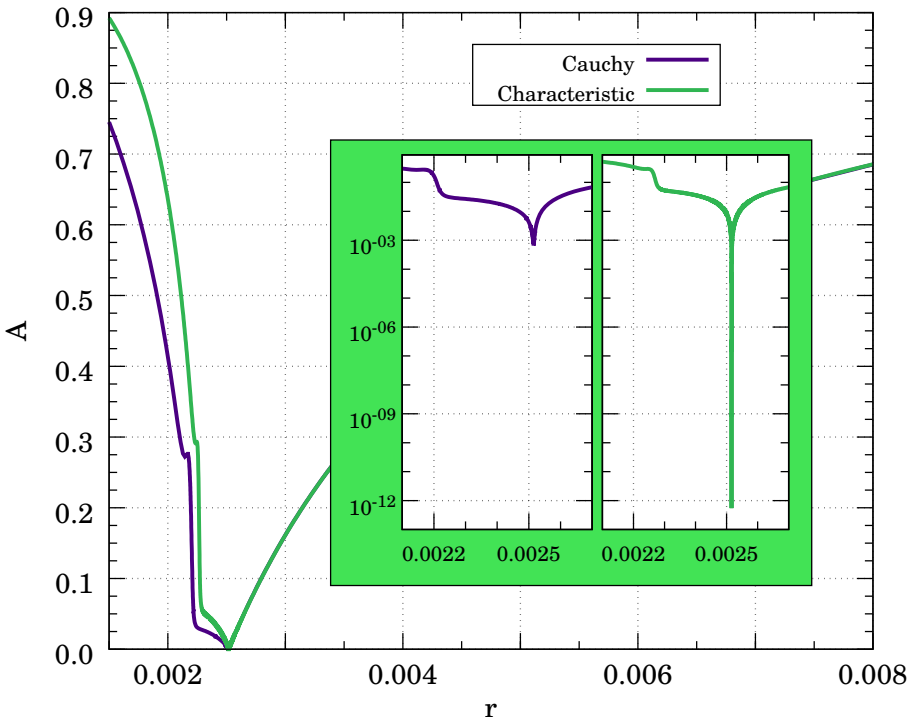

Figure 2.15: Final Snapshot of the Cauchy and Characteristic Evolution Methods. We show a snapshot of the function A just before collapse using both methods. The differences are due to the fact that in the Cauchy evolution A is plotted from a $t = const.$ slice while in the characteristic one comes from a $u = const.$ slice. The plots coincide around $r = r_{\rm AH}$. The zoom-in plot shows, by using a logarithmic scale, how close to AH formation ($A \to 0$) we can get with each evolution scheme.

---

initial conditions eventually form an AH and the point of the evolution that we take to analyse the convergence is just before the formation of the AH, when $A \approx 10^{-8}$ [A is estimated via Eq. (2.91)]. That is, we monitor how the location of AH formation changes with the number of grid points, N. We use the following indicator:

$$p = \log_2 \left(\frac{|r_{\rm AH}^{N/4} - r_{\rm AH}^{N/2}|}{|r_{\rm AH}^{N/2} - r_{\rm AH}^{N}|} \right) . \tag{2.109}$$

For $N = 120000$ we obtain $p \approx 3.0034$. This value means that the convergence of our code is third order, in agreement with the convergence rate of the Simpson integration rule that we use.

2.5.3 Comparison between the Cauchy and Characteristic Evolutions

The main reason for implementing a hybrid Cauchy-characteristic evolution scheme is to bring together the best of these two methods of evolution in order to tackle interesting questions about gravitational collapse in AAdS spacetimes. That is, taking into account that the Cauchy evolution based on the PSC method allows us to follow the possible different bounces of the matter fields (a scalar field in our case) off the AdS boundary with high precision, whereas the characteristic evolution allows us to get very close to the point of formation of an AH. Then, although the two evolution schemes are used in different stages of the evolution, it is interesting to see how they compare when they are applied to the final moments of the collapse, when an AH forms. This comparison is also a justification for the introduction of our hybrid scheme, which on top of the two evolution methods requires a non-trivial transition between them. Then, we have evolved the same scalar field configurations with both evolution schemes to get as close as possible to the point of AH formation, which is monitored using the metric function A. In the characteristic scheme the function A can be computed using Eq. (2.91). We show the results of this comparison in Fig. 2.15, where we include a zoom-in plot of the relevant region for AH formation. In the left zoom-in plot, we show the metric function A for a Cauchy evolution until the numerical code is not stable anymore without adding more domains, and such that if we keep adding resolution the evolution would essentially freeze because of the tiny time step allowed by the CFL condition. For the right zoom-in plot, we initiated the evolution also with the Cauchy evolution scheme (in order to guarantee that we are comparing the same physical configuration) and then changed to the characteristic scheme until the point where the numerical noise becomes significant or the evolution effectively stops due to a too small Δu step. As we can see, with the characteristic evolution we can get many orders of magnitude closer to the AH formation than with the Cauchy scheme, as measured in terms of the metric function A. This clearly illustrates the power of our hybrid scheme to study the collapse near AH formation.

2.5.4 Ingoing Null Geodesics

In order to understand better the magnitude of the numerical challenge posed by the study of gravitational collapse in AAdS spacetimes it is interesting to analyse the ingoing null geodesics in the characteristic evolution of AAdS spacetimes and compare them with the ingoing null geodesics in asymptotically flat spacetimes. To begin with, let us look at the difference between the ingoing null geodesics in AdS spacetime, Eq. (2.61), and in Minkowski spacetime, in the equivalent coordinate system where the metric has the same form as in Eq. (2.61). The equation for the ingoing null geodesics has also the same form in both cases, i.e. Eq. (2.73), but the

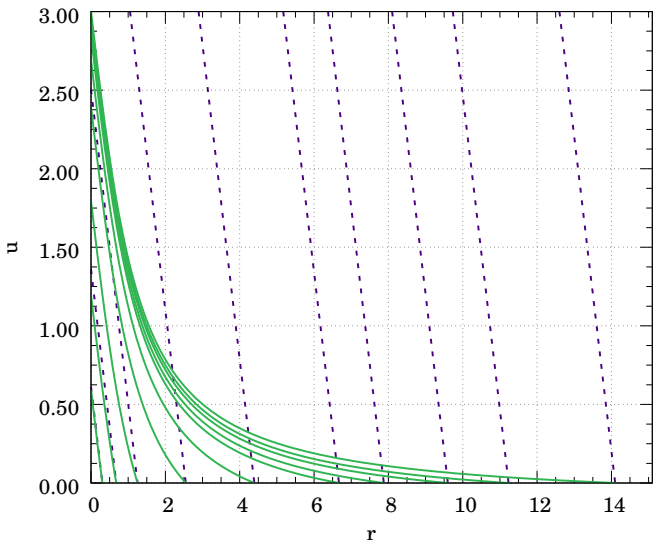

Figure 2.16: Comparison of Ingoing Null Geodesics in Minkowski (dashed purple lines) and AdS (green continuous lines) spacetimes. We see the strong effect that the cosmological constant term has in the geodesics. In AdS spacetime they reach the region near the origin much faster than in Minkowski, as measured by the time u.

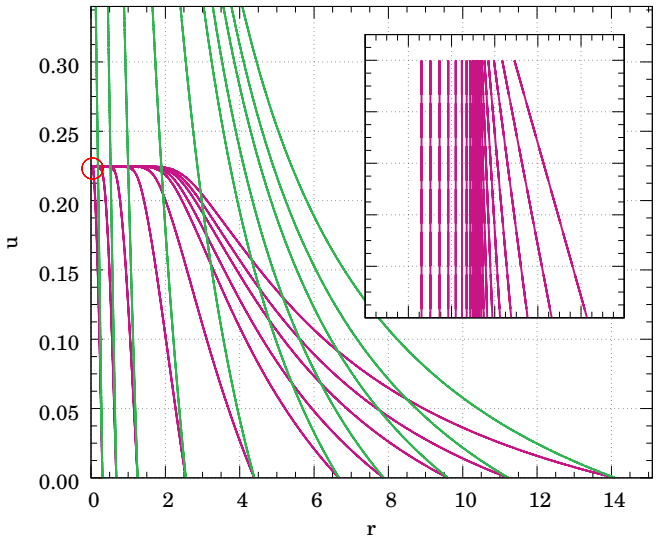

Figure 2.17: Comparison between Ingoing Null Geodesics in Pure AdS Spacetime (green colour) and in an AAdS Spacetime Describing Gravitational Collapse of a Scalar Field (fuchsia colour). In the second, the geodesics focus around the location of AH formation. The small plot is a zoom of the region inside the red circle where it can be seen how the geodesics behave around r_{AH}. This size of the zoom-in plot is $\Delta r \simeq 10^{-4}$ around $r \simeq 0.03952$ and $\Delta u \simeq 10^{-13}$ around $u \simeq 0.224673828858275$.

form of the metric function $\bar{g}$ is different. In AdS spacetime we have:

$$\bar{g}_{\rm AdS}(r) = 1 + r^2/\ell^2, \tag{2.110}$$

whereas is Minkowski we have:

$$\bar{g}_{\rm Mink}(r) = 1. \tag{2.111}$$

Therefore, by solving the ingoing null geodesic equation, Eq. (2.73), we get the following expressions for the ingoing null geodesics:

$$\begin{aligned} u_{\rm Mink}(r) &= 2\left(r_0 - r\right) , \\ u_{\rm AdS}(r) &= 2\left(\arctan(r_0) - \arctan(r)\right) . \end{aligned} \tag{2.112}$$

These geodesics have been plotted in Fig. 2.16. This illustrates what can happen with our characteristic grid in AAdS evolutions in comparison with the asymptotically flat case. As shown in Fig. 2.16, the grid points of an initial null slice ($u = 0$) move towards the origin much faster in AdS spacetime than in Minkowski spacetime. The conclusion we extract from this expansion for our simulations is that we must be very careful in choosing the initial null slice, in particular its size, because the grid points in AdS travel very fast towards the region near the origin, which means that our grid shrinks very fast and we may miss the interesting phenomena, in particular the formation of an AH.

On the other hand, in Fig. 2.17 we show the comparison between ingoing null geodesics in AdS spacetime and the ones of an AAdS spacetime where the scalar field collapses forming an AH. We compute these geodesics numerically as the solution of Eq. (2.73). As soon as the geodesics approach the spacetime point in the (u, r)-plane where the AH forms, all the ingoing null geodesics with $r > r_{AH}$ focus at that point as it can be seen in the zoom-in area of this figure, while those with $r < r_{AH}$ follow a different path.

2.6 Results from the Numerical Evolution

The landscape of the gravitational collapse in AdS spacetimes that emerged after the pioneer work of Ref. [5] can be summarised by saying that initially-compact scalar field configurations will sooner or later form an AH. The time required to form the AH depends on how many round trips to the AdS boundary are needed for the AdS *turbulent instability* to convert long-wavelength modes into short-wavelength ones so that the scalar field profile gets compressed enough to form a BH. This is illustrated in Fig. 2.18 where we show the AH radius, r_{AH}, obtained by evolving a number of initial configurations from the family of Eq. (2.113) with our Cauchy-characteristic evolution scheme. This three-dimensional plot has been obtained by

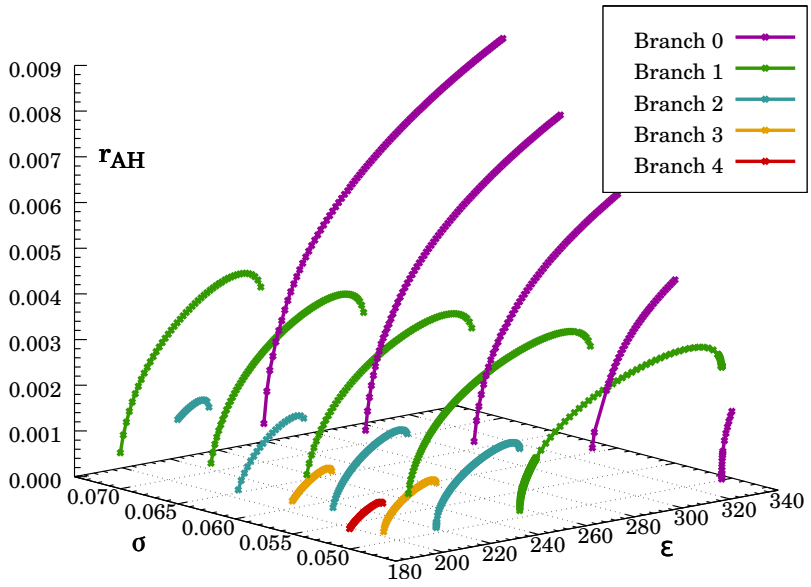

Figure 2.18: AH Location in a 2-parameter Phase Space. We show the radial location of the AH formed from initial configurations belonging to the family in Eq. (2.113) for different values of the amplitude, ε, and the width, σ.

varying both the amplitude, ε, and the width, σ, of the initial configurations. It shows the different branches that appear and that represent configurations that have bounced off the AdS boundary a fixed number of times (indicated by the colour and branch number in Fig. 2.18) before collapsing and forming an AH. The branches are clearly seen in the direction of the amplitude ε, where we have a high number of points, but it can be seen that it also happens in the direction of the width σ. The same should happen if we look at any direction in the plane (ε, σ). This is evident since the critical collapse is independent of the family of initial conditions that we take.

In what follows we describe new results regarding the critical collapse, that is, analysing the configurations in Fig. 2.18 near the plane $r_{AH} = 0$, and we also describe the existence of a mass gap between branches and a new universal power-law scaling for subcritical configurations.

2.6.1 Critical Phenomena in AAdS Gravitational Collapse

In Ref. [5] it was mentioned that at the critical points separating the branches, the supercritical configurations form an AH with mass going to zero with the same scaling as in the case of asymptotically flat spacetimes [1], that is: $r_{\rm AH} \sim (p - p_n)^\gamma$

with $\gamma \simeq 0.374$. In this section we give numerical confirmation for this claim for the six first branches.

We use the following family of initial configurations:

$$\begin{aligned} U(t_o, x) &= \varepsilon \exp\left(-\frac{4\tan^2 x}{\pi^2 \sigma^2}\right), \\ V(t_o, x) &= -U(t_o, x)\,, \end{aligned} \tag{2.113}$$

that represents a profile centred around the origin at the initial time, and characterised by the amplitude ε and width σ. This particular choice, and any that fulfils the condition $V(t_o, x) = -U(t_o, x)$, directly implies: $(\partial_x \phi)(t_o, x) = 0$.

As we explained in Sec. 2.1, the critical attractor that exists at $p = p_c$ can be observed in the scaling of the apparent horizon mass of the supercritical configurations and also in the behaviour of the maximum of the scalar of curvature at the origin of the subcritical configurations. In AdS, since the subcritical configurations will collapse after a bounce off the boundary, we need to monitor the scalar of curvature before this last bounce. Having this in mind, we remember that the scalar of curvature scales as:

$$R_{\max}|_{x=0} \sim (p_n - p)^{-2\gamma}\,, \tag{2.114}$$

where p_n is the nth critical point and γ the critical exponent. This scaling have a finer structure:

$$\ln R_{\max}|_{x=0} = (-2\gamma)\, \ln(p_n - p) + b_0 + F(\ln(p_n - p))\,, \tag{2.115}$$

where F is a periodic function with period equal to $\Delta/2\gamma$. In terms of the Cauchy-evolution variables, the scalar of curvature at the origin can be computed using the following expression:

$$R|_{x=0} = -\frac{12}{\ell^2} - \frac{1}{2\ell^2}\,(V - U)^2\,. \tag{2.116}$$

We have carried out a series of Cauchy evolutions of initial configurations from the family in Eq. (2.113) with fixed width, $\sigma = 0.05$, and amplitudes chosen in such a way that the configurations are subcritical with respect to any of the first six critical points. The results of these simulations are shown in the left plot of Fig. 2.19 with the corresponding fittings. The values of the critical amplitudes, ε_n, the critical exponents, γ, and the echoing periods, Δ, are presented in Table 2.1. We can see that the values obtained for γ and Δ are consistent with the known values for the collapse of massless scalar fields in asymptotically flat spacetimes.

We have already mentioned that the characteristic evolution method, as we have formulated it in Sec. 2.3.2, cannot be used to follow the full evolution of the scalar field because the characteristic grid shrinks with time and hence we cannot track

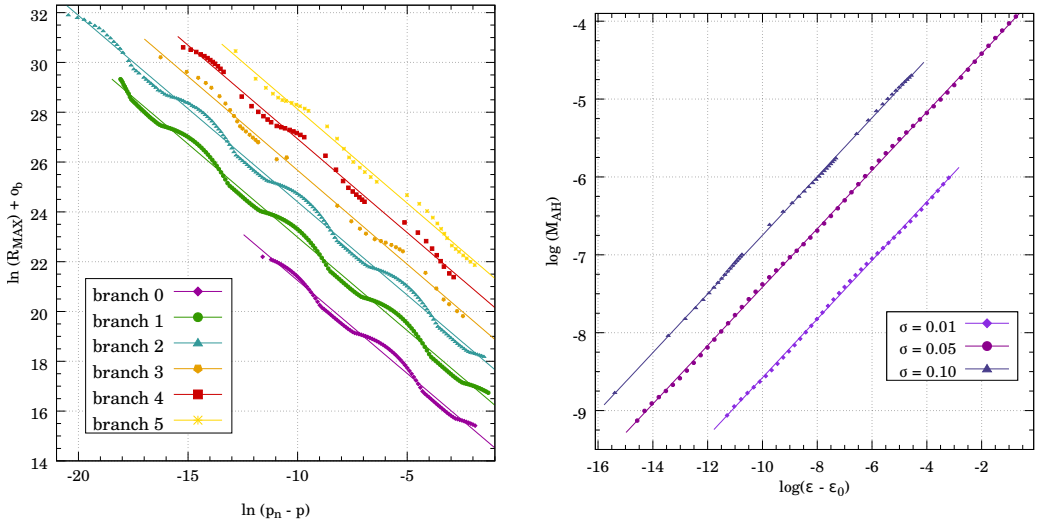

Figure 2.19: Critical Exponents for Supercritical Configurations.
Left Plot: Critical Exponents for Fixed Width ($\sigma = 0.05$). Scaling of the scalar of curvature, R, for subcritical configuration near the critical point for different branches, from the branch of direct collapse ($b = 0$, bottom) to the branch with five bounces ($b = 5$, top). An offset o_b has been added to the y axis to make the plot more clear. The values of the offset are: $o_b = -2, -1, 0, +1, +2, +3$, starting from $b = 0$. The results from the fittings are given in Table 2.1.
Right Plot: Critical Exponents for the Zero Branch Using the Characteristic Method. We show the results for the AH mass versus initial amplitude for three different families of initial configurations with fixed width [see Eq. (2.117)] of the branch 0 (direct collapse). The values of the critical amplitudes, critical exponent and echoing period are given in Table 2.1.

bounces of the scalar field off the AdS boundary. However, we can in principle use the characteristic evolution for the particular cases in which the scalar field collapses directly, or in other words, we can in principle study the zero branch with the characteristic evolution. Actually, this was already done in Ref. [35] using a double-null characteristic scheme. Here, we repeat this analysis to confirm the same result and, at the same time, to test further our characteristic evolution method. To that end, we have to prescribe initial data on a null slice $u = const.$ for the scalar field variable h. We choose the following family of initial conditions:

$$\phi(r) = \bar{h}(r) = \varepsilon \, \frac{r^2}{\ell^2} \exp\left(-\frac{(r - r_0)^2}{\ell^2 \, \sigma^2} \right) , \tag{2.117}$$

which has three parameters: The amplitude ε, the width σ, and the centre of the profile r_0, which we always fix to the value: $r_0 = 0.1\,\ell$. We have performed a series of characteristic evolutions varying the amplitude ε for three (fixed) values of the width $\sigma = 0.01, 0.05$ and 0.10. We compute the critical exponent γ and the echoing

Supercritical exponents fixed width			
Branch	Critical Value (ε_n)	Critical Exponent (γ)	Echoing (Δ)
$n=0$	$335.572231(5)$	0.374 ± 0.006	3.33 ± 0.15
$n=1$	$251.09427729(1)$	0.3746 ± 0.0008	3.45 ± 0.02
$n=2$	$216.208077165(1)$	0.3743 ± 0.0004	3.45 ± 0.02
$n=3$	$193.9755275(1)$	0.377 ± 0.007	3.43 ± 0.04
$n=4$	$178.070915(1)$	0.376 ± 0.007	3.42 ± 0.06
$n=5$	$165.946674(4)$	0.377 ± 0.010	3.46 ± 0.10
Exponents Zero Branch - Characteristic			
Width (σ)	Critical Value (ε_0)	Critical Exponent (γ)	Echoing (Δ)
0.01	$7.828039(2)$	0.376 ± 0.006	3.2 ± 0.4
0.05	$25.907772996(3)$	0.3748 ± 0.0004	3.33 ± 0.10
0.10	$23.8595911(1)$	0.375 ± 0.005	3.45 ± 0.10

Table 2.1: Critical Exponents for Supercritical Configurations.
Upper Table: Critical Exponents for Fixed Width ($\sigma = 0.05$). Fitting values of the critical exponents corresponding to the critical parameters for the six first branches (see Fig. 2.19). The number in parenthesis denotes the error to be applied to the last digit of the computed value.
Bottom Table: Critical Exponents for Branch Zero Using the Characteristic Method. Fitting values of the critical exponents corresponding to the critical parameters for the zero branch using only the characteristic method (see Fig. 2.19).

period Δ from the AH mass, which in AAdS spacetimes with the coordinates of Eq. ((2.61)) is given by:

$$M_{\rm AH} = \frac{r_{\rm AH}}{2}\left(1+\frac{r_{\rm AH}^2}{\ell^2}\right), \tag{2.118}$$

where the values of this mass that we quote in this chapter are in units of ℓ. Again we fit our characteristic only simulations to the formula:

$$\ln M_{\rm AH} = \gamma\, \ln(p-p_n) + b_0 + F(\ln(p-p_n))\,, \tag{2.119}$$

where this time we use the mass scaling and F is again a periodic function with period $\Delta/2\gamma$. The results obtained from these simulations are shown in Fig. 2.19 with the fittings to Eq. (2.119). The critical values of the amplitude, ε_0, the critical exponent γ, and the echoing period Δ are given in Table 2.1. Again, the results are consistent with the predictions for the asymptotically flat case.

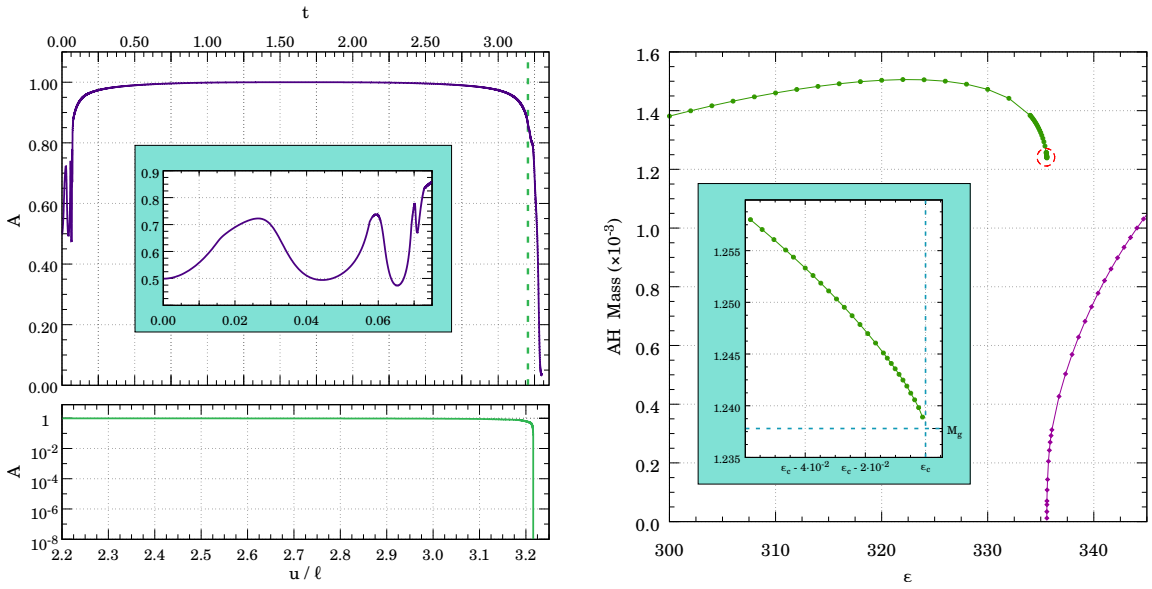

Figure 2.20: Mass Gap.
Left Plot: Evolution of A in the Case of AH Formation after One Bounce. The upper panel shows the Cauchy evolution. The vertical dashed line indicates the last time used for the transition to the characteristic evolution which A evolution is showed in the lower panel. The zoom area represents the first attempt of collapse.
Right Plot: Interface between the Zero and One Bounce Branches. The zoomed area shows the behaviour as the critical point is approached from the one bounce branch.

2.6.2 Power-law Behaviour near the Mass Gaps

We are going to focus now on near subcritical configurations for the one bounce branch. In the left plot of Fig. 2.20 we show the evolution of the metric function A for one such configuration. Initially, the evolution is close to collapse (and to the critical solution) and exhibits oscillations typical of type II critical phenomena. This moment of the evolution is when we can find the data to study the supercritical behaviour of Eq. (2.115). After the trip to the AdS boundary and back, the scalar field collapses straightaway. The difficulty of this problem lies in the resolution requirements that the subcritical configurations pose on our simulations since we have to evolve the sharp features originated during the quasi-collapse stage to the AdS boundary and back. From the point of view of computational cost, the most challenging part is this last bounce and as we get closer to the critical point gets worse. But in order to have a good precision in the values of the mass gap and power-law exponent, we need to perform as many of them as we can in order to locate properly the critical point.

In Fig 2.18, we showed the AH mass in terms of the initial scalar field amplitude ε and the width σ, in which the collapse can happen either directly or after a few

bounces depending on the colour of the points there represented. Taking a slice of constant width and focusing around the first critical point in the interface between the branch of direct collapse and the branch of collapse after one bounce as in the right plot of Fig. 2.20, we find that BHs formed after one bounce have a minimum AH mass, M_g, and that the AH mass follows a power law of the type:

$$M_{\rm AH} - M_g^{n+1} \propto (p_n - p)^{\xi}\,, \tag{2.120}$$

where p_n denotes the critical value of the initial-data parameter p for the n-th branch; M_g^{n+1} is the mass of the $(n+1)$th gap, between the branches n and $n+1$, corresponding to the minimum mass of the AH formed by subcritical configurations; and ξ is the power-law exponent. An argument about why there are no points with arbitrarily small mass in this side of the branch is that the subcritical configurations have to travel to the AdS boundary and come back, suffering a *finite compression* due to the non-linearity (a key ingredient for the *turbulent* instability), that makes them to form BHs with an initial minimum mass.

We have computed the exponent of the power law, ξ, in several ways. First of all, in a series of simulations for the one and two bounce branches for the family of initial configurations of Eq. (2.113) with fixed widths $\sigma = 0.05,\, 0.06$, and 0.07 and also for the three bounce branch for $\sigma = 0.05$. We complete these results in a series of simulations for the one bounce branch at fixed initial scalar field amplitude $\varepsilon = 250$ that in terms of the critical collapse can be consider a different one-parameter family and also with another family of configurations described as:

$$\begin{aligned} U(t_o, x) &= \varepsilon \cosh^{-1}\left(\frac{\tan(x) - \tan(x_0)}{\sigma}\right)\,, \\ V(t_o, x) &= -U(t_o, x)\,, \end{aligned} \tag{2.121}$$

that is described by three parameters, an amplitude ε, a width σ, and the position at which the scalar field profile is centred, x_0. It turns out that the simulations for the configurations within the parameter region of interest, those that lead to subcritical scalar field collapse, are numerically more challenging than in the case of the initial conditions from the family in Eq. (2.113). The reason for this is that the energy distribution in the new family of configurations is not as compact as in the old one. This has already been illustrated in the evolutions tracking the *centre of mass* of the scalar field profile shown in Fig. 2.11. For our simulations we set $x_0 = 1.2$ and $\sigma = 0.2$ for having the profile located near the boundary and then having a completely different from other that is origin-centred. All of this data is shown the Fig. 2.21 and the corresponding fitting results in Table 2.2.

The reason for choosing this data is because we want to study whether the new scaling exponent ξ is universal both for different one-parameter families and also for all the mass gaps. The fitting data is shown in Table 2.2. The key aspect to get a good estimation for ξ is to get as closer as we can to the critical point p_c. In this

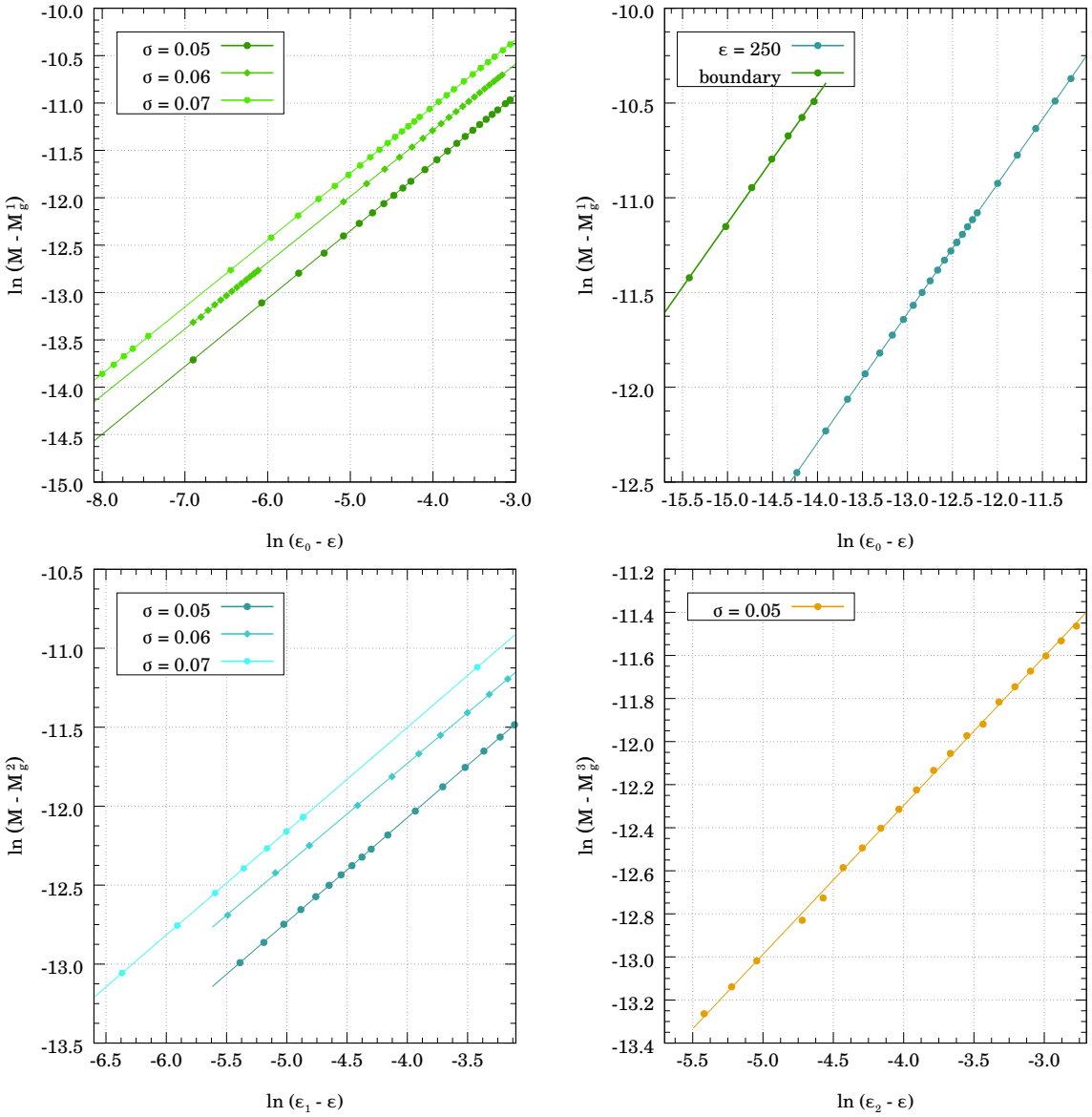

Figure 2.21: Mass Gap Fitting Data. We show all the data of the collapse for subcritical configurations fitting it according to Eq. (2.120). The upper left plot show the data of the gap 1 for fixed width initial data of Eq. (2.113). The upper right shows fixed amplitude for the previous initial data and also the family of Eq. (2.121). The bottom left shows the data of gap 2 and bottom right of gap 3, both of fixed width initial data of Eq. (2.113).

Parameters	Critical Value (p_n)	Mass Gap (M_g^{n+1})	Exponent (ξ)
Gap 1			
$\sigma = 0.05$	$335.572(2)$	$1.238(1) \cdot 10^{-3}$	0.71 ± 0.02
$\sigma = 0.06$	$279.642(1)$	$1.484(1) \cdot 10^{-3}$	0.70 ± 0.01
$\sigma = 0.07$	$239.692(1)$	$1.732(1) \cdot 10^{-3}$	0.70 ± 0.02
$\varepsilon = 250$	$0.0671138(2)$	$1.660(2) \cdot 10^{-3}$	0.68 ± 0.04
$\sigma = 0.2$ $x_0 = 1.2$	$1.093435(1)$	$7.2954(8) \cdot 10^{-3}$	0.68 ± 0.07
Gap 2			
$\sigma = 0.05$	$251.10(1)$	$7.6(1) \cdot 10^{-4}$	0.65 ± 0.07
$\sigma = 0.06$	$209.25(1)$	$9.0(1) \cdot 10^{-4}$	0.64 ± 0.10
$\sigma = 0.07$	$179.36(1)$	$1.05(2) \cdot 10^{-3}$	0.67 ± 0.07
Gap 3			
$\sigma = 0.05$	$216.203(9)$	$5.44(2) \cdot 10^{-4}$	0.69 ± 0.04

Table 2.2: Critical Exponents of the Mass Gap Power Law. Fitting values corresponding to the subcritical data of the mass gap. We include data of first three critical points for different initial conditions (Eq. (2.113) and Eq. (2.121).). The fitting data correspond with the Fig. 2.21.

sense the best resolution we have is in the first gap of the initial configuration of the family of Eq. (2.113). There we obtain a value of $\xi \simeq 0.70$ and all the rest of the values computed are compatible with this value with lower numerical precision.

From these results we conjecture that the scaling law of the subcritical configurations is universal with an exponent $\xi \simeq 0.70$ not only for different families but also for the different branches. This new feature of the critical collapse in AdS was published first in Ref. [7] and later confirmed with more results in Ref. [8]

2.7 Conclusions

The collapse of a massless scalar field in a spherically symmetric AAdS spacetime shows a much richer phenomenology than the analogous problem in asymptotically flat spacetimes as it was realised for the first time in Ref. [5] and is illustrated by our Fig. 2.18. Both the long-term evolution and the dynamics of gravitational collapse present distinctive features that are not yet fully understood. In this work we have focused on the dynamics near collapse, when an AH is formed. To study this question we need to resort to numerical methods, taking into account that we are dealing with a problem that represents an important challenge for the design

and performance of a numerical code that solves the PDEs describing the system, despite the fact that we are dealing with a 1+1 problem (spherical symmetry). The main reason for this lies behind the causal structure of global AdS, where light-like signals can reach the AdS boundary in a finite time. As a consequence, an scalar field configurations that fails to form an AH in a first attempt will travel to the AdS boundary in a finite time, bounce and travel back towards the origin, where it will have a second chance to form an AH. This process will be repeated until, after certain number of bounces, the scalar field will collapse forming an AH. This is not the whole story as we have evidence of the existence of stable scalar field configurations, which makes the whole picture to be not yet completely well understood. The near subcritical configurations are very challenging since they are very close to collapse, which induces large gradients in the field variables that we have to propagate to the AdS boundary and back. In this sense, AAdS spacetimes constitute an excellent arena for the development of new numerical relativity methods and tools.

In this chapter we have presented a new numerical scheme to study these situations which, in essence, is a hybrid Cauchy-characteristic evolution scheme. The Cauchy evolution uses a multidomain PSC method for the spatial discretization and the characteristic evolution follows the ingoing null geodesics, which allows us to get much closer to the point of AH formation than with the Cauchy evolution. An additional crucial part of this method is the transition between the two schemes. We have described in detail all the analytic and numerical ingredients of this Cauchy-characteristic evolution scheme. In doing so, we have also analysed the differences between evolution in AAdS and asymptotically flat spacetimes, pointing out how the effect of the cosmological constant makes our simulations more challenging. We have also shown the convergence properties of the different parts of the scheme and how we implement AMR techniques for the Cauchy-evolution sector. Given that the scalar field configurations that we have considered are localised in the radial direction, in the sense that the energy density is concentrated within a single radial interval, we have studied how two definitions of centre of mass can track the evolution of the field and how by using them we can also have a sense of how compact a certain scalar field configuration is.

With this numerical scheme we have studied the subcritical scalar field configurations near the different branches that appear depending on the number of times that the field bounced off the AdS boundary. We found evidence that this configurations follow the power law:

$$M_{\rm AH} - M_g^{n+1} \propto (p_n - p)^{\xi},$$

with the mass gap between branches (separated by the location of the critical point, p_n) given by M_g^{n+1} and the exponent ξ is conjectured to be universal, independent of the initial data and also the same for all the mass gaps/branches. The numerical support provided comes from the first three mass gaps using the initial conditions

of Eq. (2.113) varying both the amplitude and the width and also for the gap one with the initial data of Eq. (2.121). All these results support our conjecture for the power law at the mass gaps and the universal character of the exponent up to our numerical accuracy which, in all cases, has a value consistent with:

$$\xi \approx 0.70.$$

It would be interesting to have analytical support for this numerical result but, at a first glance, it appears to be a difficult enterprise. The reason is that the subcritical solutions that follow this power law correspond to initial conditions that are very close to those that define the associated critical solution, but they are separated by a full round trip to the AdS boundary. Then, any analytical study of this power law should consider the details of the non-linear dynamics during the round trip together with the influence of the AdS boundary, which in our view seems even more complicated than the analytical study of the critical solution itself, and hence beyond the scope of our work.

Another open question is the precise role of the AdS boundary. In Ref. [64], the introduction of an artificial boundary at a finite distance from the origin in asymptotically flat spacetime leads to an scaling law for the subcritical solutions with the same exponent γ as in the supercritical case. The comparison between their results and ours indicates that there is a difference between global AdS and the system with an artificial boundary in asymptotically flat spacetimes. In this sense it is interesting to note that our value for the exponent is quite close to $2\,\gamma \approx 0.74$. Apart from this, the global AdS and the asymptotically flat case with an artificial boundary do not show differences neither in the structure of the AH phase space (see Fig. 2.18) nor in the scaling for supercritical configurations.

On the other hand, we have also obtained the critical exponents associated with the multiple critical points that appear in the case of AAdS spacetimes. By tracking supercritical configurations using only the Cauchy evolution we have been able to find the critical points associated with the branches 0 to 5. We have confirmed the expected result [5] that at AH formation the presence of the negative cosmological constant is irrelevant. Indeed, the critical exponents and echoing periods that we have found are consistent with the values of the asymptotically flat case.

Bibliography

[1] Matthew W. Choptuik. Universality and scaling in gravitational collapse of a massless scalar field. *Phys. Rev. Lett.*, 70:9–12, 1993.

[2] Demetrios Christodoulou. The Problem of a Selfgravitating Scalar Field. *Commun. Math. Phys.*, 105:337–361, 1986.

[3] Juan Maldacena. The Large N limit of superconformal field theories and supergravity. *Int. J. Theor. Phys.*, 38:1113–1133, 1997.

[4] Edward Witten. Anti-de Sitter space and holography. *Adv. Theor. Math. Phys.*, 2:253–291, 1998.

[5] Piotr Bizoń and Andrzej Rostworowski. On weakly turbulent instability of Anti-de Sitter space. *Phys. Rev. Lett.*, 107:031102, 2011.

[6] Claudio Canuto, M Yousuff Hussaini, Alfio Quarteroni, and Thomas A. Zang. *Spectral methods in Fluid Dynamics*. Springer-Verlag, 1988.

[7] Daniel Santos-Oliván and Carlos F. Sopuerta. New Features of Gravitational Collapse in Anti-de Sitter Spacetimes. *Phys. Rev. Lett.*, 116(4):041101, 2016.

[8] Daniel Santos-Oliván and Carlos F. Sopuerta. Moving closer to the collapse of a massless scalar field in spherically symmetric anti–de Sitter spacetimes. *Phys. Rev.*, D93(10):104002, 2016.

[9] Stephen W. Hawking. Black holes in general relativity. *Comm. Math. Phys.*, 25(2):152–166, 1972.

[10] Demetrios Christodoulou. Global Existence of Generalized Solutions of the Spherically Symmetric Einstein Scalar Equations in the Large. *Commun. Math. Phys.*, 106:587–621, 1986.

[11] Demetrios Christodoulou. The Structure and Uniqueness of Generalized Solutions of the Spherically Symmetric Einstein Scalar Equations. *Commun. Math. Phys.*, 109:591–611, 1987.

[12] Demetrios Christodoulou. A Mathematical Theory of Gravitational Collapse. *Commun. Math. Phys.*, 109:613–647, 1987.

[13] Demetrios Christodoulou. The formation of black holes and singularities in spherically symmetric gravitational collapse. *Commun. Pure Appl. Math.*, 44(3):339–373, 1991.

[14] Demetrios Christodoulou and Sergiu Klainerman. *The Global Nonlinear Stability of the Minkowski Space (PMS-41)*. Princeton University Press, Princeton, 1994.

[15] Matthew W. Choptuik. *A study of numerical techniques for radiative problems in general relativity*. PhD thesis, University of British Columbia, Jul 1986.

[16] Dalia S. Goldwirth and Tsvi Piran. Gravitational Collapse of Massless Scalar Field and Cosmic Censorship. *Phys. Rev.*, D36:3575, 1987.

[17] Subrahmanyan Chandrasekhar. The maximum mass of ideal white dwarfs. *Astrophys. J.*, 74:81–82, 1931.

[18] David Garfinkle. Choptuik scaling in null coordinates. *Phys. Rev.*, D51:5558–5561, 1995.

[19] Carsten Gundlach. Understanding critical collapse of a scalar field. *Phys. Rev.*, D55:695–713, 1997.

[20] Shahar Hod and Tsvi Piran. Fine structure of Choptuik's mass scaling relation. *Phys. Rev.*, D55:440–442, 1997.

[21] Richard C. Tolman. Static solutions of Einstein's field equations for spheres of fluid. *Phys. Rev.*, 55:364–373, 1939.

[22] J. Robert Oppenheimer and George M. Volkoff. On Massive neutron cores. *Phys. Rev.*, 55:374–381, 1939.

[23] David Garfinkle and G. Comer Duncan. Scaling of curvature in subcritical gravitational collapse. *Phys. Rev.*, D58:064024, 1998.

[24] Michael Purrer, Sascha Husa, and Peter C. Aichelburg. News from critical collapse: Bondi mass, tails and quasinormal modes. *Phys. Rev.*, D71:104005, 2005.

[25] Carsten Gundlach and Jose M. Martin-Garcia. Critical phenomena in gravitational collapse. *Living Rev. Rel.*, 10:5, 2007.

[26] Jose M. Martin-Garcia and Carsten Gundlach. Global structure of Choptuik's critical solution in scalar field collapse. *Phys. Rev.*, D68:024011, 2003.

[27] Carsten Gundlach. The Choptuik space-time as an eigenvalue problem. *Phys. Rev. Lett.*, 75:3214–3217, 1995.

[28] Matthew W. Choptuik, Tadeusz Chmaj, and Piotr Bizon. Critical behavior in gravitational collapse of a Yang-Mills field. *Phys. Rev. Lett.*, 77:424–427, 1996.

[29] Patrick R. Brady, Chris M. Chambers, and Sergio M.C.V. Goncalves. Phases of massive scalar field collapse. *Phys. Rev.*, D56:6057–6061, 1997.

[30] Hirotada Okawa, Jorge C. Lopes, and Vitor Cardoso. Collapse of massive fields in Anti-de Sitter spacetime. 2015.

[31] Jason Bland, Brent Preston, M. Becker, Gabor Kunstatter, and Viqar Husain. Dimension dependence of the critical exponent in spherically symmetric gravitational collapse. *Class. Quant. Grav.*, 22:5355–5364, 2005.

[32] Jason Bland and Gabor Kunstatter. The 5-D Choptuik critical exponent and holography. *Phys. Rev.*, D75:101501, 2007.

[33] Frans Pretorius and Matthew W. Choptuik. Gravitational collapse in (2+1)-dimensional AdS space-time. *Phys. Rev.*, D62:124012, 2000.

[34] Viqar Husain and Michel Olivier. Scalar field collapse in three-dimensional AdS space-time. *Class. Quant. Grav.*, 18:L1–L10, 2001.

[35] Viqar Husain, Gabor Kunstatter, Brent Preston, and M. Birukou. Anti-de Sitter gravitational collapse. *Class. Quant. Grav.*, 20:L23–L30, 2003.

[36] Matthew W. Choptuik, Eric W. Hirschmann, Steven L. Liebling, and Frans Pretorius. Critical collapse of the massless scalar field in axisymmetry. *Phys. Rev.*, D68:044007, 2003.

[37] Stephen W. Hawking and George F. R. Ellis. *The Large scale structure of space-time*. Cambridge University Press, Cambridge, 1973.

[38] Piotr Bizoń. Is AdS stable? *Gen. Rel. Grav.*, 46(5):1724, 2014.

[39] Leszek M. Sokołowski. The bizarre anti-de Sitter spacetime. *Int. J. Geom. Meth. Mod. Phys.*, 13(09):1630016, 2016.

[40] Máximo Bañados, Claudio Teitelboim, and Jorge Zanelli. The Black hole in three-dimensional space-time. *Phys. Rev. Lett.*, 69:1849–1851, 1992.

[41] Joanna Jałmużna, Carsten Gundlach, and Tadeusz Chmaj. Scalar field critical collapse in 2+1 dimensions. *Phys. Rev.*, D92(12):124044, 2015.

[42] Maciej Maliborski. Instability of Flat Space Enclosed in a Cavity. *Phys. Rev. Lett.*, 109:221101, 2012.

[43] Hirotada Okawa, Vitor Cardoso, and Paolo Pani. Collapse of self-interacting fields in asymptotically flat spacetimes: do self-interactions render Minkowski spacetime unstable? *Phys. Rev.*, D89(4):041502, 2014.

[44] Hirotada Okawa, Vitor Cardoso, and Paolo Pani. Study of the nonlinear instability of confined geometries. *Phys. Rev.*, D90(10):104032, 2014.

[45] Vitor Cardoso and Jorge V. Rocha. Collapsing shells, critical phenomena and black hole formation. 2016.

[46] Rong-Gen Cai and Run-Qiu Yang. Multiple critical gravitational collapse of charged scalar with reflecting wall. 2016.

[47] Alex Buchel, Steven L. Liebling, and Luis Lehner. Boson stars in AdS spacetime. *Phys. Rev.*, D87(12):123006, 2013.

[48] Maciej Maliborski and Andrzej Rostworowski. A comment on "Boson stars in AdS". 2013.

[49] Venkat Balasubramanian, Alex Buchel, Stephen R. Green, Luis Lehner, and Steven L. Liebling. Holographic Thermalization, Stability of Anti-de Sitter Space, and the Fermi-Pasta-Ulam Paradox. *Phys. Rev. Lett.*, 113(7):071601, 2014.

[50] Stephen R. Green, Antoine Maillard, Luis Lehner, and Steven L. Liebling. Islands of stability and recurrence times in AdS. *Phys. Rev.*, D92(8):084001, 2015.

[51] Piotr Bizoń and Andrzej Rostworowski. Comment on "Holographic Thermalization, Stability of Anti-de Sitter Space, and the Fermi-Pasta-Ulam Paradox". *Phys. Rev. Lett.*, 115(4):049101, 2015.

[52] Venkat Balasubramanian, Alex Buchel, Stephen R. Green, Luis Lehner, and Steven L. Liebling. Reply to Comment on "Holographic Thermalization, Stability of Anti-de Sitter Space, and the Fermi-Pasta-Ulam Paradox". *Phys. Rev. Lett.*, 115(4):049102, 2015.

[53] Alex Buchel, Luis Lehner, and Steven L. Liebling. Scalar Collapse in AdS. *Phys. Rev.*, D86:123011, 2012.

[54] Joanna Jałmużna, Andrzej Rostworowski, and Piotr Bizoń. A Comment on AdS collapse of a scalar field in higher dimensions. *Phys. Rev.*, D84:085021, 2011.

[55] Richard Courant and David Hilbert. *Methods of Mathematical Physics Volume II*. John Wiley and Sons, 1989.

[56] Fritz John. *Partial Differential Equations*. Springer Verlag New York Inc., New York, 1991.

[57] Priscilla Canizares and Carlos F. Sopuerta. An Efficient Pseudospectral Method for the Computation of the Self-force on a Charged Particle: Circular Geodesics around a Schwarzschild Black Hole. *Phys. Rev.*, D79:084020, 2009.

[58] Priscilla Canizares, Carlos F. Sopuerta, and José Luis Jaramillo. Pseudospectral Collocation Methods for the Computation of the Self-Force on a Charged Particle: Generic Orbits around a Schwarzschild Black Hole. *Phys. Rev.*, D82:044023, 2010.

[59] Priscilla Canizares and Carlos F. Sopuerta. Tuning Time-Domain Pseudospectral Computations of the Self-Force on a Charged Scalar Particle. *Class. Quant. Grav.*, 28:134011, 2011.

[60] John C. Butcher. *Numerical Methods for Ordinary Differential Equations*. John Wiley & Sons, Chichester, 2003.

[61] William H. Press, Brian P. Flannery, Saul A. Teukolsky, and William T. Vetterling. *Numerical Recipes: The Art of Scientific Computing*. Cambridge University Press, Cambridge (UK) and New York, 1992.

[62] Bertil Gustafsson, Heinz-Otto Kreiss, and Joseph Oliger. *Time dependent problems*. John Wiley & Sons, New York, 1995.

[63] Brian Gough. *GNU Scientific Library Reference Manual - Third Edition*. Network Theory Ltd., 3rd edition, 2009.

[64] Rong-Gen Cai and Run-Qiu Yang. Scaling Laws in Gravitational Collapse. 2015.

Chapter 3

Holographic Collisions in Non-conformal Theories

> All you really need to know for the moment is that the universe is a lot more complicated than you might think, even if you start from a position of thinking it's pretty damn complicated in the first place.
>
> The Hitchhiker's Guide to the Galaxy
> Douglas Adams

The gauge/gravity duality, also known as holography, has provided interesting insights into the far-from-equilibrium properties of hot, strongly-coupled, non-Abelian plasmas that are potentially relevant for the quark-gluon plasma (QGP) created in heavy ion collision experiments at RHIC and LHC. The GQP is also very important because, according to the current cosmological model, it played a crucial role in the early stages of our Universe. Holographic models have shown that "hydrodynamisation", the process by which the plasma comes to be well described by hydrodynamics, can occur before "isotropisation", the process by which all pressures become approximately equal in the local rest frame. In order to make closer contact with quantum chromodynamics (QCD), and therefore with the QGP, it is important to understand non-conformal theories where it exists an equation of state that is not fixed by symmetry, and hence it needs not to be obeyed out of equilibrium. The relaxation process therefore involves an additional channel, the evolution of the energy density and the average pressure towards asymptotic values

related by the equation of state. We will refer to this process as “EoSisation" and once it has taken place we will say that the system has “EoSised”. This chapter is based on the published work of Refs. [1, 2] where it is shown that hydrodynamisation can occur before EoSisation. Another paper with more details about the numerical scheme and giving more evidence about the physical process has been recently released [3].

3.1 Holography and Heavy Ion Collisions

The idea of holography has been around in theoretical physics for several decades. One of the first suggestions came in the seventies in studies about the thermodynamics of black holes. The discovery that the black hole area cannot decrease [4] lead to an analogy with the laws of thermodynamics, the definition of the entropy of black holes and the final definition of a generalised second law of thermodynamics [5, 6]. The **Bekenstein-Hawking entropy** can be expressed as:

$$S_{BH} = \frac{1}{4}\,\frac{\kappa A}{l^2}, \tag{3.1}$$

where κ is the Boltzmann constant, A the area of the horizon of the BH and $l^2 = G\hbar$ is the Planck area. This is very surprising because it indicates that a three dimensional quantity like the entropy is determined just by two dimensional information, the black hole horizon. The evolution of this idea came in the nineties with Gerald ’t Hooft and Leonard Susskind when they formulated the Holographic Principle. In the case of BHs it can be formulated like this: the horizon contains the same information as the full three dimensional space and therefore the laws of physics in the surface are equivalent to the ones in the bulk and therefore the 3D space, and consequently also gravity, can be seen as the holographic realisation of the horizon.

Based on the previous ideas, Juan Maldacena published in 1997 a revolutionary paper (see Ref. [7]) in which he conjectured the equivalence of a field theory in 3+1 dimensions that lives in the boundary of a 4+1 AdS spacetime (AdS_5), i.e. a purely gravitational theory in one more dimensions. Later works [8, 9] have helped to sistemise and to formalise the principle now known as the gravity/gauge or AdS/CFT correspondence. Although a fundamental interpretation of this can be useful for advancing in the understanding of a quantum theory of gravity or the BH information paradox by using our knowledge of the gauge theory, here we are interested in the other way around: the use of the gravity side thanks to Numerical Relativity methods in AdS spacetimes to solve the dual problem asociated with the gauge field theory. In the usual formulation, the CFT stands for a conformal field theory and AdS_5 does not exactly refers to the AdS that we saw in the last chapter. There we studied *global* AdS spacetime and here we formulate the correspondence in a portion of it, the Poincaré patch. A simple scheme of the relation between the

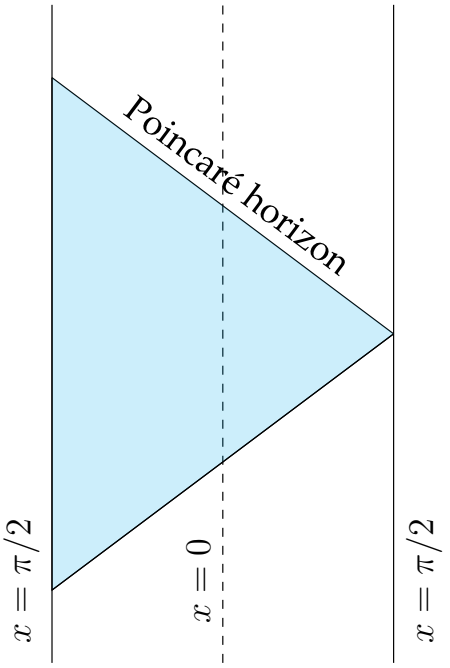

Figure 3.1: The Poincaré Patch Embedded in Global AdS: The blue area represents the Poincaré patch where it is defined the usual formulation of AdS/CFT. This is a patch of the global AdS spacetime that is limited by the Poincaré horizon.

global spacetime and the specific region corresponding to the Poincaré patch can be seen in Fig.3.1 and a more detailed description of it can be found in Ref. [10]. The metric in the Poincaré patch can be expressed as:

$$ds^2 = \frac{\ell^2}{u^2}\left(g_{\mu\nu}(x,u)dx^\mu dx^\nu + du^2\right), \tag{3.2}$$

where u is the AdS radial coordinate, the AdS boundary is located at $u = 0$. The object $g_{\mu\nu}$ is the 3+1 metric of the $u =$ const $3+1$ hypersurfaces and ℓ is again the AdS length scale.

The usual realisation of the gauge/gravity duality is formulated in a $\mathcal{N} = 4$ super Yang-Mills theory as a field theory that can be used to model heavy ion collisions. A dictionary between these two formulations is well known, allowing for systematic computations in both directions [11]. The setup of fields in the boundary determines completely the bulk geometry and, from the metric in the interior, the expected value of the stress energy tensor of the dual theory can be recovered using:

$$\langle T_{\mu\nu(x)}\rangle = g^{(4)}_{\mu\nu}(x), \tag{3.3}$$

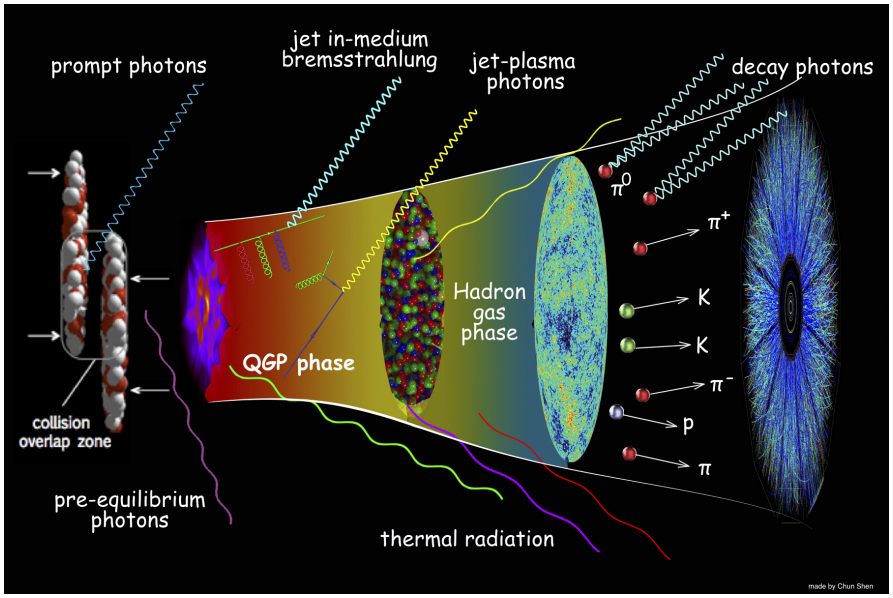

Figure 3.2: Relativistic Heavy Ion Collisions: This graph shows the stages present in the evolution of heavy ion collisions. Soon after the collision the system hydrodynamises into the QGP phase until the hadronization phase and the creation of the particles that reach the detectors. This graph is taken from Refs. [13, 14].

---

where $g^{(4)}_{\mu\nu}$ is a term of the series expansion of the 3+1 metric near the boundary:

$$g_{\mu\nu}(x,u) \sim \eta_{\mu\nu} + \sum_{n=4}^{\infty} g^{(n)}_{\mu\nu}(x) u^n. \tag{3.4}$$

This is just a simple description of the general picture of the AdS/CFT correspondence but the exact details of our work in the non-conformal case are a bit different and they are explained later.

Heavy ion collisions at the energies that the current technology allows are a very good framework to study the fundamental physics behind some of the most fundamental particles that we know at the moment: quarks and gluons. Colliders like the Relativistic Heavy Ion Collider (RHIC) and the Large Hadron Collider (LHC) use heavy nuclei like gold and lead to produce, during a very short time, a few fm/c, a plasma of quarks and gluons (QGP) that is very well described by hydrodynamics. This QGP is known to be formed very quickly after the collision, in less than 1 fm/c. In order to have an idea of the scale of this time, it is what it takes for light to go across a proton [12].

Fig. 3.2 shows the whole process of the collision of two heavy nuclei. After the QGP is formed, it last for around 10 fm/c. Then, the "free" particles are generated

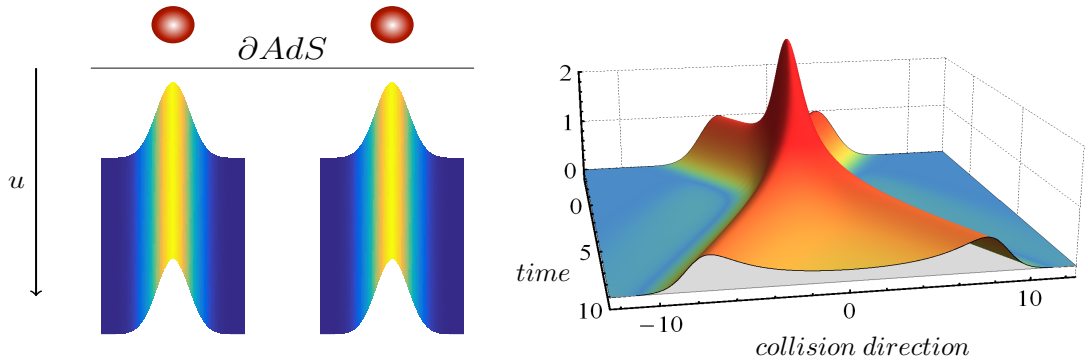

Figure 3.3: Left Plot: Holographic Model of two Motionless Particles: The scheme shows a simple picture of the AdS/CFT correspondence. The particles that we set in the CFT along the AdS boundary, $u = 0$, translate into shock waves in the bulk of AdS.
Right Plot: Energy Density in the Boundary for the Full Holographic Collision: The plot shows the energy density in the boundary, the peak in the figure represents the moment of collision and sets $t = 0$, after which the system thermalise. Figure from Ref. [15]

and thrown into the detectors. Since the formation of the QGP to the particle detection, the basic details of the process are more or less understood but there is still a key issue missing: how the QGP is created from the collision. The theory that we have to deal with is, of course, QCD in a regime where the interactions between quarks and gluons are very strong. And to solve this is very difficult. The fully non-perturbative strongly coupled regime is something that we cannot handle in QCD. There exists some approaches but perturbation theory is not very suitable for strong coupling and lattice simulations are not very good with dynamics. Here, we are going to address the problem using holography. The left plot of Fig. 3.3 shows an schematic representation of how QGP are modeled using holography. If we set two particles, two heavy nuclei, in the boundary where the field theory lives, according with the correspondence, this translates into two shock waves into the bulk. Then, we can evolve the metric in the AAdS spacetime and recover the information of the dual theory using Eq. (3.3).

The main problem we find using holography is that there is no well-defined theory of the dual of QCD. The theory that we are going to use shares common properties with QCD [16, 17] but has its limitations [18]. Current formulations require the number of colours to be very large $N_c \to \infty$. This is a problem because in QCD $N_c = 3$. However, this is not the greatest obstacle because the limit of large N_c is well known thanks to 't Hooft [19]. The real equivalence is defined between a gauge theory and a string theory. In order to be useful we need to take the limit in which string theory reduces to classical gravity and this requires, in the gauge side, the theory to be strongly coupled for all scales. This property excludes the possibility

of asympotic freedom and "contaminates" our theory with extra degrees of freedom that are not present in real QCD. Although one could think that another limitation is that the theory needs to be conformal, this is not mandatory and in this chapter we are going to show shock wave collisions in a non-conformal theory [1, 2].

In Refs. [20, 21], Paul Chesler and Laurence Yaffe presented a model of the heavy ion collisions using $\mathcal{N} = 4$ super-Yangs-Mills theory. There, they set the initial conditions for the heavy ions as Gaussian profiles and then they constructed the initial configuration for the bulk as shock wave perturbations. The conformal field theory represents infinite planar shocks where the only degree of freedom is the collision direction so effectively a 1+1 theory and its dual, a 2+1 AAdS. They studied how after the collision, the system hydrodynamises in a short time. The model was used in Refs. [15, 22] to describe different configurations like thinner shocks or asymmetric collisions and it is going to be extended in the next section to address the problem of non-conformal collisions. A model in 2+1 dimension in the gauge theory was presented in Ref. [23], where they drop one degree of symmetry to simulate off-centred collisions. Simulations in global AdS have been also presented in examples like Refs. [24, 25].

3.2 Setup for the Non-conformal Shock Waves

In the previous section, we have briefly explained the first models of shock wave collisions that were done for systems where the dictionary between the gauge theory and the gravitational one was fully known. One of their problems was that the gauge theory that was used to mimic QCD was conformal while QCD is not. In order to make close connection to the system we want to study, it is important to understand non-conformal theories. One crucial difference between the two cases is that in non-conformal theories, the equation of state, the relation between the energy density and the average pressure, is not fixed by symmetry, and hence it needs not to be obeyed out of equilibrium. The relaxation process therefore involves an additional channel, namely the evolution of the energy density and the average pressure towards asymptotic values related by the equation of state. We will refer to this process as "EoSization" and once it has taken place we will say that the system has "EoSized". One purpose of this chapter is to show that hydrodynamisation can occur before EoSization.

We will consider gravitational shock wave collisions in a five-dimensional bottom-up model [1, 2] consisting of gravity coupled to a scalar field with a non-trivial potential. At zero temperature, the dual four-dimensional gauge theory exhibits a Renormalization Group (RG) flow from an ultraviolet (UV) fixed point to an infrared (IR) fixed point. The source Λ[1] for the relevant operator that triggers

[1]From now on, in this chapter, Λ is going to be used to denote sources in the gauge theory and not for the cosmological constant that is hidden into the AdS length scale ℓ.

the flows is responsible for the breaking of conformal invariance. The dual gravity solution describes a domain-wall geometry that interpolates between two AdS spaces. We emphasise that our choice of model is not guided by the desire to mimic detailed properties of QCD but for simplicity: the UV fixed point guarantees that holography is on its firmest footing, since the bulk metric is asymptotically AdS; the IR fixed point guarantees that the solutions are regular in the interior and turning on a source for a relevant operator is the simplest way to break conformal invariance.

3.2.1 The Physical Model

We consider the dynamics in a five-dimensional holographic model consisting of gravity coupled to a scalar field ϕ with a non-trivial potential $V(\phi)$ [1, 2]. The action for our Einstein-scalar model is

$$S = \frac{2}{\kappa_5^2}\int d^5x\sqrt{-g}\left[\frac{1}{4}\mathcal{R} - \frac{1}{2}\left(\nabla\phi\right)^2 - V(\phi)\right], \tag{3.5}$$

where κ_5 is the five-dimensional Newton constant. From this action, we obtain the field equations:

$$R_{\mu\nu} - \frac{R}{2}g_{\mu\nu} = 8\pi T_{\mu\nu}\,, \tag{3.6}$$

$$\Box\phi = \frac{\partial V}{\partial\phi}\,, \tag{3.7}$$

where the stress-energy tensor has the usual form for an scalar field with potential $V(\phi)$

$$8\pi T_{\mu\nu} = 2\partial_\mu\phi\partial_\nu\phi - g_{\mu\nu}\left(g^{\alpha\beta}\partial_\alpha\phi\partial_\beta\phi + 2V(\phi)\right)\,. \tag{3.8}$$

The potential $V(\phi)$ sets the details of the dual gauge theory. We have chosen a simple potential characterised by a single parameter, $\phi_{\rm M}$, which reads:

$$\ell^2 V(\phi) = -3 - \frac{3}{2}\phi^2 - \frac{1}{3}\phi^4 + \left(\frac{1}{2\phi_{\rm M}^4} + \frac{1}{3\phi_{\rm M}^2}\right)\phi^6 - \frac{1}{12\phi_{\rm M}^4}\phi^8\,. \tag{3.9}$$

Note that $V(\phi)$ is negative, possesses a maximum at $\phi = 0$ and a minimum at $\phi = \phi_{\rm M} > 0$.

This choice of potential leads to interesting properties of the associated vacuum solution. In the ultraviolet (UV) limit, the resulting geometry is an AAdS$_5$ spacetime with radius ℓ because $V(0) = -3/\ell^2$. Moreover, at $\phi = 0$, the second derivative of the potential implies that the scalar field has mass $m^2 = -3/\ell^2$. Following the standard quantisation analysis, this means that, in the UV, this scalar field is dual to an operator in the gauge theory, $\mathcal{O}$, with dimension $\Delta_{\rm UV} = 3$. The solution near

$\phi = \phi_{\rm M}$, the infrared (IR), is going to be again an AAdS$_5$ spacetime but this time with radius

$$\ell_{\rm IR} = \sqrt{-\frac{3}{V\left(\phi_{\rm M}\right)}} = \frac{1}{1+\frac{1}{6}\phi_{\rm M}^2}\ell\,, \tag{3.10}$$

where the effective mass of the scalar field is given by:

$$m_{\rm IR}^2 = \frac{12}{\ell^2}\left(1+\frac{1}{9}\phi_{\rm M}^2\right) = \frac{12}{\ell_{IR}^2}\frac{\left(1+\frac{1}{9}\phi_{\rm M}^2\right)}{\left(1+\frac{1}{6}\phi_{\rm M}^2\right)^2}\,, \tag{3.11}$$

and, as a consequence, the operator $\mathcal{O}$ at the IR fixed point has dimension:

$$\Delta_{\rm IR} = 2+2\sqrt{1+\frac{m_{\rm IR}^2\ell_{\rm IR}^2}{4}} = 6\left(1+\frac{\phi_{\rm M}^2}{9}\right)\left(1+\frac{\phi_{\rm M}^2}{6}\right)^{-1}\,. \tag{3.12}$$

In most places, we are going to take $\ell = 1$, but we write it explicitly where the expressions or plots could present some ambiguities.

In order to compute the vacuum state of these theories, one needs to take an ansatz for the solution. In Fefferman-Graham (FG) coordinates [26, 27], the solution with translation invariance and no horizon can be written in the following form:

$$ds^2 = \frac{du_{\rm FG}^2}{u_{\rm FG}^2} + \exp\left[2a_{\rm FG}(u_{\rm FG})\right]\eta_{\mu\nu}\,dx^\mu dx^\nu\,, \tag{3.13}$$

being $a_{\rm FG}(u_{\rm FG})$ the non-trivial field that characterise the metric and $u_{\rm FG}$ the FG radial (holographic) coordinate. The computation of the vacuum state is simplified when the potential can be derived from a super-potential $W(\phi)$ as:

$$V(\phi) = -\frac{4}{3}W\left(\phi\right)^2 + \frac{1}{2}W'\left(\phi\right)^2\,. \tag{3.14}$$

For the potential that we chose in Eq. (3.9), the superpotential is:

$$\ell\, W\left(\phi\right) = -\frac{3}{2} - \frac{\phi^2}{2} + \frac{\phi^4}{4\phi_{\rm M}^2}\,. \tag{3.15}$$

In this case, the scalar field profile $\phi(u_{\rm FG})$ and the metric coefficient $a_{\rm FG}(u_{\rm FG})$ can be obtained from the equations

$$-u_{\rm FG}^2\frac{d\,a_{\rm FG}}{du_{\rm FG}} = -\frac{2}{3}W, \quad -u_{\rm FG}^2\frac{d\,\phi}{du_{\rm FG}} = \frac{\partial W}{\partial\phi}\,. \tag{3.16}$$

Fortunately, the equations have an analytic solution for our super-potential chosen,

$$e^{2a_{\rm FG}(u_{\rm FG})} = \frac{\phi_0^2}{\phi^2}\left(1-\frac{\phi^2}{\phi_{\rm M}^2}\right)^{\frac{\phi_{\rm M}^2}{6}+1} e^{-\frac{\phi^2}{6}}\,, \tag{3.17}$$

$$\phi(u_{\rm FG}) = \frac{\phi_0\, u_{\rm FG}}{\sqrt{1+\frac{\phi_0^2}{\phi_{\rm M}^2}u_{\rm FG}^2}}\,, \tag{3.18}$$

where ϕ_0 is an arbitrary constant that controls the magnitude of the non-normalisable mode of the scalar field. As we will see, in the dual gauge theory side, ϕ_0 is identified with the source of the dimension-3 operator $\mathcal{O}$. The presence of this source is what breaks conformal invariance explicitly.

3.2.2 Gauge Theory Physical Quantities

The small field behaviour of the superpotential, Eq. (3.15), is identical to the one of the GPPZ flow [28]. Therefore, we can determine the vacuum expectation values (VEV) of the stress tensor and the scalar operator. We begin by expanding the metric and the scalar field in powers of $u_{\rm FG}$ in the vicinity of $u_{\rm FG}\to 0$. Following [29], we write the 5-dimensional metric for AAdS geometries in generic FG form:

$$ds^2 = \frac{1}{u_{\rm FG}^2}\left(du_{\rm FG}^2 + g_{\mu\nu}\,dx^\mu dx^\nu\right)\,, \tag{3.19}$$

and we write the power expansion for the metric and the scalar field near $u_{\rm FG}=0$ as

$$g_{\mu\nu} = \eta_{\mu\nu} + g^{(2)}_{\mu\nu}\,u_{\rm FG}^2 + g^{(4)}_{\mu\nu}\,u_{\rm FG}^4 + \dots\,, \tag{3.20}$$

$$\phi = \phi_0 u_{\rm FG}\left(1+\phi^{(2)}u_{\rm FG}^2+\dots\right)\,. \tag{3.21}$$

The expectation values of the field theory operators are then given by

$$\langle T_{\mu\nu}\rangle = \frac{2\ell^3}{\kappa_5^2}\left[g^{(4)}_{\mu\nu} + \left(\Lambda^2\,\phi^{(2)} - \frac{\Lambda^4}{18} + \frac{\Lambda^4}{4\phi_{\rm M}^2}\right)\eta_{\mu\nu}\right]\,, \tag{3.22}$$

$$\langle \mathcal{O}\rangle = -\frac{2\ell^3}{\kappa_5^2}\left(2\Lambda\phi^{(2)} + \frac{\Lambda^3}{\phi_{\rm M}^2}\right)\,, \tag{3.23}$$

where $\Lambda = \frac{\phi_0}{\ell}$. Eqs (3.22) and (3.23) imply the Ward identity for the trace of the stress tensor

$$\left\langle T^\mu_\mu\right\rangle = -\Lambda\,\langle\mathcal{O}\rangle\,. \tag{3.24}$$

We adopt a renormalization scheme such that $\langle T_{\mu\nu}\rangle = \langle\mathcal{O}\rangle = 0$ in the vacuum state. Henceforth, we omit the expectation value signs and work with the rescaled quantities

$$(\mathcal{E}, P_{x^i}, \mathcal{V}) = \tfrac{\kappa_5^2}{2\ell^3}(-T^t_t, T^{x^i}_{x^i}, \mathcal{O})\,. \tag{3.25}$$

Using these variables, the Ward identity takes the form

$$\mathcal{E} - 3\bar{P} = \Lambda \mathcal{V} \,, \tag{3.26}$$

where

$$\bar{P} = \frac{1}{3} \sum_i P_{x^i}, \tag{3.27}$$

is the average pressure. Out of equilibrium the average pressure is not determined by the energy density because the scalar field expectation value $\mathcal{V}$ fluctuates independently. In contrast, in equilibrium, $\mathcal{V}$ is determined by the energy density and the Ward identity becomes the equation of state

$$\bar{P} = P_{\rm eq}(\mathcal{E}) \,, \tag{3.28}$$

with

$$P_{\rm eq}(\mathcal{E}) = \tfrac{1}{3} \left[\mathcal{E} - \Lambda \mathcal{V}_{\rm eq}(\mathcal{E}) \right] . \tag{3.29}$$

3.2.3 Thermodynamics and Transport

To explore the thermodynamics of our model, we look for static black brane solutions of the action (3.5) following the approach of [30]. Since for these solutions the scalar field is a monotonic function of $u_{\rm FG}$, we may use it as a coordinate when solving the dynamical equations. The value of ϕ at the black brane horizon, $\phi_{\rm H}$, univocally characterises the black brane solution. Therefore, by imposing the appropriate horizon boundary conditions at different $\phi_{\rm H}$ values one can compute all the equilibrium geometries. Then, finding the thermodynamics amounts to finding a family of black brane solutions parametrised by $\phi_{\rm H}$, and obtaining their Hawking temperatures, T, and entropy densities s. This construction can be found in detail in Ref. [1].

For our purposes here, it is enough to note that we find a set of values $(\phi_{\rm H}, T, s)$ for each model, characterised by $\phi_{\rm M}$. With these values, one can compute all the thermodynamic quantities of interest as well as the bulk viscosity ζ. In Fig. 3.4 we plot the dimensionless quantity

$$s_R = \frac{\kappa_5^2}{2\pi^4 \ell^3} \frac{s}{T^3} \,, \tag{3.30}$$

as a function of the inverse temperature for two different values of $\phi_{\rm M}$. Since the theory is conformal both at the UV and at the IR limits, the high and low temperature behaviour of the entropy density must coincide with that of a relativistic conformal theory and scale as T^3. In the intermediate region, this scaling is not fulfilled and therefore we can interpret this quantity as a measure of the non-conformality of the gauge theory.

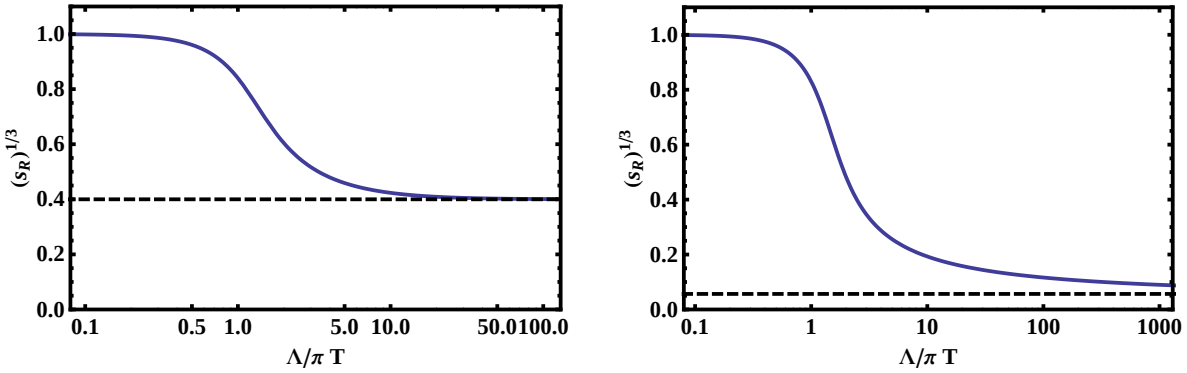

Figure 3.4: Ratio of the Entropy Density s_R to the Temperature: The two plots show the entropy-temperature ratio as a function of the inverse temperature for two different potentials: on the left for $\phi_{\rm M} = 3$ and on the right for $\phi_{\rm M} = 10$. The dashed line corresponds to $\ell_{\rm IR}/\ell$. Figure from Ref. [1].

For a relativistic CFT, s/T^3 is proportional to the number of degrees of freedom in the theory, which for an $SU(N)$ gauge theory with matter in the adjoint representation scales as N^2. For example, for $\mathcal{N} = 4$ SYM we have:

$$\frac{s}{T^3} = \frac{\pi^2}{2} N^2, \tag{3.31}$$

but the precise coefficient depends on the specific theory. In terms of the parameters of the dual gravity description this quantity becomes:

$$\frac{s}{T^3} = \frac{2\pi^4 \ell^3}{\kappa_5^2}. \tag{3.32}$$

In our bottom-up setup, the above argument allows us to define the number of degrees of freedom at the fixed points holographically in terms of the effective AdS radius. In particular, the quantity s_R should approach to the unity at high temperatures and $(\ell_{\rm IR}/\ell)^3$ at low temperatures, which is confirmed by the plots shown in Fig. 3.4.

The non-conformal behaviour already observed in the equation of state of the system is also reflected in the transport properties of the dual gauge theory plasma. Since this is isotropic, at leading order in gradients transport phenomena is controlled by only two coefficients, the shear viscosity η and the bulk viscosity ζ. Because of the universality of the shear viscosity to the entropy ratio [31] in all theories with a two-derivative gravity dual, we have that this ratio in our model takes the same value as in the conformal $\mathcal{N} = 4$ theory, that is

$$\frac{\eta}{s} = \frac{\pi}{4}. \tag{3.33}$$

In contrast, the bulk viscosity, which would vanish identically in a CFT, is non-zero in our model. Following Ref. [32] we determine the bulk viscosity by studying the dependence of the entropy on the value of the scalar field at the horizon using the expression:

$$\frac{\zeta}{\eta} = 4\left(\frac{d\log s}{d\phi_{\rm H}}\right)^{-2} . \tag{3.34}$$

3.2.4 The Metric of the Shock Wave

In Fefferman-Graham coodinates, it is possible to find a quasi-analytic solution for a single travelling shock wave on a vacuum background. The form of the metric simply corresponds to the vacuum metric, Eq. (3.13), plus the addition of the term $f(u_{\rm FG})h(x_\pm)dx_\pm^2$,

$$ds^2 = \frac{du_{\rm FG}^2}{u_{\rm FG}^2} + f(u_{\rm FG})h(x_\pm)dx_\pm^2 + e^{2a_{\rm FG}(u_{\rm FG})}\left(-dx_+dx_- + d\mathbf{x}_\perp^2\right), \tag{3.35}$$

where $x_\pm = z \pm t$, z is the direction of propagation of the shock wave, and $\mathbf{x}_\perp$ are the perpendicular directions to it. The function $h(x_\pm)$ is an arbitrary function that describes the profile of the shock wave.

The propagation of the shock wave at the speed of light does not alter the vacuum profiles of $a_{\rm FG}$ and ϕ and therefore, they are the same ones as in vacuum. There, the only remaining function to be determined is f. The equation for $f(u_{\rm FG})$ is a second order differential equation that comes from the EFEs and needs to be solved numerically:

$$u_{\rm FG}^2\frac{\partial^2 f}{\partial u_{\rm FG}^2} + u_{\rm FG}\frac{\partial f}{\partial u_{\rm FG}} - f\left[2\left(u_{\rm FG}^2\frac{\partial^2 a_{\rm FG}}{\partial u_{\rm FG}^2} + u_{\rm FG}\frac{\partial a_{\rm FG}}{\partial u_{\rm FG}}\right) + 4\left(-u_{\rm FG}\frac{\partial a_{\rm FG}}{\partial u_{\rm FG}}\right)^2\right] = 0, \tag{3.36}$$

from where we can derive an integral expression for $f(u_{\rm FG})$:

$$f(u_{\rm FG}) = 4\,e^{2a_{\rm FG}(u_{\rm FG})}\int_0^{u_{\rm FG}}\frac{d\tilde{u}}{\tilde{u}}\,e^{-4a_{\rm FG}(\tilde{u})}. \tag{3.37}$$

An additional difficulty for the numerical computation of the function $f(u_{\rm FG})$ is that it grows exponentially with $u_{\rm FG}$. However, this problem can be solved by computing instead the redefined function $g(u_{\rm FG}) = e^{2a_{\rm FG}(u_{\rm FG})}f(u_{\rm FG})$ which, takes values between 0 and 1.

3.3 Numerical Framework for the Holographic Collisions

In this section we describe all the ingredients to formulate the physical problem described previously and to simulate it numerically. We start, of course, with the expressions of the EFEs in the appropriate coordinates and the correct manner to write the metric coefficient for them to be finite in our computational domain. We also describe the discretisation of the AAdS spacetime and the procedure to construct proper initial conditions. Finally, we explain how to compute our desired gauge theory quantities from the gravitational variables.

3.3.1 Field Equations

We follow the notation of [20] and begin by writing the 5D metric using Eddington-Finkelstein (EF) coordinates

$$ds^2 = -Adt^2 + \Sigma^2\left(e^B d\boldsymbol{x}_\perp^2 + e^{-2B}dz^2\right) + 2dt(dr + Fdz)\,, \tag{3.38}$$

where A, B, Σ, and F are functions of the radial coordinate r, the time t, the coordinate corresponding to the collision direction z and $\boldsymbol{x}_\perp = (x_1, x_2)$ denotes the two perpendicular directions. Note that t is a null time coordinate (in the literature it is usually called v when using EF coordinates), $t =$ const surfaces are null, and not spacelike.

Written in this form, the form of the metric is invariant under the following transformations

$$\begin{aligned} r &\to \bar{r} = r + \xi(t,z) \\ \Sigma &\to \bar{\Sigma} = \Sigma \\ B &\to \bar{B} = B \\ A &\to \bar{A} = A + 2\partial_t\xi(t,z) \\ F &\to \bar{F} = F - \partial_z\xi(t,z) \end{aligned} \quad . \tag{3.39}$$

Upon plugging the metric (3.38) into Eq. (3.6) the resulting system of PDEs conveniently obeys a particular nested structure. This structure consists of a sequence of radial ODEs at each $t =$ const null slice that can be solved in a certain order, see e.g. [33].

The equations of motion for our present case are given by

$$\Sigma'' = -\frac{1}{6}\Sigma\left(3\left(B'\right)^2 + 4\left(\phi'\right)^2\right)\,, \tag{3.40a}$$

$$\Sigma^2 F'' = \Sigma\left(6\tilde{\Sigma}B' + 4\tilde{\Sigma}' + 3F'\Sigma'\right) + \Sigma^2\left(3\tilde{B}B' + 2\tilde{B}' + 4\tilde{\phi}\phi'\right) - 4\tilde{\Sigma}\Sigma'\,, \tag{3.40b}$$

$$
\begin{aligned}
12\Sigma^3(d_+\Sigma)' &= e^{2B}\Big[\Sigma^2\left(4\tilde{B}F' - 4\left(\tilde{\tilde{B}}+\tilde{\phi}^2\right) - 7\tilde{B}^2 + 2\tilde{F}' + (F')^2\right) \\
&\quad + 2\Sigma\left(\tilde{\Sigma}\left(F' - 8\tilde{B}\right) - 4\tilde{\tilde{\Sigma}}\right) + 4\tilde{\Sigma}^2\Big] \\
&\quad - 8\Sigma^2\left(\Sigma^2 V(\phi) + 3(d_+\Sigma)\Sigma'\right), \qquad (3.40c) \\
6\Sigma^4(d_+B)' &= e^{2B}\Big[\Sigma^2\left(-\tilde{B}F' + \tilde{B}^2 + \tilde{\tilde{B}} - 2\tilde{F}' + 4\tilde{\phi}^2 - (F')^2\right) \\
&\quad + \Sigma\left(\tilde{\Sigma}\left(\tilde{B} + 4F'\right) + 2\tilde{\tilde{\Sigma}}\right) - 4\tilde{\Sigma}^2\Big] \\
&\quad - 9\Sigma^3\left((d_+\Sigma)B' + (d_+B)\Sigma'\right), \qquad (3.40d) \\
3\Sigma'\Sigma^2(d_+\phi) &= -e^{2B}\Sigma\left(2\tilde{B}\tilde{\phi} - \tilde{\phi}F' + \tilde{\tilde{\phi}}\right) + e^{2B}\tilde{\Sigma}\tilde{\phi} \\
&\quad + \Sigma^3\left(-\left(V'(\phi) - 2(d_+\phi)'\right)\right) + 3(d_+\Sigma)\Sigma^2\phi', \qquad (3.40e) \\
6\Sigma^4 A'' &= 3e^{2B}\left(\Sigma^2\left(4\left(\tilde{\tilde{B}}+\tilde{\phi}^2\right) + 7\tilde{B}^2 - (F')^2\right) + 8\Sigma\left(2\tilde{B}\tilde{\Sigma} + \tilde{\tilde{\Sigma}}\right) - 4\tilde{\Sigma}^2\right) \\
&\quad + 2\Sigma^4\left(-9(d_+B)B' + 4V(\phi) - 12(d_+\phi)\phi'\right) + 72(d_+\Sigma)\Sigma^2\Sigma', \qquad (3.40f) \\
2\Sigma^2(d_+F)' &= -\Sigma^2\left(2B'\left(\tilde{A} + 2(d_+F)\right) + 2\tilde{A}' + 6(d_+B)\tilde{B}\right) \\
&\quad - \Sigma^2\left(4\tilde{(d_+B)} + 8(d_+\phi)\tilde{\phi} + A'F'\right) \\
&\quad + 2\Sigma\left(\Sigma'\left(\tilde{A} + 2(d_+F)\right) - 6(d_+B)\tilde{\Sigma} - 4\tilde{(d_+\Sigma)} - 3(d_+\Sigma)F'\right) \\
&\quad + 8(d_+\Sigma)\tilde{\Sigma}, \qquad (3.40g)
\end{aligned}
$$

where, for any function g, the tilde means:

$$\tilde{g} \equiv (\partial_z - F\partial_r)\, g, \qquad (3.41)$$

the prime stands for:

$$g' \equiv \partial_r g \qquad (3.42)$$

and the d_+ operator denotes:

$$d_+ g \equiv \left(\partial_t + \frac{A}{2}\partial_r\right) g\,. \qquad (3.43)$$

Note that these equations can be arranged in the following general form

$$\left[\alpha_g(r,t,z)\partial_{rr} + \beta_g(r,t,z)\partial_r + \gamma_g(r,t,z)\right] g(r,t,z) = -S_g(r,t,z)\,, \qquad (3.44)$$

where $g = \Sigma,\ F,\ d_+\Sigma,\ d_+B,\ d_+\phi,\ A,\ d_+F$. These equations are solved by imposing reflecting boundary conditions at the AdS boundary, at $u = 1/r = 0$, which take the form

$$A(u,t,z) = \frac{1}{u^2} + \frac{2\xi(t,z)}{u} - 2\partial_t\xi(t,z) + \xi(t,z)^2 - \frac{2\phi_0^2}{3} + \phi_0\partial_t\phi_2(t,z) + u^2 a_4(t,z)$$

$$- \frac{2}{3}u^3(3a_4(t,z)\xi(t,z) + \partial_z f_2(t,z)) + O(u^4), \tag{3.45a}$$

$$B(u,t,z) = u^4 b_4(t,z) + O(u^5), \tag{3.45b}$$

$$\Sigma(u,t,z) = \frac{1}{u} + \xi(t,z) - \frac{\phi_0^2 u}{3} + \frac{1}{3}\phi_0^2 u^2 \xi(t,z) + \frac{1}{54}\phi_0 u^3 \left(-18\phi_0 \xi(t,z)^2 - 18\phi_2(t,z) + \phi_0^3\right) + O(u^4), \tag{3.45c}$$

$$F(u,t,z) = \partial_z \xi(t,z) + u^2 f_2(t,z) + u^3 \left(\frac{4}{15}\left(\phi_0 \partial_z \phi_2(t,z) - 6\partial_z b_4(t,z)\right) - 2f_2(t,z)\xi(t,z)\right) + O(u^4), \tag{3.45d}$$

$$\phi(u,t,z) = \phi_0 u - \phi_0 u^2 \xi(t,z) + u^3\left(\phi_0 \xi(t,z)^2 + \phi_2(t,z)\right) + u^4\left(-\phi_0 \xi(t,z)^3 - 3\xi(t,z)\phi_2(t,z) + \partial_t \phi_2(t,z)\right) + O(u^5), \tag{3.45e}$$

$$d_+ B(u,t,z) = -2u^3 b_4(t,z) + O(u^4), \tag{3.45f}$$

$$d_+\Sigma(u,t,z) = \frac{1}{2u^2} + \frac{\xi(t,z)}{u} + \frac{1}{2}\xi(t,z)^2 - \frac{\phi_0^2}{6} + \frac{1}{36}u^2\left(18a_4(t,z) + 18\phi_0\phi_2(t,z) - 5\phi_0^4\right) + O(u^3), \tag{3.45g}$$

$$d_+\phi(u,t,z) = -\frac{\phi_0}{2} + u^2\left(\frac{\phi_0^3}{3} - \frac{3}{2}\phi_2(t,z)\right) + O(u^3), \tag{3.45h}$$

$$d_+ F(u,t,z) = \partial_{tz}\xi(t,z) - u f_2(t,z) + O(u^2). \tag{3.45i}$$

The functions $a_4(t,z)$ and $f_2(t,z)$ are free functions defined on the boundary whose evolution can be determined using the conservation of the stress energy tensor in the boundary [21], from where we obtain the equations:

$$\partial_t a_4 = -\frac{4}{3}\left(\partial_z f_2 + \phi_0 \partial_t \phi_2\right), \tag{3.46a}$$

$$\partial_t f_2 = \frac{1}{4}\left(-\partial_z a_4 - 8\partial_z b_4 + \frac{4}{3}\phi_0 \partial_z \phi_2\right), \tag{3.46b}$$

where b_4 can be obtained from B through (3.45b) and both ϕ_2 and $\partial_t\phi_2$ are determined from ϕ through (3.45e).

The function $\xi(t,z)$ encodes the residual gauge freedom associated with the radial shifts [21]. A convenient choice is to treat $\xi(t,z)$ as another evolved variable and to choose its evolution equation by requiring that the apparent horizon position lies at some constant radial coordinate value $r = r_h$. We thus want to impose

$$\Theta|_{r=r_h} = 0\,, \qquad \partial_t \Theta|_{r=r_h} = 0\,, \tag{3.47}$$

at all times, where Θ is the expansion of the outgoing null geodesics for metric (3.38). At the surfaces $r = \text{const}$, Θ is given by

$$\Theta = -\frac{1}{2}e^{2B}F\left(3F\partial_r\Sigma - 2\partial_z\Sigma\right) + e^{2B}\Sigma\left(2F\partial_z B + \partial_z F\right) - 3\Sigma^2 d_+\Sigma\,. \tag{3.48}$$

A simple way to impose the condition in Eq. (3.47) numerically is the following

$$\left(\partial_t\Theta + \kappa\Theta\right)|_{r=r_h} = 0\,, \tag{3.49}$$

where κ is a positive parameter typically chosen to be one. The advantage of imposing such a condition is that it is constructed to drive the $\Theta = 0$ surface back to $r = r_h$ whenever numerical errors accumulate. This turns out to work very well in practice.

Equation (3.49) can be expanded and then we have an equation for $\partial_t\xi$ of the form

$$\Big[\alpha_\xi(t,z)\partial_{zz} + \beta_\xi(t,z)\partial_z + \gamma_\xi(t,z)\Big]\partial_t\xi(t,z) = -S_\xi(t,z)\,, \tag{3.50}$$

that we solved at $r = r_h$. This is a second order linear ODE in the coordinate z.

3.3.2 Field Redefinitions and Evolution Algorithm

To integrate the system of the Eqs. (3.40), we need to impose the boundary conditions. It is very convenient to introduce $u = 1/r$ as our radial coordinate and redefine the variables so that the divergent pieces at $u = 0$ are absent. Motivated by Eq. (3.45), we set the definitions

$$B(u,t,z) \equiv u^4 B_f(u,t,z), \tag{3.51a}$$
$$\Sigma(u,t,z) \equiv \frac{1}{u} + \xi(t,z) - u\frac{\phi_0^2}{3} + u^2\frac{\phi_0^2}{3}\xi(t,z) + u^3\Sigma_f(u,t,z), \tag{3.51b}$$
$$F(u,t,z) \equiv \partial_z\xi(t,z) + u^2 F_f(u,t,z), \tag{3.51c}$$
$$A(u,t,z) \equiv \frac{1}{u^2} + \frac{2\xi(t,z)}{u} - 2\partial_t\xi(t,z) + \xi(t,z)^2 - \frac{2\phi_0^2}{3} + u^2 A_f(u,t,z), \tag{3.51d}$$
$$\phi(u,t,z) \equiv u\phi_0 - u^2\phi_0\xi(t,z) + u^3\phi_0^3\phi_f(u,t,z), \tag{3.51e}$$
$$d_+\Sigma(u,t,z) \equiv \frac{1}{2u^2} + \frac{\xi(t,z)}{u} + \frac{\xi(t,z)^2}{2} - \frac{\phi_0^2}{6} + u^2\dot{\Sigma}_f(u,t,z), \tag{3.51f}$$
$$d_+B(u,t,z) \equiv u^3\dot{B}_f(u,t,z), \tag{3.51g}$$
$$d_+\phi(u,t,z) \equiv -\frac{\phi_0}{2} + u^2\phi_0^3\dot{\phi}_f(u,t,z), \tag{3.51h}$$
$$d_+F(u,t,z) \equiv \partial_{tz}\xi(t,z) + u\dot{F}_f(u,t,z), \tag{3.51i}$$

where the variables with the f subscript are the ones that are used for the numerical evolution.

Now that we have worked out all the necessary details, the evolution algorithm is then as follows:

1. At any given time t_n, which can be the initial time after having performed the transformation of Eq. (3.39) that puts the apparent horizon at constant u, we know $B_f(u, t_n, z)$, $\phi_f(u, t_n, z)$, $\xi(t_n, z)$, $a_4(t_n, z)$ and $f_2(t_n, z)$;
2. Successively solve the elliptic equations (3.40) with the redefinitions of Eq. (3.51). The equations are solved in a specific sequence in a way that a given equation only depends on the previous one. This order is Σ_f, F_f, $\dot{\Sigma}_f$, $\dot{B}_f$, $\dot{\phi}_f$, A_f. All of them are radial ODEs subject to the boundary conditions (3.45) ;
3. Eq. (3.50) is solved to get $\partial_t \xi(t_n, z)$ and afterwards, $\partial_t B_f(t_n, u, z)$ and $\partial_t \phi_f(t_n, u, z)$ can be obtained through equation (3.43) using (3.51d);
4. Obtain $\partial_t a_4(t_n, z)$ and $\partial_t f_2(t_n, z)$ through (3.46) and, together with the already obtained $\partial_t \xi(t_n, z)$, $\partial_t B_f(u, t_n, z)$, $\partial_t \phi_f(u, t_n, z)$, advance all these quantities to time t_{n+1} with a Runge-Kutta or Adams-Bashforth ODE solver.
5. Return to step 1.

3.3.3 Discretization

Eqs. (3.40) are written in a form that appear decoupled in the radial coordinate u and in the collision direction coordinate z. Then, they can be solved as ODEs in the u direction for each point in z. The z direction is discretized using a uniform grid where periodic boundary conditions are imposed, while along the u direction we use a *Lobatto-Chebyshev* grid with $N_u + 1$ points, for details about this grid and the PSC method, see the Sec. 1.3. The collocation points are given by

$$X_i = -\cos\left(\frac{\pi\, i}{N_u}\right) \qquad (i = 0, 1, \ldots, N_u)\,, \tag{3.52}$$

are defined in the range $[-1, +1]$, and can be mapped to our *physical* grid using the linear mapping:

$$u_i = \frac{u_R + u_L}{2} + \frac{u_R - u_L}{2} X_i \qquad (i = 0, 1, \ldots, N_u)\,, \tag{3.53}$$

where $u_L = 0$ and u_R are the limits of the computational domain of u.

Since the differential equations (3.40) are solved in u for each z point, the only important operation performed in the z direction are the partial derivatives with

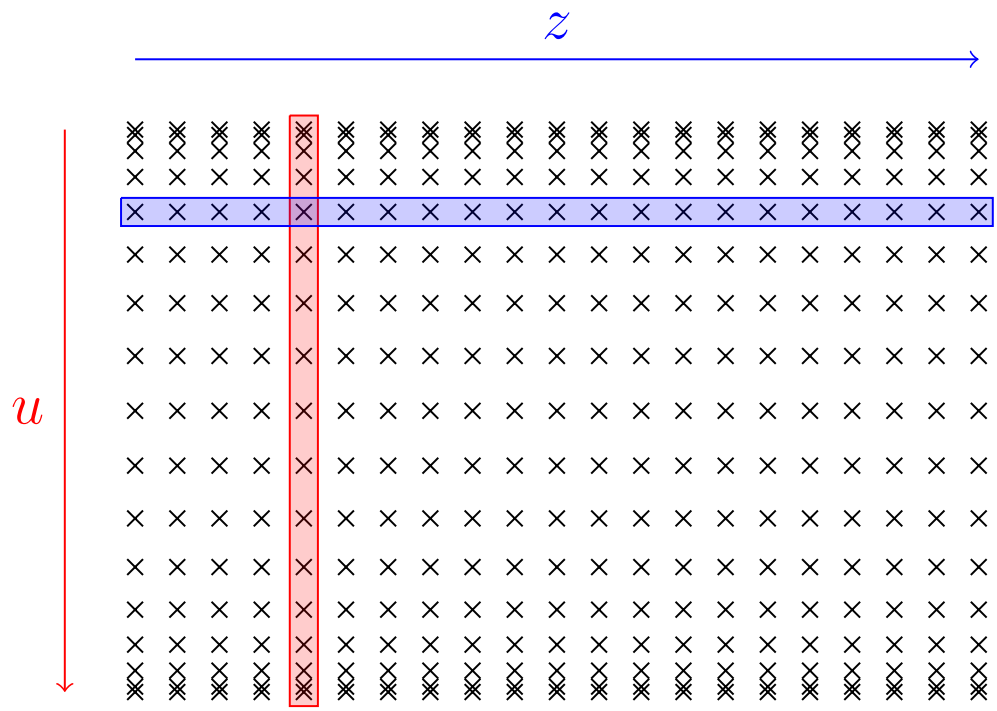

Figure 3.5: Shock Wave Grid Scheme: Two dimensional grid for the AAdS space. The radial direction u is discretised using a Chebyshev-Lobatto pseudo-spectral grid (see Sec. 1.3 for details). All the operations that involve only this coordinate (in red) are performed using PSC methods. In the z direction the grid points are set uniformly.

respect to that direction present in the equations. To evaluate them we use a fourth-order accurate (central) finite difference approximation:

$$\left.\frac{df(z)}{dz}\right|_{z_i} = \frac{1}{\Delta z}\left[\frac{f(z_{i-2})}{12} - \frac{2\,f(z_{i-1})}{3} + \frac{2\,f(z_{i+1})}{3} - \frac{f(z_{i+2})}{12}\right], \tag{3.54}$$

for the first order derivatives and:

$$\left.\frac{d^2f(z)}{dz^2}\right|_{z_i} = \frac{1}{\Delta z}\left[-\frac{f(z_{i-2})}{12} + \frac{4\,f(z_{i-1})}{3} - \frac{5\,f(z_i)}{2} + \frac{4\,f(z_{i+1})}{3} - \frac{f(z_{i+2})}{12}\right], \tag{3.55}$$

for the second order ones. In this direction, we find spurious noise that accumules the form of the high-frequency modes of our variables. This is common to finite differences schemes. In order to remove it, or at least to reduce it to a level that we can control, we add numerical dissipation. We have therefore implemented a Kreiss-Oliger dissipation method [34] whereby, after each time step, all our evolved

quantities $f \in \{B_f, \phi_f, a_4, f_2, \xi\}$ are added a term of the form

$$D_{\rm KO} f_i \equiv \frac{\sigma}{64} \left(f_{i-3} - 6 f_{i-2} + 15 f_{i-1} - 20 f_i + 15 f_{i+1} - 6 f_{i+2} + f_{i+3} \right) , \tag{3.56}$$

where i labels the grid point in the z direction and σ is a tuneable dissipation parameter which must be smaller than one for stability. In our computations we have typically fixed it to be 0.2. This procedure works effectively as a low-pass filter that eliminates the high-frequency modes that are related with the noise.

In the radial direction u, the use of PSC methods allows us to have good accuracy in operations involving this coordinate. As we mentioned previously in Eq. (3.44), the radial equations for solving the metric coefficients can be written in a general form

$$\left[\alpha_g(u,t,z) \partial_{uu} + \beta_g(u,t,z) \partial_u + \gamma_g(u,t,z) \right] g(u,t,z) = -S_g(u,t,z) \, ,$$

where, again, g represents the metric coefficients $\Sigma,\ F,\ d_+\Sigma,\ d_+B,\ d_+\phi,\ A,\ d_+F$. Once our coordinate is discretized, the differential operator becomes a matrix one acting over the vector of the values of the functions at the collocation points. The discrete form is:

$$\left[\alpha_g^i(t,z) \mathcal{D}_{uu}^{ij} + \beta_g^i(t,z) \mathcal{D}_u^{ij} + \gamma_g^i(u,t,z) \right] g^j(t,z) = -S_g^j(t,z) \, ,$$

where $\mathcal{D}_u$ and $\mathcal{D}_{uu}$ represent the first and second order derivative operators for a Lobatto-Chebyshev grid in the physical representation, and (i, j) are indices in the u coordinate. We now construct the operator (matrix) defined inside the brackets and then invert it to solve for the collocation values of the function g. Boundary conditions are imposed by replacing full rows in this operator by the values we need to fix. In the general case, for a second order operator we replace the rows $j = 0$, $j = N$ by the value of the function and its derivative at $u = 0$ according to Eq. (3.45).

Another useful tool associated with spectral methods is the possibility of filtering, which plays the role of the dissipation term seen in the finite difference scheme. We can also damp high order modes that may originate in the computation but, in this case, directly in the spectral representation. After each time step, we apply an exponential filter to the spectral coefficients of our u-dependent evolved quantities $\hat{f} \in \{\hat{B}_f, \hat{\phi}_f\}$. The complete scheme for an exponential filter is:

$$\{ f_i \} \overset{FFT}{\longrightarrow} \left\{ \hat{f}_k \right\} \longrightarrow \left\{ \hat{f}_k \, e^{-\alpha (k/N_u)^{\gamma N_u}} \right\} \overset{FFT}{\longrightarrow} \{ f_i \} \tag{3.57}$$

where α and γ are tuneable parameters of the filter which we typically fix to $\alpha = 36.0437$ and $\gamma = 8$. In the spectral representation of the PSC method, the absolute value of the coefficients should decay exponentially. In this sense, the higher order coefficients are the ones that acumulate the noise that little by little grow and affect to more coefficients. This filter, eliminates this higher order coefficients before the noise piles up.

3.3.4 Initial Data

As we described in Sec. 1.2.2, the characteristic formulation of Einstein's Field Equations allows to specify the initial data needed for an evolution by freely setting the functions $B(u,z)$, $\phi(u,z)$, $\xi(z)$, $a_4(z)$ and $f_2(z)$. For our intended applications, we wish to have initial data resembling an ultra-relativistic projectile, such as the shock wave metric in AdS. The starting point to construct such initial data is thus the shock wave metric in FG coordinates in Eq. (3.35). Once the function $f(u_{\rm FG})$ is computed, one can proceed to transform the metric to the EF coordinate system (3.38) in which the numerical integration is performed. Taking into account that both the FG and the EF metrics have an explicit Killing vector, one can use the following ansatz for the coordinate transformation between the two frames:

$$\begin{aligned} \mathbf{x}_\perp^{\rm FG} &= \mathbf{x}_\perp^{\rm EF}\,, \\ u_{\rm FG} &= u + \lambda_1(u, t+z)\,, \\ x_+ &= t + z + \lambda_2(u, t+z)\,, \\ x_- &= t - z + \lambda_3(u, t+z)\,, \end{aligned} \tag{3.58}$$

for a left-moving shock [21] while for a shock moving to the right these expressions are:

$$\begin{aligned} \mathbf{x}_\perp^{\rm FG} &= \mathbf{x}_\perp^{\rm EF}\,, \\ u_{\rm FG} &= u + \lambda_1(u, t-z)\,, \\ x_+ &= t + z + \lambda_2(u, t-z)\,, \\ x_- &= t - z - \lambda_3(u, t-z)\,. \end{aligned} \tag{3.59}$$

The differential equations for the transformation functions $\lambda_1(u,z)$, $\lambda_2(u,z)$, and $\lambda_3(u,z)$ are obtained from the change of coordinates, see Eq. (1.12). Equivalently, one can use the fact that the EF coordinate u is a non-affine parameter for ingoing null geodesics

$$\partial_u^2 k^\mu(u) + \Gamma^\mu_{\alpha\beta}\partial_u k^\alpha(u)\partial_u k^\beta(u) = F(u)\partial_u k^\mu\,, \tag{3.60}$$

where $k^\mu(u)$ is the geodesic tangent vector and $F(u)$ is chosen to be $F(u) = \frac{-2}{25u}$. The geodesic equations have the advantage of depending explicitly on $t+z$ and, therefore, its solution reduces to a set of ODEs in u at each point of the coordinate z for $t = 0$. We thus write our initial data for a left-moving shock with width ω and

height $\frac{\mu^3}{\sqrt{2\pi\omega}}$ as

$$h(z) = \frac{\mu^3}{\sqrt{2\pi}\omega} e^{-\frac{(z-z_0)^2}{2\omega^2}}\,, \tag{3.61}$$

$$\mathcal{E}(z) = \mathcal{E}_0 + h(z)\,, \tag{3.62}$$

$$f_2(z) = h(z)\,, \tag{3.63}$$

$$\phi(u,z) = \frac{\phi_0 u_{\rm FG}}{\sqrt{1+\frac{u_{\rm FG}^2}{3\phi_0}\left(\phi_0^3 - 6\phi_2\right)}}\,, \tag{3.64}$$

$$e^{3B(u,z)} = \frac{e^{2a_{\rm FG}(u_{\rm FG})}}{\frac{\partial_z\lambda_1^2}{u_{\rm FG}^2} - \left(\partial_z\lambda_2+1\right)\left(\partial_z\lambda_3-1\right)e^{2a_{\rm FG}(u_{\rm FG})} + \left(\partial_z\lambda_2+1\right)^2 f(u_{\rm FG})h(z)}\,, \tag{3.65}$$

where $u_{\rm FG}$, $\lambda_{1,2,3}$ are functions of u and z obtained from Eq. (3.58). $\mathcal{E}$ is the energy density of the boundary field theory and $\mathcal{E}_0$ the corresponding background value (which we typically set to $\mathcal{E}_0 = 0.02\frac{\mu^3}{\sqrt{2\pi\omega}}$). Having chosen $\mathcal{E}_o$, we know the solution in the absence of shocks (with $B=0$), and its corresponding z-independent ϕ_2 value, the equilibrium value for the specified energy density. With the above construction, we set ϕ_2 to its equilibrium value, for the given background energy density $\mathcal{E}_0$, and a_4 is trivially determined from Eqs. (3.68) and (3.62).

At this point, we have constructed a shock moving in one direction. The contruction of the second shock needs to be done separately because the metric of Eq. (3.38) only described one of the two shocks. The solution for the other shock can be obtained by a mirror reflexion in the collision direction: $z \to -z$ and then we can add the two solutions. We want to construct two shocks than in the boundary are separated but no matter how big this separation is, there is going to be a region in the bulk where the shocks overlap and the superposition is not correct in the sense that it is not longer a solution of the EFEs. In any case, we can always choose a separation large enough for the shocks to overlap beyond the horizon u_h and therefore guarantee that the superposition is correct [21].

3.3.5 Code Convergence and Validation

We have implemented the numerical scheme that we have developed here in a standalone C code. There, we use the GSL library [35] to solve the linear systems of Eqs. (3.40) through a LU decomposition. For the evolution we use a fourth-order Adams-Bashforth method to integrate the functions $B(u,z)$, $\phi(u,z)$, $a_4(z)$, $f_2(z)$ and $\xi(z)$ forward in time, using the procedure outlined in section 3.3.2. The code is trivially parallelised with OpenMP dividing in blocks the z direction.

Numerical simulations using finite differences techniques typically approximate the continuum solution of the problem with an error that depends polynomially on

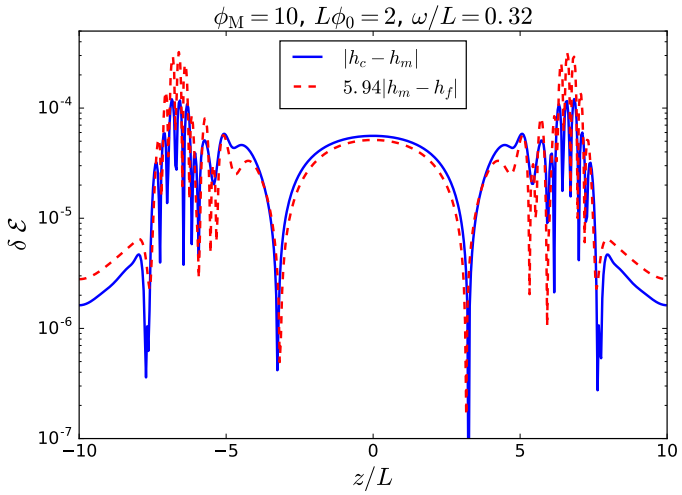

Figure 3.6: Convergence Analysis: A configuration with $\phi_{\rm M} = 10$, $\ell\phi_0 = 2$, $\omega/\ell = 0.32$, $\ell^4\frac{\mu^3}{\sqrt{2\pi\omega}} = 1$ and $\ell^4\mathcal{E}_0 = 0.02$ is evolved until $t = 10\ell$ with three different resolutions in z: $h_c = \ell/20$, $h_m = \ell/30$ and $h_f = \ell/40$. We plot the absolute differences between the coarse and medium resolution (blue solid line) and the medium and fine (red dashed line) resolutions. The latter has been re-scaled by a factor $Q = 5.94$ the one expected for fourth order convergence.

the grid spacing h,

$$f = f_h + O(h^n)\,. \tag{3.66}$$

Different numerical implementations produce different convergence orders, n. In our case, since we make use of fourth order finite difference stencils, we expect to see $n = 4$. One simple way to check the consistency of a code is evolving the same configuration with coarse, medium and fine resolutions, h_c, h_m and h_f respectively. One can then compute a convergence factor using the following expression:

$$Q \equiv \frac{f_{h_c} - f_{h_m}}{f_{h_m} - f_{h_f}} = \frac{h_c^n - h_m^n}{h_m^n - h_f^n}\,, \tag{3.67}$$

where f_h is an arbitrary evolved variable obtained using numerical resolution h in the spatial discretisation. Since in the radial direction we make use of pseudo-spectral methods, which provide exponential convergence, our error is dominated by the resolution used in the z direction, to which the grid spacing h alludes to. In the analysis presented in this section we always make use of the same resolution in the u direction.

We have evolved a configuration with physical parameters: $\phi_{\rm M} = 10$, $\ell\phi_0 = 2$, $\omega/\ell = 0.32$, $\ell^4\frac{\mu^3}{\sqrt{2\pi\omega}} = 1$ and $\ell^4\mathcal{E}_0 = 0.02$. We take resolutions in the z direction: $h_c = \ell/20$, $h_m = \ell/30$ and $h_f = \ell/40$. The convergence factor expected for fourth

order convergence would therefore be $Q \approx 5.94$. The results obtained for the energy density at $t = 10\ell$ can be seen in Fig. 3.6, where the differences $|f_{h_m} - f_{h_f}|$ have been amplified by the factor $Q = 5.94$. The results show fourth-order convergence. We have further verified that the values obtained for our medium resolution run are within $\sim 0.4\%$ of the fourth-order Richardson extrapolated [36] ones, giving us an estimate of the error incurred in the simulation.

3.3.6 Connecting the Gauge Theory with the Shock Wave Evolution

Until now we have developed the full scheme that we need to simulate numerically the shock wave collision in the AAdS gravity theory so we are ready to perform our simulations. However, we can not forget that our goal is to study the gauge theory that lives in the boundary. Therefore, we need to relate the variables of our gravitational shock wave collision with the quantities that we want to study in the gauge theory. For this we use the near-boundary behaviours, Eqs. (3.45), together with the Fefferman-Graham expansions, Eqs. (3.20) and (3.21), to find the coordinate transformation relating the fall-off coefficients. Now, with the expectation values of Eqs. (3.22) and (3.23), we can write the expressions for the gauge theory values in terms of (b_4, a_4, f_2, ϕ_2) as

$$\mathcal{E} = -\left(\frac{3}{4}a_4 + \phi_0\phi_2 + \frac{9 - 7\phi_{\rm M}^2}{36\phi_{\rm M}^2}\phi_0^4\right) , \tag{3.68}$$

$$P_L = -\frac{a_4}{4} - 2b_4 + \frac{\phi_0\phi_2}{3} + \left(-\frac{5}{108} + \frac{1}{4\phi_{\rm M}^2}\right)\phi_0^4 , \tag{3.69}$$

$$P_T = -\frac{a_4}{4} + b_4 + \frac{\phi_0\phi_2}{3} + \left(-\frac{5}{108} + \frac{1}{4\phi_{\rm M}^2}\right)\phi_0^4 , \tag{3.70}$$

$$J_{\mathcal{E}} = f_2 , \tag{3.71}$$

$$\mathcal{V} = -2\phi_2 + \frac{\phi_0^3}{3} - \frac{\phi_0^3}{\phi_{\rm M}^2} , \tag{3.72}$$

where P_L and P_T are the longitudinal and transverse pressures.

3.4 Non-conformal Collisions

In the conformal shock wave model, the physics of the collision only depends on the dimensionless "thickness" $\mu\omega$ [15] of the initial shocks. This is different in the non-conformal case where the physics also depends on the initial transverse energy density in units of the source, μ/Λ. We simulate collisions of $1/2$-shocks and $1/4$-shocks in the terminology of [15] ($\mu\omega = 0.30$ and $\mu\omega = 0.12$, respectively) for several different values of μ/Λ. We then extract the boundary stress tensor and we focus on

its value at the centre, in the z coordinate where the collision takes place as a function of time. We employ as a background a thermal bath with an energy density between 0.8% and 2.5% of the one at the centre of the initial shocks. We simulate each collision with several different regulators and extrapolate to zero regulator. We choose $t = 0$ as the time at which the two shocks would have exactly overlapped in the absence of interactions [15].

We define the hydrodynamisation time, $t_{\rm hyd}$, as the time beyond which both pressures are correctly predicted by the constitutive relations of first-order viscous hydrodynamics [21],

$$P_L^{\rm hyd} = P_{\rm eq} + P_\eta + P_\zeta \,, \tag{3.73a}$$

$$P_T^{\rm hyd} = P_{\rm eq} - \tfrac{1}{2} P_\eta + P_\zeta \,, \tag{3.73b}$$

with a 10% accuracy, so that:

$$\frac{\left| P_{L,T} - P_{L,T}^{\rm hyd} \right|}{\bar{P}} < 0.1 \,. \tag{3.74}$$

In Eqs. (3.73) we have denoted the shear and the bulk contributions to the hydrodynamic pressures by P_η and P_ζ , respectively, which are proportional to the corresponding viscosities. We define the EoSization time, $t_{\rm EoS}$, as the time beyond which the average pressure $\bar{P}$ coincides with the equilibrium pressure within a 10% accuracy, meaning that

$$\frac{\left| \bar{P} - P_{\rm eq} \right|}{\bar{P}} < 0.1 \,. \tag{3.75}$$

On physical ground, we expect that increasing the initial energy in the shocks increases the energy deposited in the resulting plasma and hence the hydrodynamisation temperature of it. We have confirmed that indeed, $T_{\rm hyd}/\Lambda$ increases monotonically with μ/Λ. On the gravity side this means that, for sufficiently large (small) μ/Λ, the horizon forms in the UV (IR) region of the solution, where the geometry is approximately AdS. As a consequence, in these two limits the plasma formation and subsequent relaxation proceeds approximately as in a CFT. In contrast, for $\mu \sim \Lambda$, the relaxation of the plasma takes place in the most non-conformal region where the bulk viscosity effects are the largest. In this intermediate region we see several effects that are absent in a CFT. First, hydrodynamisation times are longer than in a CFT. This is illustrated by the dashed red curve in the left bottom plot of Fig. 3.7 whose maximum, indicated by the second vertical line from the left, is 2.5 times larger than the conformal result, which is indicated by the horizontal line.[2] As expected, at high $T_{\rm hyd}/\Lambda$ we see that $t_{\rm hyd} T_{\rm hyd}$ asymptotically approaches its conformal value (we have checked that at $T_{\rm hyd}/\Lambda = 4.8$

[2]This value differs from the one in [15] because there they used a 20% criterion to define $t_{\rm hyd}$.

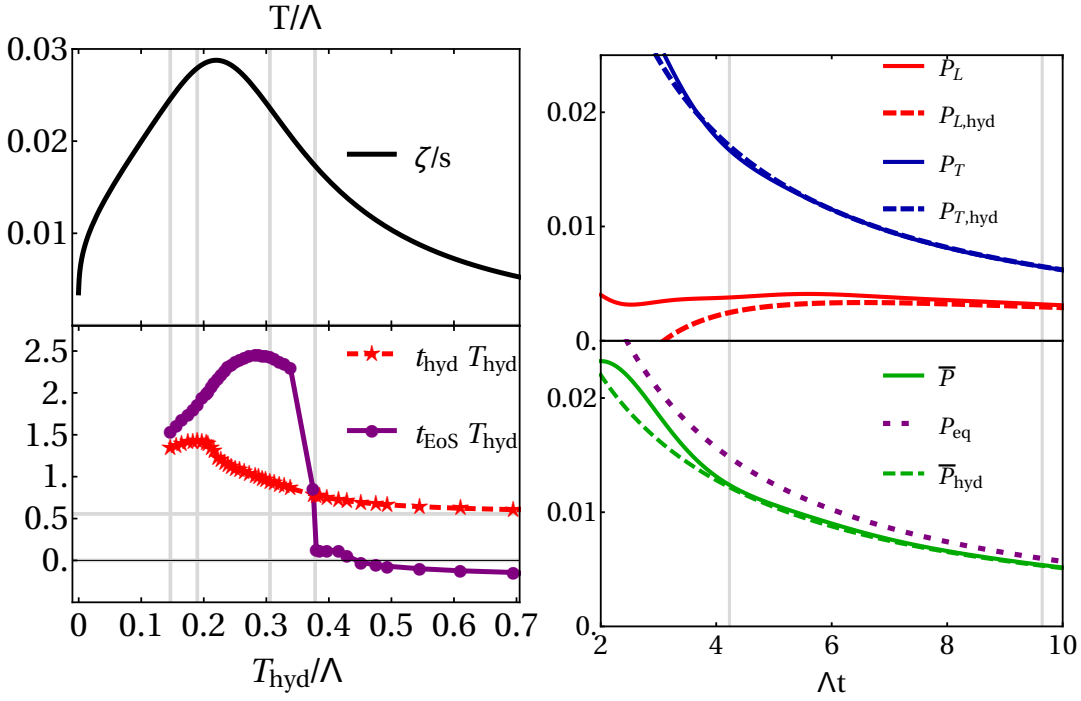

Figure 3.7: Non-conformal Shock Wave Evolution Results:
Left upper plot: Bulk viscosity over entropy density as a function of temperature. **Left bottom plot:** Hydrodynamisation and EoSization times as a function of the hydrodynamisation temperature for collisions of $1/2$-shocks. The vertical grid lines lie at $T/\Lambda = \{0.15, 0.19, 0.31, 0.38\}$ and mark, respectively, the lowest value of $T_{\rm hyd}/\Lambda$ that we have simulated, the maximum of $t_{\rm hyd}T_{\rm hyd}$, the point with the largest ratio of $t_{\rm EoS}/t_{\rm hyd}$, and the intersection between the two curves. The bulk viscosity at these temperatures is $\zeta/s = \{0.025, 0.028, 0.023, 0.017\}$. The top horizontal line indicates the result in a CFT, $t_{\rm hyd}T_{\rm hyd} = 0.56$.[2].
Right upper plot: Longitudinal and transverse pressures with their hydrodynamic approximations, all in units of Λ^4, for a collision of $1/4$-shocks with $\mu/\Lambda = 0.94$. The hydrodynamisation temperature is $T_{\rm hyd}/\Lambda = 0.24$. Because the transverse pressure hydrodynamises much faster than the longitudinal one, P_T and $P_T^{\rm hyd}$ are virtually on top of one another for the times shown.
Right bottom plot: Average pressure with its hydrodynamic approximation and the equilibrium pressure extracted from the equation of state for the same configuration as in the right upper plot. Hydrodynamisation and EoSization take place at $t_{\rm hyd}\Lambda = 4.2$ and $t_{\rm EoS}\Lambda = 9.6$, respectively, as indicated by the vertical lines. At $t_{\rm hyd}$ the difference between $\bar{P}$ and $P_{\rm eq}$ is 18%, whereas the difference between $\bar{P}$ and $\bar{P}_{\rm hyd}$ is 2%. At $t_{\rm EoS}$ the difference between P_L and $P_L^{\rm hyd}$ is 3%. The P_T/P_L ratio is 4.4 at $t_{\rm hyd}$ and 1.9 at $t_{\rm EoS}$.

the difference is 0.5%). We expect the same to be true at low $T_{\rm hyd}/\Lambda$. The increase in the hydrodynamisation time is qualitatively consistent with the increase in the lifetime of non-hydrodynamic quasi-normal modes found in [37, 38, 39, 1]. An heuristic explanation on the gravity side comes from realising that the larger the non-conformality, the steeper the scalar potential becomes. As the plasma expands and cools down, the horizon "rolls down the potential". It is therefore intuitive that steeper potentials make it harder for the non-hydrodynamic perturbations of the horizon to decay. Second, the equation of state is not obeyed out of equilibrium. This is illustrated in the right bottom plot of Fig. 3.7 for a collision of $1/4$-shocks with $\mu/\Lambda = 0.94$, for which the hydrodynamisation temperature is $T_{\rm hyd}/\Lambda = 0.24$. We see that the equilibrium and the average pressures are not within 10% of one another until a time $t_{\rm EoS} = 9.6/\Lambda = 2.4/T_{\rm hyd}$. This is further illustrated in the left bottom plot of Fig. 3.7, which shows the dependence of the EoSization time on the hydrodynamisation temperature for $1/2$-collisions. We see that for sufficiently large μ/Λ the EoSization time becomes negative, meaning that the average and the equilibrium pressures differ by less than 10% even before the shocks collide. The reason is simply that in these cases the energy density in the Gaussian tails in front of the shocks, which start to overlap at negative times, becomes much higher than Λ. At these energy densities the physics becomes approximately conformal and the equation of state becomes approximately valid as a consequence of this symmetry. An analogous argument implies that $t_{\rm EoS}$ should also become negative for collisions with sufficiently small μ/Λ. Third, hydrodynamisation can take place before EoSization. Indeed, we see in the left bottom plot of Fig. 3.7 that $t_{\rm hyd} < t_{\rm EoS}$ for collisions for which the hydrodynamisation temperature is between the first and the fourth vertical line. Comparing with the left upper plot of Fig. 3.7 we see that at these two temperatures the viscosity-to-entropy ratios are $\zeta/s = 0.025$ and $\zeta/s = 0.017$, respectively. Note that the first value of ζ/s would decrease if we were to consider the lower temperature at which we expect that the two curves in the left bottom plot of Fig. 3.7 will have a second crossing. Also, note that the ordering of $t_{\rm hyd}$ and $t_{\rm EoS}$ depends on the accumulated effect of the bulk viscosity along the entire history of the collision. Notwithstanding these caveats, we will take the value $\zeta/s = 0.025$ as a conservative estimate of the minimum bulk viscosity needed to have $t_{\rm hyd} < t_{\rm EoS}$ for $1/2$-collisions. The maximum value of the ratio $t_{\rm EoS}/t_{\rm hyd}$ for $1/2$-collisions is $t_{\rm EoS}/t_{\rm hyd} = 2.56$.

Eqs. (3.73) imply that the hydrodynamic viscous correction to the equilibrium pressure is controlled by the bulk viscosity alone, since

$$\bar{P}_{\rm hyd} = P_{\rm eq} + P_\zeta \,, \tag{3.76}$$

whereas the viscous deviation from isotropy is controlled by the shear viscosity alone, since

$$P_L^{\rm hyd} - P_T^{\rm hyd} = \tfrac{3}{2} P_\eta \,. \tag{3.77}$$

We see from Eq. (3.76) that the reason why hydrodynamisation can take place

before EoSization is because hydrodynamics becomes applicable at a time when bulk-viscosity corrections are still sizeable. This is illustrated in right bottom plot of Fig. 3.7 by the fact that hydrodynamics provides an excellent prediction (within 2%) for $\bar{P}$ at $t_{\rm hyd}$, whereas at this time $\bar{P}$ and $P_{\rm eq}$ still differ by 18%. The above statement is the analogue of the fact that hydrodynamisation can take place before isotropisation because hydrodynamics becomes applicable at a time when shear-viscosity corrections are still sizeable [20]. In our model the bulk viscosity is rather small compared to the shear viscosity, since $\zeta/\eta = 4\pi\zeta/s \simeq 0.35$ at the temperature at which ζ attains its maximum value. Presumably this is the reason why the difference between P_L and P_T at $t_{\rm hyd}$ is much larger than that between $\bar{P}$ and $P_{\rm eq}$.

3.5 Conclusions

In this chapter we have presented the first shock wave collisions in a non-conformal theory [1, 2, 3]. This describes an holographic model for the evolution of plasma in a non-conformal gauge theory. This scheme uses the evolution of two shock waves with a scalar potential in an asymptotically AdS spacetime to obtain the details of the gauge theory in which we want to study the formation of the quark-gluon plasma in the heavy ion collision.

The introduction of the non-conformality implies that the time between the collision and the time when the system can be described by hydrodynamics is longer than in a conformal field theory. Moreover, we have showed that the equation of state is not obeyed outside of equilibrium and that the system can be described by hydrodynamics before the equation of state is fulfilled.

Bibliography

[1] Maximilian Attems, Jorge Casalderrey-Solana, David Mateos, Ioannis Papadimitriou, Daniel Santos-Oliván, Carlos F. Sopuerta, Miquel Triana, and Miguel Zilhão. Thermodynamics, transport and relaxation in non-conformal theories. *JHEP*, 10:155, 2016.

[2] Maximilian Attems, Jorge Casalderrey-Solana, David Mateos, Daniel Santos-Oliván, Carlos F. Sopuerta, Miquel Triana, and Miguel Zilhão. Holographic collisions in non-conformal theories. *JHEP*, 01:026, 2017.

[3] Maximilian Attems, Jorge Casalderrey-Solana, David Mateos, Daniel Santos-Oliván, Carlos F. Sopuerta, Miquel Triana, and Miguel Zilhão. Paths to equilibrium in non-conformal collisions. 2017.

[4] Stephen W. Hawking. Gravitational radiation from colliding black holes. *Phys. Rev. Lett.*, 26:1344–1346, 1971.

[5] Jacob D. Bekenstein. Black holes and entropy. *Phys. Rev.*, D7:2333–2346, 1973.

[6] Jacob D. Bekenstein. Generalized second law of thermodynamics in black hole physics. *Phys. Rev.*, D9:3292–3300, 1974.

[7] Juan Maldacena. The Large N limit of superconformal field theories and supergravity. *Int. J. Theor. Phys.*, 38:1113–1133, 1997.

[8] Steven S. Gubser, Igor R. Klebanov, and Alexander M. Polyakov. Gauge theory correlators from noncritical string theory. *Phys. Lett.*, B428:105–114, 1998.

[9] Edward Witten. Anti-de Sitter space and holography. *Adv. Theor. Math. Phys.*, 2:253–291, 1998.

[10] Carlos A. Bayona and Nelson R. F. Braga. Anti-de Sitter boundary in Poincare coordinates. *Gen. Rel. Grav.*, 39:1367–1379, 2007.

[11] Sebastian de Haro, Sergey N. Solodukhin, and Kostas Skenderis. Holographic reconstruction of space-time and renormalization in the AdS / CFT correspondence. *Commun. Math. Phys.*, 217:595–622, 2001.

[12] Vitor Cardoso, Leonardo Gualtieri, Carlos Herdeiro, Ulrich Sperhake, Paul M. Chesler, et al. NR/HEP: roadmap for the future. *Class. Quant. Grav.*, 29:244001, 2012.

[13] Chun Shen, Zhi Qiu, Huichao Song, Jonah Bernhard, Steffen Bass, and Ulrich Heinz. The iEBE-VISHNU code package for relativistic heavy-ion collisions. *Comput. Phys. Commun.*, 199:61–85, 2016.

[14] iEBE-VISHNU Package. `https://u.osu.edu/vishnu/category/visualization/`, 2015.

[15] Jorge Casalderrey-Solana, Michal P. Heller, David Mateos, and Wilke van der Schee. From full stopping to transparency in a holographic model of heavy ion collisions. *Phys. Rev. Lett.*, 111:181601, 2013.

[16] David Mateos. String Theory and Quantum Chromodynamics. *Class. Quant. Grav.*, 24:S713–S740, 2007.

[17] Jorge Casalderrey-Solana, Hong Liu, David Mateos, Krishna Rajagopal, and Urs Achim Wiedemann. Gauge/String Duality, Hot QCD and Heavy Ion Collisions. 2011.

[18] David Mateos. Gauge/string duality applied to heavy ion collisions: Limitations, insights and prospects. *J. Phys.*, G38:124030, 2011.

[19] Gerard 't Hooft. A Planar Diagram Theory for Strong Interactions. *Nucl. Phys.*, B72:461, 1974.

[20] Paul M. Chesler and Laurence G. Yaffe. Holography and colliding gravitational shock waves in asymptotically AdS5 spacetime. *Phys.Rev.Lett.*, 106:021601, 2011.

[21] Paul M. Chesler and Laurence G. Yaffe. Numerical solution of gravitational dynamics in asymptotically Anti-de Sitter spacetimes. *JHEP*, 07:086, 2014.

[22] Jorge Casalderrey-Solana, Michal P. Heller, David Mateos, and Wilke van der Schee. Longitudinal Coherence in a Holographic Model of Asymmetric Collisions. *Phys. Rev. Lett.*, 112(22):221602, 2014.

[23] Paul M. Chesler and Laurence G. Yaffe. Holography and off-center collisions of localized shock waves. *JHEP*, 10:070, 2015.

[24] Hans Bantilan, Frans Pretorius, and Steven S. Gubser. Simulation of Asymptotically AdS5 Spacetimes with a Generalized Harmonic Evolution Scheme. *Phys. Rev.*, D85:084038, 2012.

[25] Emilia da Silva, Esperanza Lopez, Javier Mas, and Alexandre Serantes. Collapse and Revival in Holographic Quenches. *JHEP*, 04:038, 2015.

[26] Charles Fefferman and Robin Graham. Conformal invariants. *Elie Cartan et les Mathématiques d'aujourd'hui*, page 95, 1985.

[27] Charles Fefferman and Robin Graham. The ambient metric. *ArXiv e-prints*, October 2007.

[28] Luciano Girardello, Michela Petrini, Massimo Porrati, and Alberto Zaffaroni. Novel local CFT and exact results on perturbations of N=4 superYang Mills from AdS dynamics. *JHEP*, 12:022, 1998.

[29] Massimo Bianchi, Daniel Z. Freedman, and Kostas Skenderis. Holographic renormalization. *Nucl. Phys.*, B631:159–194, 2002.

[30] Steven S. Gubser and Abhinav Nellore. Mimicking the QCD equation of state with a dual black hole. *Phys. Rev.*, D78:086007, 2008.

[31] Pavel K. Kovtun, Dan T. Son, and Andrei O. Starinets. Viscosity in strongly interacting quantum field theories from black hole physics. *Phys. Rev. Lett.*, 94:111601, 2005.

[32] Christopher Eling and Yaron Oz. A Novel Formula for Bulk Viscosity from the Null Horizon Focusing Equation. *JHEP*, 06:007, 2011.

[33] Jeffrey Winicour. Characteristic evolution and matching. *Living Rev.Rel.*, 1:5, 1998.

[34] Heinz-Otto Kreiss and Joseph Oliger. *Methods for the Approximate Solution of Time Dependent Problems*. World Meteorological Organization, 1973.

[35] Brian Gough. *GNU Scientific Library Reference Manual - Third Edition*. Network Theory Ltd., 3rd edition, 2009.

[36] Lewis F. Richardson. The approximate arithmetical solution by finite differences of physical problems involving differential equations, with an application to the stresses in a masonry dam. *Philosophical Transactions of the Royal Society of London A: Mathematical, Physical and Engineering Sciences*, 210(459-470):307–357, 1911.

[37] Alex Buchel, Michal P. Heller, and Robert C. Myers. Equilibration rates in a strongly coupled nonconformal quark-gluon plasma. *Phys. Rev. Lett.*, 114(25):251601, 2015.

[38] Romuald A. Janik, Grzegorz Plewa, Hesam Soltanpanahi, and Michal Spalinski. Linearized nonequilibrium dynamics in nonconformal plasma. *Phys. Rev.*, D91(12):126013, 2015.

[39] Alex Buchel and Andrew Day. Universal relaxation in quark-gluon plasma at strong coupling. *Phys. Rev.*, D92(2):026009, 2015.

Chapter 4

Pseudo-Spectral Collocation Methods and Arbitrary Precision

"Fast is fine, but accuracy is everything."

Xenophon

In previous chapters of this thesis, we have seen how spectral methods can be used for solving problems in numerical relativity. Thanks to their high accuracy and their unbeatable order of convergence, they can make a huge difference in the cases where very high precision is needed. For this reason, they are extensively used in different fields of computational science like fluid dynamics, the generation of gravitational-wave templates or weather prediction, see e.g Refs. [1, 2, 3, 4]. In this chapter we go one step further showing that spectral methods can also be very useful when we need to increase the numerical precision of our computations.

In many scientific problems, it is reasonable to assume that 64-bit (double precision) floating point arithmetic, roughly fifteen or sixteen significant digits, is enough to get accurate results. Or even in some cases maybe with 32-bit (single precision), seven or eight significant figures, can be sufficient; but for many another cases this is not true [5]. In systems where long-term solutions depend strongly in the initial conditions or where the physical properties are very sensitive to the value of the parameters, the control of the precision is going to be very relevant. And more important, the lack of capacity of controlling our precision can also lead to unpleasant surprises. The fast convergence of spectral methods makes them one of the best options to go beyond the 64-bit floating point arithmetic. For this precision, maximum accuracy is reached with a very low number of discretisation points and

then it is not that computationally expensive to go further. Also, this means high-compression in the information that we need to store. The number of points, or modes in spectral language, needed to reach very high accuracy is much less than in any other method and the memory demand reduces drastically.

To show these claims, we are going to use a new tool called **ANETO** (Arbitrary precisioN solvEr with pseudo-specTral MethOds) implemented as **C++** templates. This implementation gives us total flexibility and can be used with the faster, highly optimised but limited in accuracy **C++** standard data types like **float** and **double**. In addicion, it can also be used with user defined types like quadruple precision (**float128**) or arbitrary precision ones like **MPFR** (Multiple Precision Floating-Point Reliable) [6, 7]. As the structure of the library is very adaptable, it is easy to build a code on top of it with standard, fast, types and then, once the performance and requirements needed are fully comprehended, translate it to arbitrary precision ones. The library is realised as **Free Software** and can be downloaded at [8] where documentation and examples can also be found. Although we have used **ANETO** only for solving different problems in Numerical Relativity with spherical symmetry, its use can easily be extended to different one-dimensional problems or evolution problems with one space coordinate of different disciplines. Moreover, we think that the conclusions reached here can also be extrapolated to general high precision problems.

4.1 Floating Point Numbers

The representation of real numbers in a manner that computers can understand and calculate with is not an easy problem. Nor it is unique. For integers it is straightforward, the binary representation can be used directly with the precaution of saving one bit for the sign. But if we consider that real numbers have, in principle, infinite digits, the exact translation of the number into bits is going to conditionate not only the performance but also our numerical error. The first thing one can imagine is that real numbers can be approximated by a couple of integers as rational numbers. This way can be very efficient and all the computations have no numerical error but it restricts ourselves to the domain of the rational number and the error is determined by the maximum possible integer that we can expressed. Another approach is to consider a fixed point representation. We take two integers, one representing the integer before the binary point and the other one with the integer after the binary point. Plus one for the sign of course. This has an obvious limitation. The precision in the integer representation limits the maximum and minimum possible values that we can deal with. For example, with a precision of 10^{-10} we can only have numbers with absolute value in the range $(10^{-10}, 10^{+10})$ what would make impossible to deal with problems that have values with different magnitudes. And this is the usual scenario in science. Imagine the simple problem of computing the Newtonian force of the Sun and the Earth in the international system.

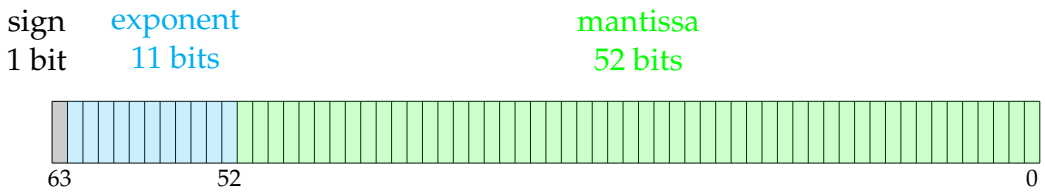

Figure 4.1: Floating Point Internal Representation for Double Precision. The bits in green express the mantissa in 52 bits , usually normalised. The blue, the exponent in base 2 with 11 bits and finally, the last bit indicates the sign. The numbers below represent the indix i of the representation. See Eq. (4.1) for the exact formula.

The mass of the Sun is 10^{+30}, the distance is 10^{-11} and the Newtonian constant is 10^{-23}. To perform this simple computation we would need a precision of $10^{30} \approx 2^{100}$. In other words, around a hundred bits.

Of course we can do better and nowadays all the processors use another representation called *floating point* where the idea is similar to scientific notation. We assign some bits to the significant part, or mantissa, another to the exponent, and of course, again, one for the sign. See Fig. 4.1 for a diagram of it. The number of bits dedicated to the mantissa determine the precision and the ones for the exponent the greatest reachable number and the smallest positive one. For instance, standard single precision (32 bits) reserves 8 bits for the exponent and 23 for the mantissa and for double precision (64 bits) we have 52 bits for the mantissa and 11 for the exponent. If we call b_m to the mantissa bits that are labelled from b_0, the value of a floating point number x is:

$$x = \left(1 + \sum_{i=1}^{b_m - 1} b_i \times 2^{-i}\right) \times 2^E, \tag{4.1}$$

where E is the exponent and we suppose that the numbers are normalised and then $b_0 = 1$, this is equivalent to demand in scientific notation that the mantissa is in the range $[1, 10)$. With this expression we can also comment about the precision that this representation gives us. The gap between 1.00 and the next first floating number is taken as the precision of the machine:

$$\epsilon_0 = 2^{b_m - 1}. \tag{4.2}$$

It can be easily checked that this is not constant in all the range of real numbers. In fact the gap between numbers gets bigger as we move away from $x \approx 1.00$. It can be easily computed that the gap between 2^E and the next one is just:

$$\epsilon_E = 2^E \times 2^{b_m - 1}. \tag{4.3}$$

Data Type	$f(a,b)$
float (32 bits)	1.17260396
double (64 bits)	1.1726039400531787
quad (128 bits)	$1.172603940053178631858834904520 18$

Table 4.1: Rump's Example for Standard Data Types. Evaluation of the expression of Eq. (4.4) for the standard data types. It can be seen that increasing the precision of the computation, the result seems to improve.

Putting some numbers in the case of double precision we have that the machine precision is $\epsilon = 2^{-52} \approx 2 \cdot 10^{-16}$ and the maximum possible number is $10^{1024} \approx 10^{308}$.

Double precision is usually chosen because most of the processors nowadays incorporate a floating point unit (FPU) that performs operations of floating points in 64 bits. Operations of this kind are very quickly but the floating point arithmetic can lead to unpleasant surprises when are performed with a blinded faith. To illustrate one of the issues that can arise in the numerical computations we review Rump's example [9]. Let us consider the expression:

$$f(a,b) = (333.75 - a^2)\, b^6 + a^2(11\, a^2\, b^2 - 121\, b^4 - 2) + 5.5\, b^8 + \frac{a}{2b}, \tag{4.4}$$

that we evaluate for the values $a = 77617$ and $b = 33096$ using standard data types that are shown in Table 4.1. These results indicate that increasing the precision, the same number is obtained with more significant digits and therefore we can say that we have obtained a good approximation of $f \approx 1.17260394005$ and that our computation is correct. This should be the end of our discussion but it was observed that the case was more complicated. Let us evaluate the same expression with the MPFR library [6, 7] that allows us to choose the number of bits of our floating point numbers and hence the digits of precision. The results obtained can be seen in Table 4.2. For low number of bits, until 24, the behaviour of f is difficult to explain. The evaluation failed and compute in some cases very large numbers that does not correspond with the correct value. These results are mixed with the same value that we have computed with the standard ones and that we supose it is the correct one. From 28 to 36 bits this value stabilises so it could seem that is the correct one. The surprise come after 40 bits of precision. Then, we obtain a complete different value of $f \approx -0.82739605994682$ that appears to be correct even when computing with 150 precision bits.

To analise what happens we need to realise that the values of a and b chosen fulfil the equation:

$$a^2 = 5.5b^2 + 1, \tag{4.5}$$

Precision bits	$f(a,b)$
4	$6.4904\ 10^{+32}$
6	1.172604
8	$-7.92281625\ 10^{+28}$
12	$9.671406556917\ 10^{+24}$
16	$-5.9029581035870565\ 10^{+20}$
20	1.17260394005317863186
24	$8796093022209.172603940053$
28	$1.17260394005317863185883490452018$
32	$1.17260394005317863185883490452018$
36	$1.17260394005317863185883490452018$
40	$-0.82739605994682136814116509547981629199906$
44	$-0.82739605994682136814116509547981629199033112$
48	$-0.82739605994682136814116509547981629199033115784839$
52	$-0.82739605994682136814116509547981629199033115784384819916$
56	$-0.82739605994682136814116509547981629199033115784384819916$
60	$-0.82739605994682136814116509547981629199033115784384819916$
100	$-0.82739605994682136814116509547981629199033115784384819916$
150	$-0.82739605994682136814116509547981629199033115784384819916$

Table 4.2: Rump's Example for Different Bit Precision Using MPFR. Evaluation of the expression of Eq. (4.4) for different bit precision. The behaviour of the obtained value is more difficult to explain. Until 24 bits, the evaluation failed computing in some cases very large numbers that does not correspond with the correct computation. These results are mixed with the same value that we have computed with the standard ones and from 28 to 36 bits the previous value seems to stabilised. The surprise is that after 40 bits of precision, we obtain a complete different value that this time does appear to be correct.

from where it is obvious that the higher order terms of Eq. (4.4) cancel and it reduces to:

$$f = \frac{1}{2b} - 2 = -0.82739... \tag{4.6}$$

The problem now is clear. An analytical cancellation need to happen to get the correct result and numerically this is done properly only when a very high number of bits is used. This exposes the fact that the control in the expressions that we use is fundamental in order to avoid numerical instabilities. A proper identification of the terms where a cancellation of this kind can happen is always a good practice that allows us to deal with them. Sometimes is enough with a clever rearranging of the expressions, controlling the rounding mode or using higher precision just for this difficult terms. The lesson of this simple example is that dealing with floating-point arithmetic can be very problematic sometimes and that having a full control of the numerical precision can help to detect instabilities. It is also very important to notice

that precision convergence does not guarantee at all that our computation is correct.

Current processors incorporate a FPU unit that allows to compute operations with floating point numbers, usually 64 bit. Therefore, the algorithms working in this precision are going to be the fastest ones[1]. Going further than this is going to require a software layer that makes the code to run slower. This is studied and discussed in Sec. 4.3.2.

4.2 ANETO Library Structure

All of the tests that we have done to study the use of PSC methods for arbitrary precision are going to be implemented using the **ANETO** library. This is implemented as **C++** templates and it can use it with any data type available. The library is release as Free Software and be found and downloaded at [8]. In that website, apart from the source code that can be taken and reused, there is a full documentation of the classes and functions available as well as examples of its functionalities. The features of the library can be applied with two different classes. One is **spectral_grid<>** and generate an individual Lobatto-Chebychev grid. The other one is **multidomain<>** and generates a mesh composed by several Lobatto-Chebychev domains. All the details of the grid and the PSC methods are explained in Sec. 1.3. In this section we are going to go over the main functionalities of both classes.

4.2.1 Class Spectral Domain

The class **spectral_grid<>** generates a *Lobatto-Chebyshev* grid defined in $X = [-1, 1]$ of N points. A function discretised using PSC methods is defined by its value in the collocations points of the grid in what we call the *physical representation*. In general the information of the function is stored in this representation but usually the internal operations are performed used the *spectral representation*, the coefficients of the expansion in Chebychev polynomials. The grid that we have introduced makes the transformation between the two straightforward using a discrete cosine transformation (DCT). The library can performed this through a matrix transformation, that scales as $\sim N^2$ or using a fast Fourier algorithm (FFT), that scales as $\sim N \log N$ and it is included through the Eigen library [10]. The last one is optimised for the case in which the number of points is a power of two, and therefore the recomended use, that is the default one, is to use the FFT in these cases and the matrix transformation otherwise. The main operations that the spectral domain class can perform are:

[1]Here we do not consider optimisations done for lower bit precision data types like vectorisation because double precision is the minimum that we are interested in.

Indefinite Integrals: The class can perform indefinite integrals. It takes the value of a function in the collocation points and return the value in the collocation points of the accumulative integral compute from the left boundary, $X_- = -1$ or from the right boundary $X_+ = +1$. The arbitrary integration constant can be specified as the value in one of the boundaries. The exact expressions are:

$$I_L(X) = I(X_-) + \int_{X_-}^{X} dX'\, f(X'), \tag{4.7}$$

$$I_R(X) = I(X_+) + \int_{X}^{X_+} dX'\, g(X'), \tag{4.8}$$

and for details Eqs. (1.115) and (1.120) in Sec. 1.3.1 can be checked.

Derivatives: It can also perform the derivative of a given function:

$$d(x) = \frac{df(x)}{dx}, \tag{4.9}$$

the details of the produce are in Eq. (1.111) of Sec. 1.3.1 .

Interpolation: One of the highest benefits of the use of spectral methods is the accuracy of the interpolation obtained inside a domain, check Sec. 1.3.1 for details. This is done using the spectral representation:

$$y = \sum_{n=0}^{N} \boldsymbol{a}_n(t)\, T_n(X), \tag{4.10}$$

check Eq. (1.104) for details. The class computes the value of the function in any interior point of the domain. Once they are computed, the spectral coeffients are stored inside the class so they can be used afterwards to get values of the function in other interior coordinate without recomputing the spectral coeeficients This can be done not only for the funciton values but also for the first and second derivatives.

Root Finding: The accuracy of the interpolation inside a domain of the PSC methods makes it very efficient and accurate the use of algorithms for root finding:

$$f(X_R) = f_R.$$

In the library it is implemented an iterative Newton's method to find the root until the precision of the datatype used is reached. If no root is present in the domain, the function will return the closest value and if there is more than one, just one of them it is returned.

4.2.2 Class Multidomain

The **multidomain<>** class generates a multidomain structure with the number of domains and points per domain specified. The distribution of the domains can be set to be uniform or to specify the bondaries of them to generate a more adapted mesh. The **multidomain<>** class manage the internal operations of the different domains and once it is created, the main features can be accessed without noticing the internal structure.

Indefinite Integrals: The class extends the indefinite integrals mentioned in the spectral domain class but in addition to it we extend the possibility to specify the boundary condition in an arbitrary interior point x_C:

$$I_C(x) = I(x_C) + \int_{x_C}^{x} f(\tilde{x})d\tilde{x} \tag{4.11}$$

Derivatives: For the computation of the derivative one can choose to perform normal derivatives or the dual grid scheme defined in Eq. (1.128) of Sec. 1.3.2. This second option allows to improve a lot the derivative accuracy in the points near the domain boundaries.

Interpolation: The interpolation function just expands the functionalities of the spectral grid interpolation adapting it to the multidomain structure.

Root Finding: In the multidomain, it has been added two important cases of root finding one for monotonic increasing functions and another one for monotonic decreasing functions. In both of them the root, if it exists, will be unique. If there is no root in the whole computational domain, the function will return an error. For general functions, we can find the root indicating the domain where we think the value we are looking belongs to but the result it is not checked returning the closest value if there is no root in the domain.

4.3 Library Performance

In this section we check the performance both in accuracy and speed of several of our library routines. For the following test, we use either standard types as **float** and **double**, also the **quadruple precision type**[2] and the general datatype where we can choose the bit precision: the GNU's MPFR [6] with a C++ wrapper [7].

[2]The quadruple precision is based on the float128 type in Boost Multiprecision library

4.3.1 Integrals

As a test function for the integrals routines, we are going to take a simple cosine function:

$$f(x) = \cos(x), \tag{4.12}$$

to which we consider the integration over a spectral domain. As it can be seen in the left plot of Fig. 4.2, for this simple example as long as you have enough points in your grid, the error should scale with the round-off error fixed by the number of significant digits that is essentially $\lceil \text{bits} \cdot \log_{10}(2) \rceil$. This is true even for a low number of points as $N = 47$ until 260 precision bits where the error saturates because of the discretization error is more important than the round-off. It is enough to use $N = 71$ to decrease the error easily up to 10^{-120}. Using the multidomain with only four domains and 23 and 47 points per domain structure, the same behaviour is observed in the right plot of Fig. 4.2. For the first case the discretisation error is reach around 10^{-50} but for the second one we easily reach again 10^{-120}. The horizontal lines show the round-off error with the single, double and quadruple precision respectively that are much higher than the error we can reach using arbitrary precision.

Notice that thanks to the exponential convergence of spectral methods is very easy to obtained very small error with a low number of points. In the previous example with less than two hundred points we can reach an incredible small numerical error. Although the integral was done for simple function very well adapted to the method, the same is true whatever is the integral to compute, assuming that our functions are smooth. In the previous figure it seems that in the multidomain approach needs the total number of points to be higher to get the same error but in the general case a multidomain can be faster, more flexible and better for other operations.

4.3.2 Double Precision versus Arbitrary: Computational Time

In the previous section we have seen how the use of arbitrary precision can be extremely useful for obtaining better accuracy. We emphasise this property in the following sections but first we need to consider the drawbacks of its use. Most of the available computers nowadays use a 64-bit processor and the use of double precision is highly optimised to work there. The approach to go beyond this precision requires a software implementation that slows down the computation.

We use the test case of Eq. (4.12) to quantify this effect for three different grid configurations that can be seen in Fig. 4.3. In the plot, we show how much slower is the use of MPFR compared with the computational time used by the standard double precision. In the range analysed, until 512 bits or around 150 significant digits, the computational time seems to increase linearly, being a factor 150-300 times slower than the double case. This is even worse if we consider that to take

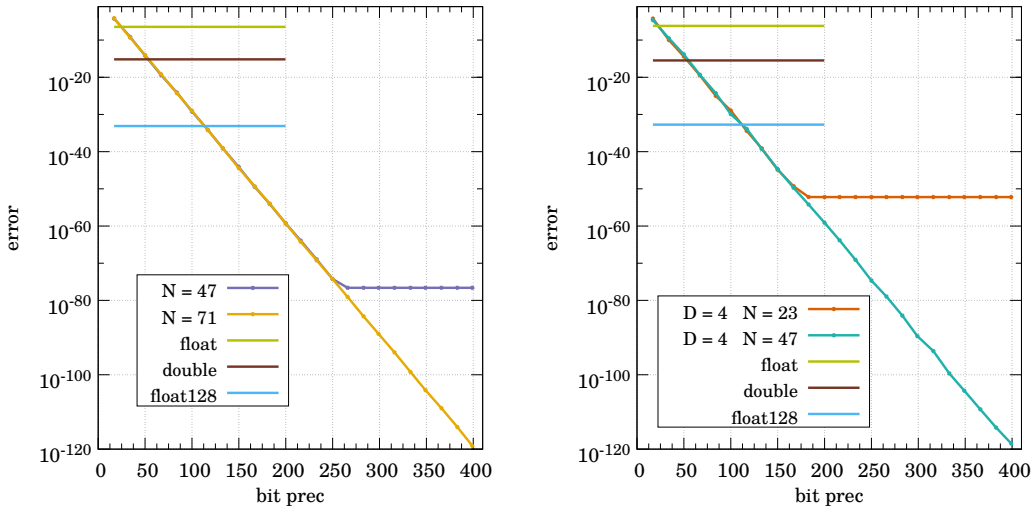

Figure 4.2: Maximum Error of a Test Integral for Different Bit Precision. The left plot shows the error of the integration routine on the spectral grid and the right one in the case of the multidomain grid. In both cases, the points show the error of two different grid configuration respect to the bit precision and the horizontal lines correspond to the error for single, double and quadruple precision.

advantage the significant digits we need to increase the number of domains/points. This is something that we need to take in consideration before the use of any kind of arbitrary precision.

Looking at Fig 4.3, it is also worth mentioning the small jumps in the computational time. Although the general behaviour is linear, at small scales the function is more or less flat, increasing in multiples of 64 bits. This is not surprising because the tests have been done using a 64-bit processor and is related with the way the MPFR library uses double precision numbers to stored the arbitrary floating points variables.

4.3.3 Parallelization with OpenMP

In the previous subsection we have seen the main problems of the use of arbitrary precision: speed. As the current processors are designed for 64-bit precision computations, all the arbitrary precision libraries emulate this using symbolic calculations or a software layer to compute the arbitrary precision operations. Both options slows the computation, in our case around 150-300 times. In order to overcome this drawback, we are going to show that some kind of parallelism can help us a lot. The use of parallel computing adapts perfectly to our multidomain scheme because most our computations are done independently in each of the

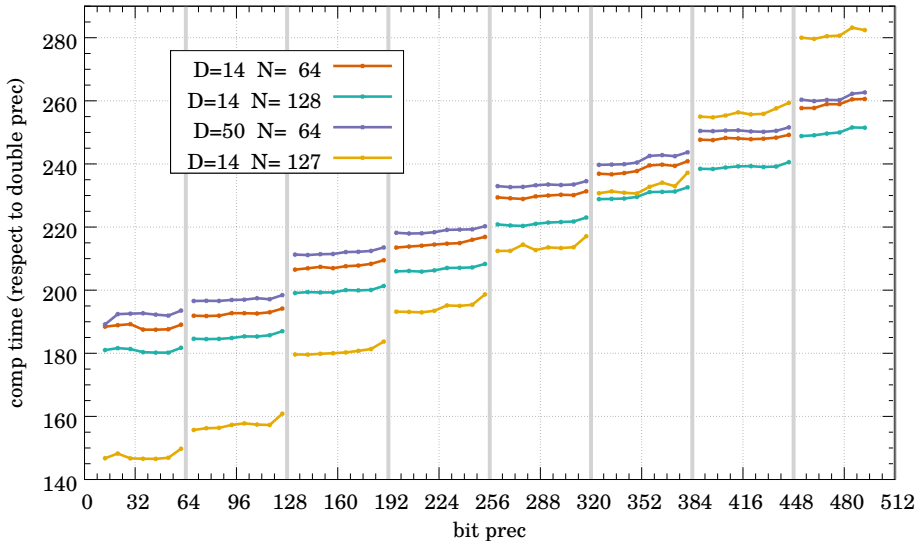

Figure 4.3: Computational Time of MPFR's Arbitrary Precision. The plot represents the computational time for the test integral presented in section 4.3.1 at three different grid configurations. All the times are normalise with the time of the double precision operation of this grid. In the general scale the computational time seems to be linear with the bit precision. The vertical lines separate multiples of 64 bits. The computational time essentially increases in these boundaries. The runs with 64 and 128 points per domain are done via FFT and the one with 127 with matrix transformation. Notice that higher does not mean greater absolute computational time. All the simulations with (14,127) domains/points are much slower than the ones with (14,128).

domains.

The shared-memory OpenMP [11] is the simplest option to show the possibilities of the parallelization because we can profit of the independence of our domains without adding any communication overhead. In Fig. 4.4 we show a measure of the computational time speedup(S_p) as we increase the number of OpenMP cores. This is defined as:

$$S_p = T/T_p, \tag{4.13}$$

where T is the time used by a sequential computation and T_p is the time of a computation that uses p cores. Of course, the ideal unreachable limit is $S_p = p$ as it is shown as a dash line in the plot and our goal is to get as close as we can to it. We have performed tests for the integral and the derivative for double precision and float128, quadruple precision, where we see that we are very close to the maximum speed-up. It is also interesting to notice that the derivative are closer to full parallelism. This is expected as this operation is fully independent in each of the domains while in the case of the integrals we need to communicate partial integrals. Anyway, in all the

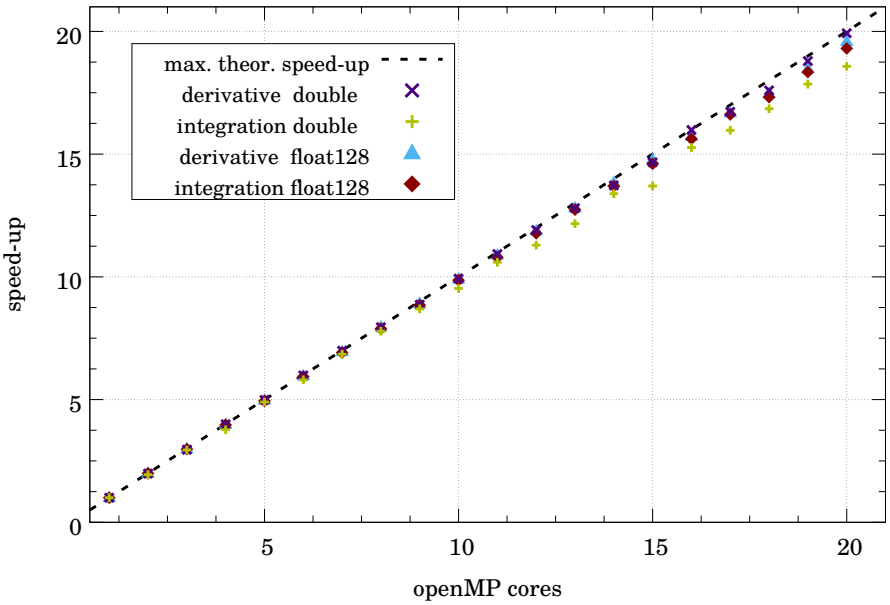

Figure 4.4: Speed-up with OpenMP in Multigrid Routines. The plot represent the speed-up at integral and derivative routines for double and quadruple precision. Derivatives present a better speed-up but both cases show that multidomain is a very good option for parallelization.

cases the final behaviour is more than reasonable.

What we have discussed in this section is parallelization at the level of the multidomain. This is very helpful for speedup the computation but still it does not address the key problem. The computational time increases because what before was fundamental operation, it is not anymore. A different approach is to look the parallelism in the fundamental operations of arbitrary precision. This is already investigated in some projects like [12] where they use CUDA to compute basic operation. This approach can be very useful when we use higher precision computations.

4.3.4 Multidomain Derivatives: The Dual Grid

The computation of derivatives at points near the domain boundaries tends to accumulate a big error that can be one or two orders of magnitude higher than in the central region of the domain. And this phenomenon is worse with a high number of collocation points in a domain. As we commented in Secs. 1.3.2 and 4.2.2, we can deal with it creating a dual grid structure as the one presented in Fig. 1.6. For this example, we take a Gaussian function as a test function and a partition function

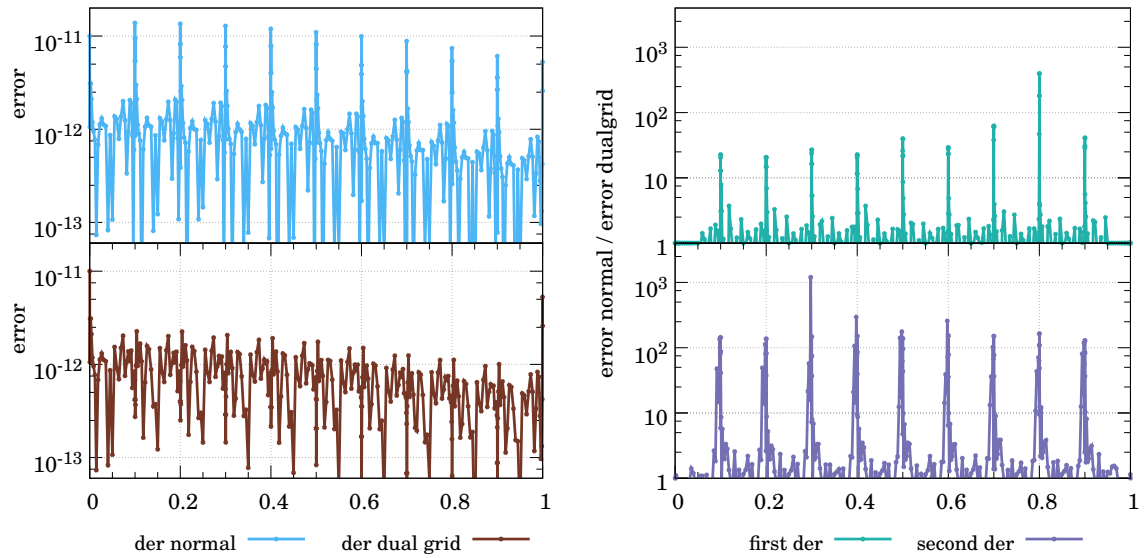

Figure 4.5: Dual Grid Derivatives. The left plots shows the error for the first derivative computed with the dual grid setup (left bottom) or without it (left top). it can be seen that in the domain boundaries there is a huge reduction of the error. The magnitude of the improvement can be seen in the top right plot. The quotient of the error in both cases quantifies the improvement in the points near the boundaries between one and two orders of magnitude. The bottom right plot shows the same for the second derivative where the improvement increases from two to three orders of magnitude.

defined by:

$$\pi(x) = \frac{(x - x_L) \cdot (x - x_R)}{(x - x_L) \cdot (x - x_R) + (x - \bar{x}_L) \cdot (x - \bar{x}_R)}, \tag{4.14}$$

where the bar indicates the boundaries of the dual grid.

In the left top plot of Fig. 4.5, the error of a derivative computed in one grid of ten domains is shown. Here, it is very easy to notice where are the boundaries of these domains as the error have a peak of more than one order of magnitude in most of the cases. The brown line of the left bottom plot shows the error when we do the same computation with the dual grid scheme. The peaks disappear completely and the error in the derivative is now very flat. This improvement can be seen on the right top plot where we present the quotient between the error of the derivative computed with and without the dual grid. Near the boundaries we refine our computation between one and two orders of magnitude. Doing the same for the second derivative (right bottom plot) the enhancement is even better with all the boundaries reducing the error in two/three orders of magnitude.

4.4 Applications to Numerical Relativity

The main methods presented here and the interest of exploring arbitrary precision come from the previous work about the gravitational collapse of scalar fields in Anti-de Sitter (AdS) that was presented in Chapter 2 and published in Refs. [13, 14]. In this section we improve the two schemes that we use there, specially the characteristic one. Thanks to a different coordinate system and a small change in the computation of the metric variables, we have been able to incorporate the PSC method to the impletation of this formulation.

4.4.1 Gravitational Collapse

We start reformulating the problem of gravitational collapse in characteristic coordinates. This was introduced in Sec. 2.1 and we used the characteristic formulation in AdS spacetimes in Secs.2.3.2 and 2.4.3. We rewrite our original characteristic formulation [15, 16, 17, 18] using now a double null metric. For simplicity we deal with the case of zero cosmological constant but the difference with AAdS is very small. The line element is:

$$ds^2 = -2f(u,v)\, r_v(u,v)\, du dv + r^2(u,v) d\Omega^2, \tag{4.15}$$

where f and r are two arbitrary functions of (u,v) and r_v is the partial derivative of r with respect to the coordinate v. The idea of a double-null folation is to take both directions of the propagation of light rays as coordinates. In Fig. 4.6 an scheme of this idea can be seen for the case of an empty spacetime. In our case, the spacetime is curved by the presence of the scalar field so (u,v) would not be perpendicular to the (t,r) coordinates.

With the intention of reducing the order of the system and to separate variables we introduce the following new variables for the scalar field:

$$\begin{aligned} h &= \frac{(r\phi)_v}{r_v} \\ \bar{h} &= \phi, \end{aligned} \tag{4.16}$$

and also a new metric variable:

$$\bar{f} = -2r_u. \tag{4.17}$$

With this new variables, from the vv and the uv components of the EFEs we get two equations:

$$\begin{aligned} f_v &= \frac{f\, r_v}{r}(h-\bar{h})^2 \\ \bar{f}_v &= \frac{r_v}{r}\left(f-\bar{f}\right) \end{aligned} \tag{4.18}$$

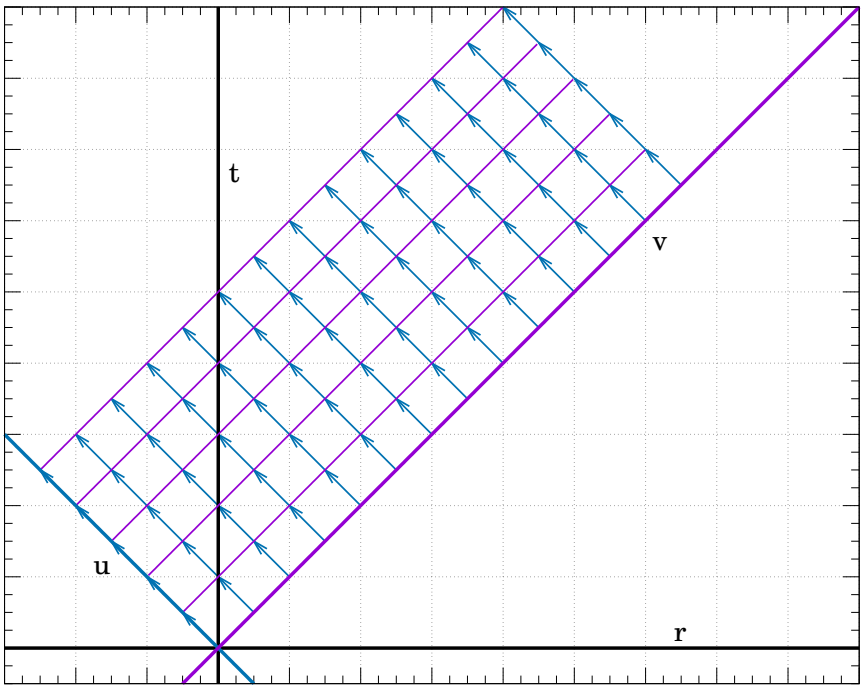

Figure 4.6: Scheme of an Evolution in Double Null Coordinates. The horizontal and vertical lines are the axis of the (r,t) coordinates. We set our initial conditions in a u =const (wide purple) and evolve each point of the grid following the arrows. This scheme is true in the case of an empty spacetime where null coordinates form 45 degrees with (r,t). In a general case, the (u,v) coordinates will be curved but the idea is the same.

We prescribe initial conditions in the profile $h(v)$ in an initial u=const and then we compute all the needed information with the expressions:

$$\begin{aligned} \bar{h} &= \frac{1}{r}\int_{v_0(u)}^{v} h\, r_v dv \\ f &= f(v_0)\exp\int_{v_0(u)}^{v} \frac{r_v}{r}(h-\bar{h})^2\, d\widetilde{v} \\ \bar{f} &= \frac{1}{r}\int_{v_0(u)}^{v} r_v f\, d\widetilde{v} \end{aligned} \tag{4.19}$$

where v_0 is the value of v where $r = 0$ and for regularity at this point we impose $\bar{h}(v_0) = h(v_0)$ and $\bar{f}(v_0) = f(v_0)$. The last expression can be rewritten by using

integration by parts as:

$$\bar{f} = f - \frac{1}{r}\int_{v_0(u)}^{v} r_v f (h-\bar{h})^2 \, d\widetilde{v}. \tag{4.20}$$

Once we have all the information in one u =const, we evolve the field using the conservation of the stress-energy tensor:

$$h_u = \frac{1}{2\,r}(f-\bar{f})(h-\bar{h}) \tag{4.21}$$

and also from Eq. (4.17) and 4.18 we can obtain the other evolution equations:

$$\begin{aligned} r_u &= -\frac{1}{2}\bar{f}, \\ (r_v)_u &= -\frac{1}{2} r_v \left[\frac{f-\bar{f}}{r}\right]. \end{aligned} \tag{4.22}$$

The only piece missing in the scheme is the $f(v_0)$ that appears in Eqs. 4.19. This indicates a residual *gauge* freedom about the change in the coordinate v thought hypersurfaces of u =const. In practice, this is going to fix how the origin $r = 0$ moves in the (u, v) plane. Considering v_o, the coordinate of the origin, its trajectory can be computed with:

$$\frac{dv_o(u)}{du} = \left.\frac{f_o}{2r_v}\right|_o, \tag{4.23}$$

so we are going to take $f(v_0) = 2\, r_v|_o$ and then the origin moves as:

$$v_0(u) = v_o(u_0) + u. \tag{4.24}$$

We prescribe a Gaussian as initial condition in the scalar field:

$$h(u_0, v) = \epsilon \;\; e^{\frac{(v-b)}{\omega^2}}, \tag{4.25}$$

where we select $\epsilon = 2.00$, $b = 0.15$ and $\omega = 0.05$, a configuration above the critical threshold and therefore that will form an AH. The evolution is performed with an standard Runge-Kutta 4 algoritm. In our coordinates, the presence of an AH will be noticed by the condition $r_v \to 0$ or, equivalently, $\bar{f}/f \to 0$. This limit is not reachable in our coordinates but we assume the AH forms when these quantities reach a value less than 10^{-8}. At this point, we stop the simulation and we analyse the solution.

Using the spectral representation, Eq. (1.104), the error can be estimated from the absolute value of the last spectral coefficient. The value of the coefficients a_i decay exponentially, reaching or not the round-off error. If round-off is not reached, the

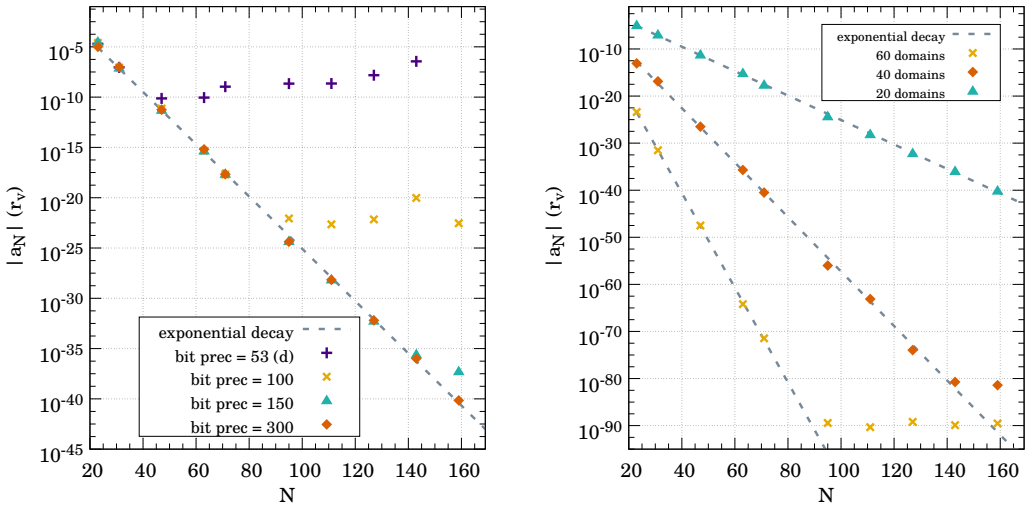

Figure 4.7: Convergence of the Position of the AH Formation: The left plot shows the truncation error (estimated from last spectral coefficient) at the moment of AH formation for several different grid configurations, all of them with 20 domains. Each data set corresponds to simulations done with different bit precision. The error decays exponentially (spectral convergence) until maximum precision is reached. On the right we see the impact of having more domains added. All sets of data have spectral convergence but the number of domains has an impact in the α factor of the exponential decay $e^{-\alpha N}$. These simulations are done with 300 bit precision.

last spectral coefficient represents an estimation of the truncation error for ignoring the rest of terms of the spectral series. Otherwise, if the last coefficient is the round-off error the last coefficient represents the precision reached. In both cases, it can be used for a good estimation of the error.

In Fig. 4.7 we show this error at the end of the evolution for the case presented. As we have different errors at each domain, we consider the highest of all of them that corresponds with the domain where the collapse is taking place. In that figure we only show the error of the function r_v because is the one that have the highest error of all the three evolution variables.

Moreover, in the left plot of Fig. 4.7, we use a setup with twenty domains and we change the number of points for different bit precision. In all the cases, the error has an exponential decay (spectral convergence), notice the log scale in the y axis, until the reach of the precision limit that, of course, improves as we increase the number of bits of our data types. The first one represents a 53 bit precision equivalent to the double standard and allows us to get a maximum precision of 10^{-10}-10^{-11}. Notice that this is few orders of magnitude above the theoretical limit of sixteen digits, but

this is not strange considering that during the evolution noise is going to pile-up reducing our maximum precision. In addition, the number of domains used in our test evolution is not optimal. This is just a comparison of the same exact scheme for several bit precisions. Increasing the number of significant bits we improve the maximum error and with 150 bits (around 45 significant digits) we easily decrease the error up to almost 10^{-40}.

In the right plot of Fig. 4.7 we study the influence of the number of domains in the error. If we change the number of points per domain keeping the number of domains constant, the error presents an exponential decay $\Delta r_v \approx \exp(-\alpha N)$. Varying the number of domains changes the factor of the exponential decay α. In this case we can reach the minimum error adding domains with less points per domain. This can be a good idea considering that adding domains has, in general, a linear impact on the computational time while increasing N has an impact of $N \log N$ or N^2 according if the operations in the spectral domain are performed with FFT or with matrix transformations.

4.4.2 (in)Stability in Anti-de Sitter Spacetimes

In this section we recover the Cauchy evolution in Anti-de Sitter spacetimes as it was presented in Secs. 2.3.1 and 2.4.1 and adapted in a simplified version for arbitrary precision. In Chapter 2 it was shown that a perturbation in AdS has no mechanism to disperse and must bounce in the boundary several times before it becomes compact enough to collapse. Some stable configurations have been found for some cases but the exact meaning of these is still under debate. In order to study these cases, long and accurate evolution are needed. In this section we present a test case where we evolve one of these configurations during two bounces and compare the accuracy obtained using double precision and 300 bit precision.

We solve the EFEs as in the previous section but this time we consider the spacetime metric of Sec. 2.3.1:

$$ds^2 = \frac{\ell^2}{\cos^2 x}\left(-Ae^{-2\delta}\,dt^2 + \frac{dx^2}{A} + \sin^2 x\, d\Omega_2^2\right), \tag{4.26}$$

where $A = A(t, x)$ and $\delta = \delta(t, x)$ are two arbitrary functions, t is the time coordinate and x is a compactified spatial coordinate where the AdS boundary is located at $x = \pi/2$. The full equations of this example can be found in Sec. 2.3.1

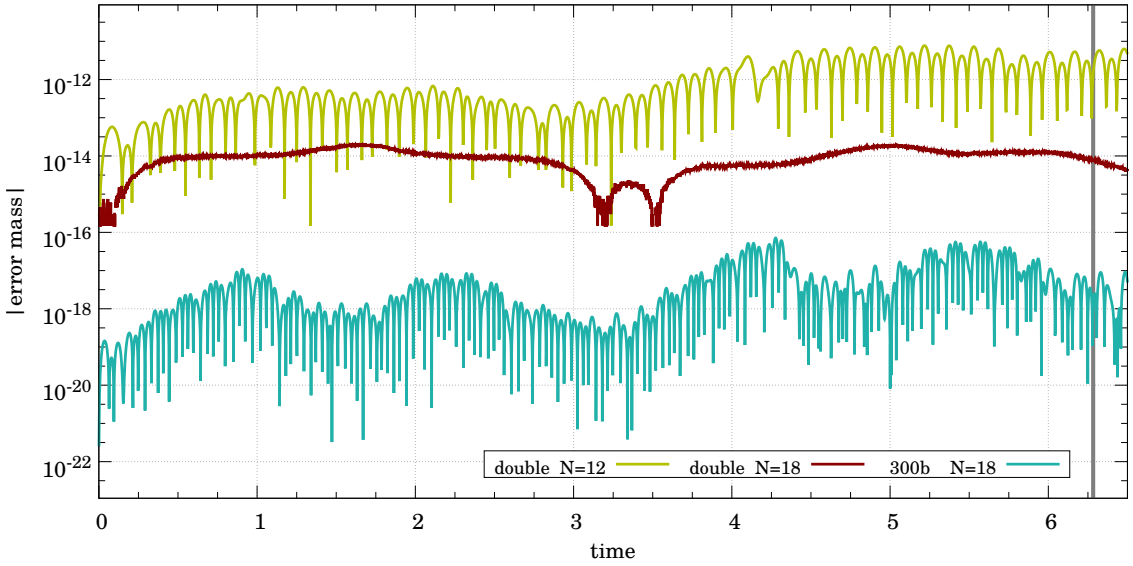

Figure 4.8: Mass Error During an Evolution in AAdS Spacetimes. We compare three different grid/precision configurations with ten domains. Using double precision, the use of N=18 points per domain (red line) is enough for reaching the round-off error. The same number of points with 300-bit precision (turquoise line) allows us to reduce a few orders of magnitude the error during the evolution. It is interesting to notice how, when the error is determined by the discretization error, several fluctuations are present while in the one determined by round-off the error remain very flat during the time evolution. The grey vertical line shows the instant of time at which we measure the error for the study of Fig 4.9 .

To see how the use of arbitrary precision can help in this case we take a initial perturbation similar to a Gaussian function centred at zero:

$$\begin{aligned} U(t_0, x) &= \epsilon \exp\left(-\frac{4\tan^2 x}{\pi^2 \sigma}\right), \\ V(t_0, x) &= -U(t_0, x), \end{aligned} \tag{4.27}$$

with $\epsilon = 2.0$ and $\sigma = 0.4$. We set up a multidomain grid of ten domains and we change the number of collocation points per domains to see how the error changes according to this for both double precision and for a 300-bit MPFR variable. We evolve this initial perturbation during the time corresponding off two bounces in the boundary. As we need a very precise time evolution, we use a sixth order Runge-Kutta 10,6(7) (see Refs. [19, 20] for details). This algorithm uses ten intermidiate steps to generate a sixth order time integration with the seventh order as stimation of the error.

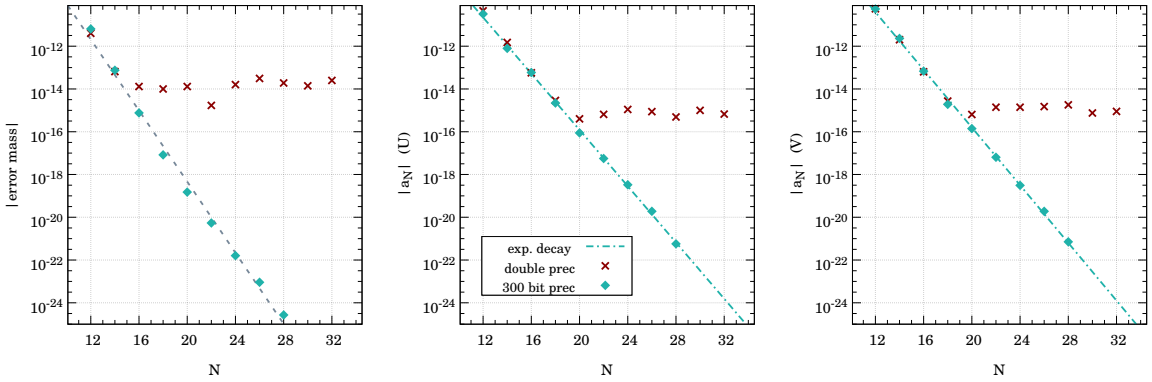

Figure 4.9: Convergence of the Error in AdS Evolutions. The figure shows how we can control the error in the AAdS evolution using double (red points) or 300-bit precision variables (turquoise ones). The plots represent the normalise mass error (left) and the truncation error of U (centre) and V (right) with respect of the number of collocation points per domain. This information is measured at the same time ($t = 6$) after two bounces in the boundary for grid configurations with ten domains.

At any time step, we can compute the energy contained inside a sphere of a given compactified radius x, which we call the mass function:

$$\mathcal{M}(t,x) = e^{\delta} \int_0^x dy\, e^{-\delta} \sin^2 y \left(\frac{U^2 + V^2}{2} \right) , \tag{4.28}$$

and then the total energy contained in the spacetime is $M(t) = \mathcal{M}(t, \pi/2)$. Its conservation can be controlled by using a mass error function defined as:

$$\Delta M(t) = \frac{|M(t) - M(t_0)|}{M(t_0)} . \tag{4.29}$$

In Fig. 4.8 we present the evolution of this mass error function. The purple line shows an evolution with a low number of points ($N = 12$) with double precision. The error oscillates in the range $10^{-12} - 10^{-11}$. Increasing the number of points, in the plot we have considered $N = 18$, we can decrease the mass error down to around 10^{-14}. It is interesting to notice the different behaviour between the two lines. In the first case there is plenty of oscillations and we consider the error as the maximum value of those. This is because here the error is determined by the discretization error in such a way that the total error can oscillate between the discretization and the round-off errors. In the second case we have, by far, reached the round-off error and the profile is very flat and, of course, it can not be improved by using double precision. Just changing from double precision to 300-bit precision variables with

the same number of points per domain, the error drops more than two orders of magnitude and, again, it is determined by the discretization.

Once two full bounces are completed ($t \approx 2\pi$), we consider not only the error mass at that moment but also the error of the U and V functions from the last spectral coefficient in the domain where the error is maximum. This is shown in Fig.4.9 for grid configurations of ten domains with different number of points and precisions. As expected, all three quantities decays exponentially until they have reached the round-off error. For double precision (red points) this happens at values of the $10^{-14} - 10^{-15}$ that is easily overcome using higher precision as in the turquoise points of this plot. With this we can easily evolve the configuration with an accuracy below 10^{-24} with a very low number of collocation points per domain as 28, for a total of 290 points.

4.5 Conclusions and Future Prospects

In this chapter we have presented the potential of the PSC methods in arbitrary precision computations using the **C++ ANETO** library that we have developed. The basic examples shown in Sec. 4.3 already give a glimpse of the potential that PSC methods with very few collocation points are capable to achieve increadible precisions when we allow the use of high precision arithmetic. In Sec. 4.4, this is proven with the use of complex problems in numerical relativity when again the use of high number of significant digits shows how far we can go.

In Sec. 4.3.2, we have seen that the main problem of arbitrary precision arithmetic is that usually is implemented via a software layer that slows tremendously our computation respect to the use of standard double precision. In this sense spectral methods can help because due to the exponential order of convergence, the discretization points required are smaller and therefore less computational demanding. Secondly, the multidomain scheme here presented is very suitable for parallelization as we have showed with the use of OpenMP. The scalability of the multidomain is very good for now but for making the library more powerful can be interesting to explore more low level approach that address the problem of the arbitrary precision arithmetic.

The current version of the library have been release with the basics to be useful for evolution problems but its functionalities are just few of the total possibilities that PSC methods offer and that **ANETO** it expected to incorporate in the future. Maybe one of the main ones is the possibility of solving linear and non-linear general Ordinary Differential Equations. Also some kind of Adapting Mesh Refinement method to allow the grid to be more flexible under problems different conditions or in a farther future the incorporation of more than one dimensions. Another aspect that we have not discuss in this paper is time integration. As the demand for

accuracy increase, this aspect become very important and a high-order integration can help a lot to reduce the number of steps in an evolution. For this reason, a spectral time integration like the ones used in Refs. [21, 22, 23] can be a very interesting to improve the accuracy of the evolutions with arbitrary prevision arithmetic.

Bibliography

[1] Philippe Grandclement and Jerome Novak. Spectral methods for numerical relativity. *Living Rev. Rel.*, 12:1, 2009.

[2] Claudio Canuto, M Yousuff Hussaini, Alfio Quarteroni, and Thomas A Zang. *Spectral methods: evolution to complex geometries and applications to fluid dynamics*. Springer Science & Business Media, 2007.

[3] William Bourke. *Spectral Methods in Global Climate and Weather Prediction Models*, pages 169–220. Springer Netherlands, Dordrecht, 1988.

[4] Martin Ehrendorfer. *Spectral Numerical Weather Prediction Models*. Other titles in applied mathematics. Society for Industrial and Applied Mathematics, 2012.

[5] David H. Bailey and Jonathan M. Borwein. High-Precision Arithmetic in Mathematical Physics. *Mathematics*, 3(2):337, 2015.

[6] Laurent Fousse, Guillaume Hanrot, Vincent Lefèvre, Patrick Pélissier, and Paul Zimmermann. MPFR: A Multiple-precision Binary Floating-point Library with Correct Rounding. *ACM Trans. Math. Softw.*, 33(2), June 2007.

[7] Pavel Holoborodko. MPFR C++. http://www.holoborodko.com/pavel/mpfr/, 2008-2012.

[8] ANETO library: Arbitrary precisioN solvEr with pseudo-specTral MethOds. `https://github.com/DSantosO/anetolib`, 2017.

[9] Eugene Loh and G. William Walster. Rump's example revisited. *Reliable Computing*, 8(3):245–248, 2002.

[10] Gaël Guennebaud, Benoît Jacob, et al. Eigen v3. http://eigen.tuxfamily.org, 2010.

[11] Leonardo Dagum and Ramesh Menon. OpenMP: an industry standard API for shared-memory programming. *Computational Science & Engineering, IEEE*, 5(1):46–55, 1998.

[12] Mioara Joldes, Jean-Michel Muller, Valentina Popescu, and Warwick Tucker. CAMPARY: Cuda Multiple Precision Arithmetic Library and Applications. In *5th International Congress on Mathematical Software (ICMS)*, Berlin, Germany, July 2016.

[13] Daniel Santos-Oliván and Carlos F. Sopuerta. New Features of Gravitational Collapse in Anti-de Sitter Spacetimes. *Phys. Rev. Lett.*, 116(4):041101, 2016.

[14] Daniel Santos-Oliván and Carlos F. Sopuerta. Moving closer to the collapse of a massless scalar field in spherically symmetric anti–de Sitter spacetimes. *Phys. Rev.*, D93(10):104002, 2016.

[15] Demetrios Christodoulou. The Problem of a Selfgravitating Scalar Field. *Commun. Math. Phys.*, 105:337–361, 1986.

[16] Dalia S. Goldwirth and Tsvi Piran. Gravitational Collapse of Massless Scalar Field and Cosmic Censorship. *Phys. Rev.*, D36:3575, 1987.

[17] David Garfinkle. Choptuik scaling in null coordinates. *Phys. Rev.*, D51:5558–5561, 1995.

[18] Rong-Gen Cai and Run-Qiu Yang. Multiple critical gravitational collapse of charged scalar with reflecting wall. 2016.

[19] James H. Verner. Explicit runge-kutta methods with estimates of the local truncation error. *SIAM Journal on Numerical Analysis*, 15(4):772–790, 1978.

[20] Peter J. Prince and John R. Dormand. High order embedded Runge-Kutta formulae. *Journal of Computational and Applied Mathematics*, 7(1):67–75, 1981.

[21] Jorg Hennig and Marcus Ansorg. A Fully Pseudospectral Scheme for Solving Singular Hyperbolic Equations on Conformally Compactified Space-Times. *J. Hyperbol. Diff. Equat.*, 6:161, 2009.

[22] Jorg Hennig. Fully pseudospectral time evolution and its application to 1+1 dimensional physical problems. *J. Comput. Phys.*, 235:322–333, 2013.

[23] Rodrigo Panosso and Marcus Ansorg. Axisymmetric fully spectral code for hyperbolic equations. *J. Comput. Phys.*, 276:357–379, 2014.

Overview and Conclusions

In this thesis we have studied several open problems using numerical methods as the main tool, showing the great potencial of Numerical Relativity to address problems in gravitation. This branch of General Relavity help us to solve problems that are very difficult or prohibitive by another means. Moreover, it opens the door to constructing new solutions of the Einstein Field Equations for spacetimes without symmetries or any special properties. Even in cases with some symmetry, as in the problems that we have discussed in this thesis, it is unreasonable to think that they could be treated without appropiate numerical tools. Anyway, it is also not very wise to think that we can work only with numerical methods and therefore the combination of numerical, analytic and perturbative tecniques is vital and very fruitful.

On the other hand, the study of the dynamics of AdS spacetimes is very important for several reasons The first one is theoretical. The discovery of the *turbulent instability* common to AdS and another confined geometries is useful to understand the structure of the equations of General Relativity and the features of relativistic gravitation. Another interesting aspect is the possible role of AdS in the Randall–Sundrum scenarios. And the last, but not least important, is its use in the holographic correspondence that we have used in parts of this thesis. For all these reasons, the interest and applications on AdS has increased in the last couple of decades and it seems that is going to rise even more in the next years.

Our research on the gravitational collapse of massless scalar fields in AAdS spacetimes, Chapter 2, has brought a very interesting outcome. First of all, we have developed a new method that combines two different formulations of the Einstein Field Equations to get closer to the collapse and with more accuracy. The first one is a Cauchy scheme similar to the ones used in the literature but with a multidomain grid and a pseudo-spectral collocation method that gives a very good precision to deal with the dynamics of this spacetime. This is important because the boundary of AdS confines the scalar field and then it is forced to bounce there. For this reason, it needs to be tracked with high accuracy, specially for configurations near to the critical points. The second scheme is based on characteristic coordinates and help us to track the formation of the apparent horizon. The transformation between the

two is performed during the simulation. The collapse of the scalar field happens after a number of bounces with the critical points being the separation between the different branches. We have numerical evidence that in the separation of the branches there is a power law for subcritical configurations in addition to the one for supercritical ones. This new power law have a universal exponent $\xi \approx 0.70$ to any initial conditions and to the different branches. It also confirms that there is a gap in the mass of the apparent horizon. This work has been published in two papers in the *Physical Review Letters* and *Physical Review D* journals. Despite of the numerical evidence, the exact interpretation of this new power law and its relation with the already known critical behaviour is still uncertain and remains as a question for future research. In addition, it would be interesting to study the influence of more complex matter content, like massive scalar fields, in the new power law that we have found. Also in other confined geometries. In this sense, there have been works that report the same phenomena in flat spacetime with an artificial boundary but a different value of the exponent was found. This could be an stimulating difference that needs to be analysed in more detail.

We have also described the shock waves model in AdS to study the far-from-equilibrium studies in the heavy ion collisions and the formation of the QGP through the holographic correspondence. This has attracted a lot of attention in the last few years because of the possibility of simulating strongly coupled systems but, as a drawback, we do not know yet the exact dual of the QCD that should explain the phenomena. In the models used until now, the shock waves corresponds to conformal gauge theories while QCD is not conformal. And this an important limitation. For this reason, in order to get closer to a description of the actual physical collisions, we need to study non-conformal theories. In Chapter 3, we have presented the first shock wave collisions in a non-conformal theory. The results obtained on this have been presented in two papers in *Journal of High Energy Physics* and another one with more details is about to be released. We show how the non-conformality increases the hydrodynamisation time and also that this can happen before the equation of state is fulfilled. The continuation of the study of non-conformal theories is going to be important to approach to this system meanwhile a better dual for QCD is discovered. The reduction of some symmetries and the simulation in higher dimensional AAdS scenarios is also essential.

The last chapter has been dedicated to the proposal of the pseudo-spectral collocation method as a very strong candidate for high precision computations. The use of an arbitrary large number of digits has two main problems. The first is the necessity of increasing a lot the discretisation points to reach the precision we want. The other one is the slowing down in the computational performance due to the fact that we need to emulate the fundamental operations with software because the processors are not adapted to carry out computations with precision different from the standard one, double or float. The exponential convergence of spectral methods can approximate functions to a very high accuracy with a few hundred

terms in our spectral expansion while in other numerical methods it would be a few orders of magnitude larger. This makes these methods very atractive because they facilitate the accessibility to very small error simulations, removes the bottleneck of the memory demand and also help in the computational speed because fewer points are needed for the computation. We have tested this idea with the **ANETO** library for simulations in AdS spacetimes and the gravitational collapse in an asymptotically flat spacetime with very promising results. This library has been developed as a direct result of this thesis and that can be downloaded as Free Software. The results are very promising and it should be applicable also for long-term simulations. For these long-term simulations the usual algorithms to perform the time integratation maybe are not enough and it can be a good idea to improve them with spectral methods. Other prospect for the future is to use pseudo-spectral methods with arbitrary precision for problems in other fields of science where high accuracy is currently being used.